Z-Pinch Pulsed Plasma Propulsion Technology Development

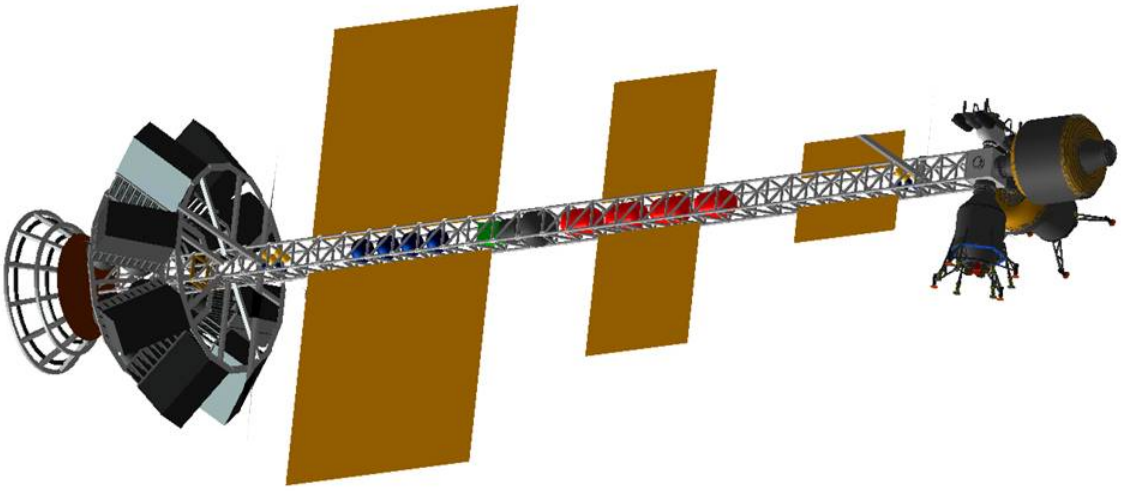

Final Report

Advanced Concepts Office (ED04)

Marshall Space Flight Center

October 8, 2010

TABLE OF CONTENTS

LIST OF ACRONYMS

AU	Astronomical Unit
C&DH	Command and Data Handling
CCD	Charge-Coupled Device
COPV	Composite Overwrapped Pressure Vessel
D-T	deuterium-tritium
DTRA	Defense Threat Reduction Agency
ECLSS	Environmental Control and Life Support System
ERC	Engineering Research and Consulting
FEMAP	Finite Element Modeling and Post-processing
G&N	Guidance and Navigation
GNC	Guidance, Navigation and Communications
HOPE	Human Outer Planet Exploration
ICF	Inertial Confinement Fusion
ISP	Initial Specific Impulse
LSI	Laser Shearing Interferometer
MAGPIE	Mega-ampere generator for plasma implosion experiments
MHD	Magneto-Hydrodynamic
MIF	Magneto-Inertial Fusion
MSFC	Marshall Space Flight Center
MTF	Magnetized Target Fusion
NWE	Nuclear Weapons Effects
PFC	Plasma Facing Component
PLIF	Planar Laser Induced Fluorescence
PRS	Plasma Radiation Sources
RASC	Revolutionary Aerospace Systems Concepts
RCS	Reaction Control System
SAIC	Science Applications International Corporation
SMES	Superconducting Magnetic Energy Storage
SNL	Sandia National Laboratory
XRD	X-Ray Diode

LIST OF TABLES

LIST OF FIGURES

TEAM MEMBERS

Tara Polsgrove, MSFC
Robert B. Adams, MSFC
Leo Fabisinski, ISSI - MSFC
Sharon Fincher, MSFC
C. Dauphne Maples, Qualis - MSFC
Janie Miernik, ERC - MSFC
Tom Percy, SAIC - MSFC
Geoff Statham, ERC - MSFC
Matt Turner, UAH - MSFC

Jason Cassibry, UAH
Ross Cortez, UAH - MSFC

John Santarius, U of W

1 INTRODUCTION

Fusion-based propulsion can enable fast interplanetary transportation. Magneto-inertial fusion (MIF) is an approach which has been shown to potentially lead to a low cost, small reactor for fusion break even (Lindemuth and Siemon 2009). The Z-Pinch/dense plasma focus method is an MIF concept in which a column of gas is compressed to thermonuclear conditions by an axial current (I~100 MA). Recent advancements in experiments and the theoretical understanding of this concept suggest favorable scaling of fusion power output yield as I^4 (Velikovich et al. 2007). This document presents a conceptual design of a Z-Pinch fusion propulsion system and a vehicle for human exploration.

The purpose of this study is to apply Z-Pinch fusion principals to the design of a propulsion system for an interplanetary spacecraft. This study took four steps in service of that objective; these steps are identified below.

1. ***Z-Pinch Modeling and Analysis***: There is a wealth of literature characterizing Z-Pinch physics and existing Z-Pinch physics models, e.g. (Olson et al. 2005; Shumlak 2006; Velikovich et al. 2007). In order to be useful in engineering analysis, simplified Z-Pinch fusion thermodynamic models are required to give propulsion engineers the quantity of plasma, plasma temperature, rate of expansion, etc. The study team developed these models in this study.
2. ***Propulsion Modeling and Analysis***: While the Z-Pinch models characterize the fusion process itself, propulsion models calculate the parameters that characterize the propulsion system (thrust, specific impulse, etc.) The study team developed a Z-Pinch propulsion model and used it to determine the best values for pulse rate, amount of propellant per pulse, and mixture ratio of the D-T and liner materials as well as the resulting thrust and specific impulse of the system.
3. ***Mission Analysis***: Several potential missions were studied. Trajectory analysis using data from the propulsion model was used to determine the duration of the propulsion burns, the amount of propellant expended to complete each mission considered.
4. ***Vehicle Design***: To understand the applicability of Z-Pinch propulsion to interplanetary travel, it is necessary to design a concept vehicle that uses it – the propulsion system significantly impacts the design of the electrical, thermal control, avionics and structural subsystems of a vehicle. The study team developed a conceptual design of an interplanetary vehicle that transports crew and cargo to Mars and back and can be reused for other missions. Several aspects of this vehicle are based on a previous crewed fusion vehicle study – the Human Outer Planet Exploration (HOPE) Magnetized Target Fusion (MTF) vehicle. Portions of the vehicle design were used outright and others were modified from the MTF design in order to maintain comparability.

2 Z-PINCH FUSION MODELING AND ANALYSIS

2.1 Z-Pinch Fusion

The approach investigated in this study involves the use of a confinement scheme known as a Z-Pinch, which falls under the MIF regime. The premise of a Z-Pinch is to run very large currents (Megampere scale) through a plasma over short timescales (10^{-6} sec). The magnetic field resulting from the large current then compresses the plasma to fusion conditions. This plasma formation is widely used in the field of Nuclear Weapons Effects (NWE) testing in the defense industry, as well as fusion energy research. Facilities of note include the Z Machine at Sandia National Laboratories (SNL) and MAGPIE at Imperial College, London. For a fusion propulsion system, the Z-Pinch is formed using annular nozzles with Deuterium-Tritium (D-T) fuel in the innermost nozzle and a lithium mixture containing lithium-6/7 in the outermost nozzle. The configuration would be focused in a conical manner so the D-T fuel and lithium-6/7 mixture meet at a specific point that acts as a cathode so that the lithium mixture can serve as a current return path to complete the circuit, as shown in Figures 2.1 and 2.2.

In addition to serving as a current return path, the lithium liner also serves as a radiation shield. The advantage to this configuration is the reaction between neutrons and lithium-6 resulting in the production of Tritium, thus adding further fuel to the fusion reaction, and boosting the energy output. In utilizing this method of fusion for propulsion, high thrusts and/or specific impulse can be produced.

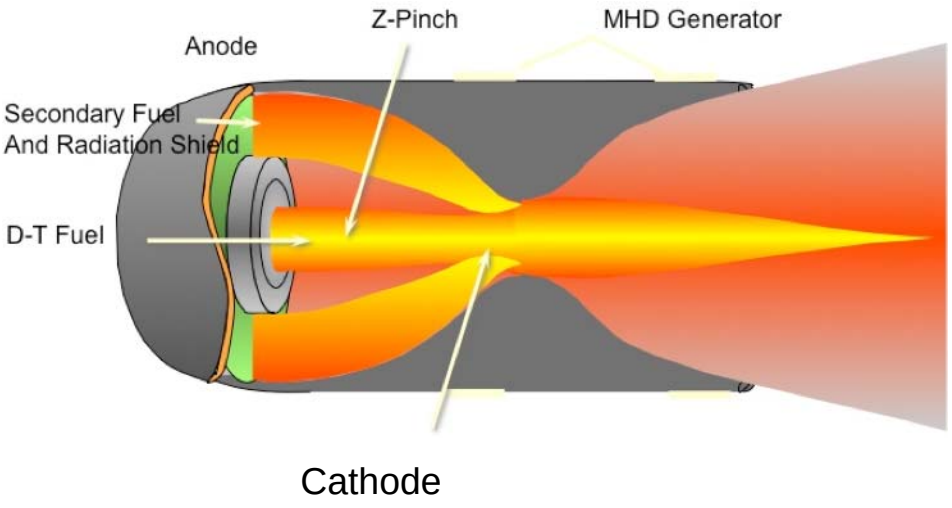

Figure 2.1 Concept Drawing 1

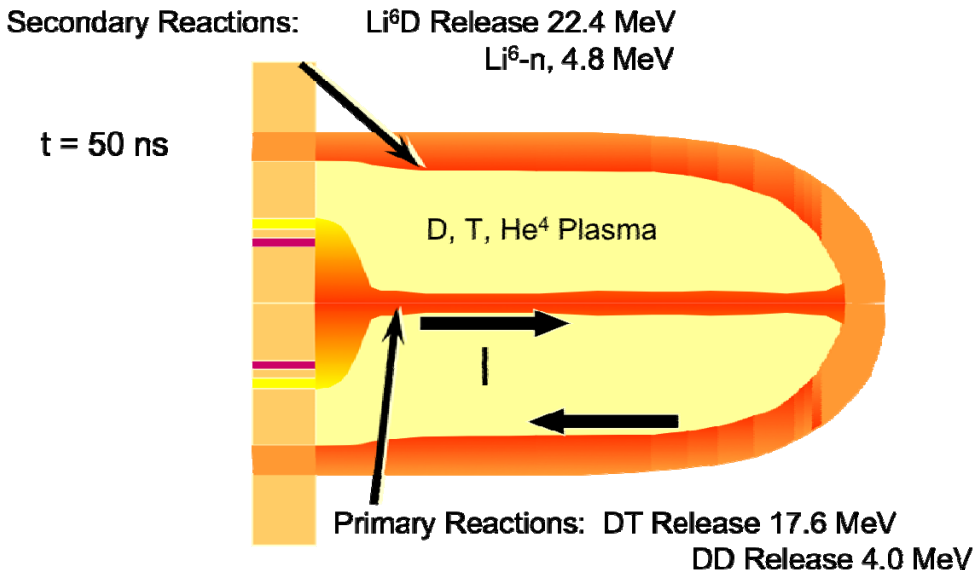

Figure 2.2 Concept Drawing 2

2.2 Fusion Reaction Engine Cycle Analysis

Modeling and analysis of fusion plasmas and their dynamics is a large field in which multiple approaches have been taken to gain insight into how the fusion process proceeds according to the dynamics of an implosion, laser/plasma interaction, etc. (Schulze 1991). The difficulties and complications involved in modeling magnetohydrodynamic (MHD) flows, as well as the fusion reactions themselves, are legion, necessitating the formulation of simple models and approximations to facilitate understanding. Computational studies, performed with complex programs and large amounts of computing power, have tremendous value in the fusion community due to the wealth of quantitative data they provide. Although this may be true, the intrinsic value of simple, analytical models must not be overlooked due to their ability to quickly impart qualitative understanding of a concept. It is therefore advantageous to have these models to describe fusion processes to guide subsequent use of higher fidelity codes and experiments.

An example of the wealth of qualitative information such simple models may provide is given by the cold air-standard analysis of an internal-combustion engine, also known as an Otto cycle. The combustion of fuel within the engine makes the analysis of such a process exceedingly complicated. In addition to this, fuel and air flow steadily into the engine while combustion products flow steadily out of it such that no working medium undergoes a cyclic process. However, a simple analysis can be made by imagining a cyclic engine with air as the working fluid that is equivalent in performance to actual internal-combustion engines. Furthermore, the step involving combustion is replaced by the addition of an equivalent amount of heat to the air at a constant volume.

Likewise, a similar approximation may be made to develop a qualitative understanding of multiple fusion ignition processes. Thus, within the framework of thermodynamics, it is

possible to develop a straightforward engineering cycle analysis in similar fashion to those developed for the internal-combustion engine. In what follows, the ideal thermodynamic model that describes the Otto cycle is presented. This model is then used to explain the performance of a fusion reaction engine. The theoretical development of the cycle and its implications and inputs is described next, followed by the results used for this study and the design points chosen based on those results.

The Otto cycle takes place in a four step, or four-stroke process, for which the working fluid is air, considered an ideal gas with constant heat capacities. The process is illustrated in Figure 2.3 and proceeds in four steps as follows:

- *Process 1-2: Isentropic compression*
- *Process 2-3: Constant volume heat addition*
- *Process 3-4: Isentropic expansion*
- *Process 4-1: Constant volume heat rejection*

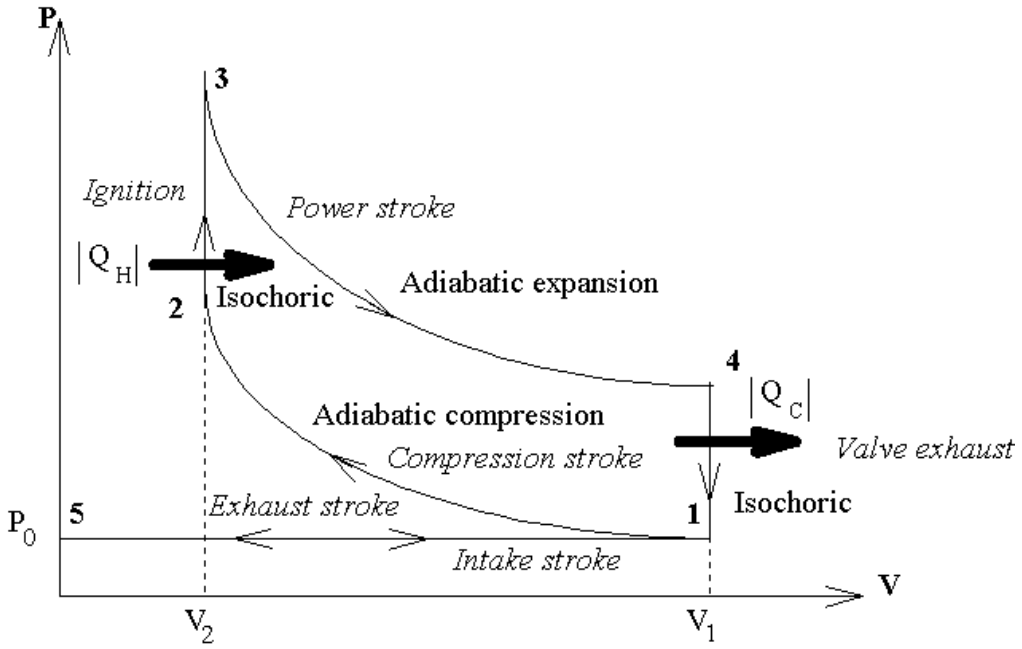

Figure 2.3 Pressure-Volume Diagram for Otto cycle

The energy balance $(q_{in} - q_{out}) + (w_{in} - w_{out}) = \Delta u$ gives:

$$[1-2]: \quad w_{in} = u_2 - u_1$$
$$[2-3]: \quad q_{in} = u_3 - u_2$$
$$[3-4]: \quad w_{out} = u_3 - u_4$$
$$[4-1]: \quad q_{out} = u_4 - u_1$$

For processes [2-3] and [4-1], the heat transfer occurs at constant volume, thus giving

$$[2-3]:\ \ q_{in} = q_{23} = u_3 - u_2 = c_v\left(T_3 - T_2\right)$$
$$[4-1]:\ \ q_{out} = q_{41} = u_4 - u_1 = c_v\left(T_4 - T_1\right)$$

Processes [1-2] and [3-4] are isentropic, so the following relations may be used:

$$\left(\frac{T_2}{T_1}\right) = \left(\frac{V_1}{V_2}\right)^{\gamma-1} = \left(\frac{p_2}{p_1}\right)^{\frac{\gamma-1}{\gamma}}$$

since $pV^{\gamma} = const.$
Assuming cylindrical geometry of the system, the volume as $V = \pi R^2 l$ may be written so that

$$\frac{T_2}{T_1} = \left(\frac{V_1}{V_2}\right)^{\gamma-1} = \left(\frac{\pi l R_1^{\,2}}{\pi l R_2^{\,2}}\right)^{\gamma-1} = \left(\frac{R_1}{R_2}\right)^{2(\gamma-1)} = r^{2(\gamma-1)}$$
$$\frac{T_4}{T_3} = \left(\frac{V_3}{V_4}\right)^{\gamma-1} = \left(\frac{V_2}{V_1}\right)^{\gamma-1} = \left(\frac{R_2}{R_1}\right)^{2(\gamma-1)} = \left(\frac{1}{r}\right)^{2(\gamma-1)}$$

where $r = R_1/R_2$ is the compression ratio, $V_2 = V_3$ and $V_4 = V_1$. Then the isentropic processes may be written as

$$[1-2]:\ \ w_{in} = w_{12} = u_2 - u_1 = c_v\left(T_2 - T_1\right) = c_v T_2\left(1 - r^{2(1-\gamma)}\right)$$
$$[3-4]:\ \ w_{out} = w_{34} = u_3 - u_4 = c_v\left(T_3 - T_4\right) = c_v T_3\left[1 - \left(\frac{1}{r}\right)^{2(\gamma-1)}\right]$$

The efficiency η of the cycle will be

$$\eta = \frac{|w_{net}|}{q_{23}} = \frac{q_{23} + q_{41}}{q_{23}} = \frac{c_v\left(T_3 - T_2\right) + c_v\left(T_4 - T_1\right)}{c_v\left(T_3 - T_2\right)} = 1 - \frac{T_4 - T_1}{T_3 - T_2}$$

or

$$\eta = 1 - \left(\frac{1}{r}\right)^{\gamma-1}.$$

As stated above, similar approximations may be made that will illuminate a qualitative understanding of multiple fusion ignition processes. This study examines the formation, implosion, and explosion of a Z-Pinch plasma. As a starting point, illustrating how this particular confinement scheme is achieved is useful. Next, the similarities between this process and a typical internal-combustion engine are presented. The analytical model

used to extract performance parameters for a propulsion system utilizing this method of confinement is also explained.

Basic Z-Pinch Operation

A Z-Pinch is a radial implosion of a cylindrical or annular plasma under the influence of a strong magnetic field produced by current flowing down the length of the plasma; it usually involves the ionization and subsequent implosion of a gas for time-scales on the order of microseconds. The process can be broken down into a number of steps that occur in the following order (see figure below):

1. Gas injection/pre-ionization
2. Compression/implosion
3. Stagnation/burn
4. Expansion/explosion

Upon close examination, this process can be observed as strikingly similar to the operation of an Otto cycle. Therefore the following correlations can be made:

1) The gas injection/pre-ionization phase can be considered in a similar fashion to the valve intake process of an internal-combustion engine
2) Compression/implosion can be correlated to Process 1-2 of the Otto cycle, making similar assumptions: approximate the plasma as an ideal gas, with constant specific heats and composition.
3) Stagnation/burn is the stage in which the plasma reaches fusion conditions, thus causing fusion reactions to occur. In this case, like the normal combustion process, the fusion reactions can be considered to occur rapidly enough such that the process takes place at constant volume. This stage can therefore be approximated as a constant volume heat addition like Process 2-3 of the Otto cycle.
4) Expansion/explosion, like Process 3-4 of the Otto cycle, can also take place isentropically under the same assumptions. For this particular propulsion application, the process takes place by expanding the plasma out of a magnetic nozzle into a vacuum.
5) Process 4-1 of the Otto cycle can be incorporated into the fusion reaction engine model by assuming constant volume heat rejection from the plasma, thus returning to state 1. Like the Otto cycle, this does not necessarily reflect reality, but is nonetheless useful when considering the general performance of an engine.

Using the correlations stated above, a useful thermodynamic model incorporating simple plasma physics arguments to describe the performance of a Z-Pinch fusion reaction cycle can be constructed.

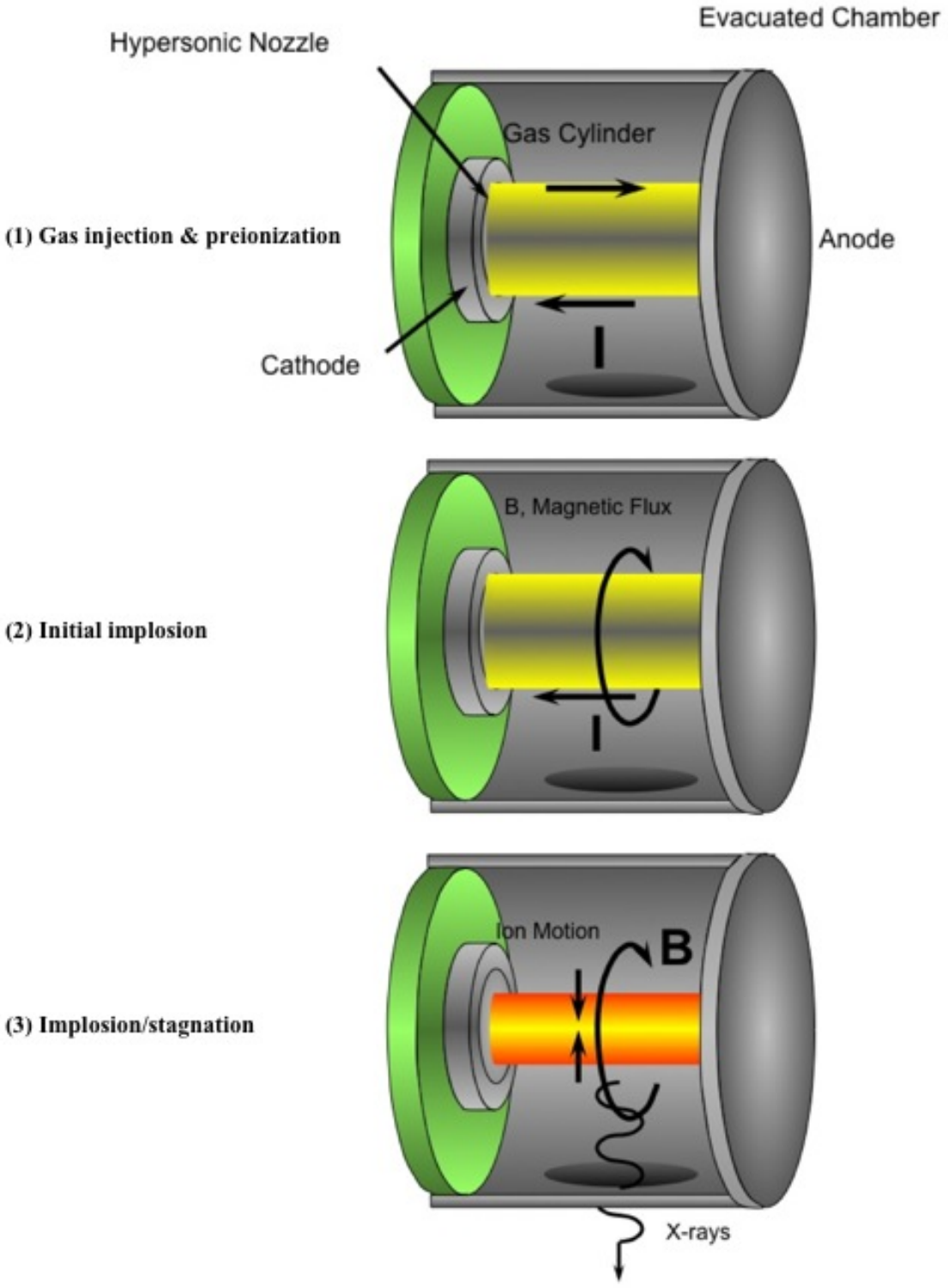

Figure 2.4 Stages of Z-Pinch Formation

Before further developing the thermodynamic analysis of the Z-Pinch system, there are a few important notes to consider involving the formation process. First, the Z-Pinch process proceeds by pulsing large currents through the gas being used. Therefore, electrodynamics plays a significant role in the performance of the system. Due to this, the effects of electric and magnetic field dynamics must be incorporated into the model. Second, the representation of this cycle analysis can only be made by considering the state of the system at each individual step of the process. The complicating effects of the electric and magnetic fields must therefore be somehow discretized to consider each state individually, disregarding the dynamics in between. A simple pressure balance model used to describe Z-Pinch stability facilitates this by assuming the pinch to be a cylindrical column of fully ionized gas with an axial electric field, producing an axial current density, $\mathbf{j}$, and an associated azimuthal magnetic field, $\mathbf{B}$. As this current flows through its own magnetic field, it produces an inward radial force density of $\mathbf{j} \times \mathbf{B}$. The pressure balance is achieved by matching the internal gas pressure with the pressure of the magnetic field compressing the column, which can be shown to be

$$p = \frac{B^2}{2\mu_0}.$$

Finally, by focusing on the energy states of each process and knowing certain criteria, such as temperature, composition, and geometry of the system, the input requirements of the system to achieve ignition can be determined. For example, to ignite a 50/50 Deuterium-Tritium gas mixture, the minimum temperature required at state 2 (compressed state) is at least 10 keV. Knowing this temperature, and the mixture composition, the magnetic field strength (and therefore current) required for ignition via simple thermodynamic arguments can be backed out. Thus the input parameters used to design the system can be simplified to simple functions of the ignition temperature, compression ratio, and mass of the fuel being used.

As noted above in the introductory sections of this report, the Z-Pinch propulsion concept studied here is modified from a typical Z-Pinch confinement scheme by using a liquid lithium mixture to serve as the current return path for the circuit. This serves two purposes: (1) the lithium acts as a partial shield to capture neutrons from the D-T reaction, releasing further energy in the reaction as well as helping to reduce the burden of the neutron load on the surrounding nozzle structure, and (2) it will add mass to the exhaust of the rocket causing increased mass flow and therefore increased thrust. In the model depicted here, the lithium liner mass is defined to be a function of the fuel mass in order to determine its effect on the overall performance of the system. By plotting parameters such as specific impulse, thrust and acceleration as functions of the fractional liner mass the results show a significant dependence upon the liner mass and therefore the fuel mass and composition.

To model the fusion reaction engine, the first step is to re-state the steps of the Otto cycle and writing the energy balance for each:

- *Process 1-2: Isentropic compression* $[1-2]: \quad w_{in} = u_2 - u_1$
- *Process 2-3: Constant volume heat addition* $[2-3]: \quad q_{in} = u_3 - u_2$
- *Process 3-4: Isentropic expansion* $[3-4]: \; w_{out} = u_3 - u_4$
- *Process 4-1: Constant volume heat rejection* $[4-1]: \quad q_{out} = u_4 - u_1$

For process [1-2], knowing the ignition temperature required, a value for the initial temperature of the plasma can be backed out since

$$T_1 = T_2 r^{-2(\gamma-1)}.$$

Treating the plasma at state 1 as an ideal gas, so that $p_1 = \rho_1 R T_1$, and using the pressure balance stated above, values of magnetic field estimated at state 1, current required to generate the field, and the magnetic field energy:

$$B_1 = \sqrt{2\mu_0 p_1}$$

$$I_1 = \frac{B_1}{\mu_0}(2\pi R_1)$$

$$E_{mag,1} = \frac{B_1^{\,2}}{2\mu_0}\left(\pi R_1^{\,2} l\right)$$

Following the same procedure also enables estimating these values at state 2.
Process [2-3], constant volume heat addition, is evaluated by the relation

$$q_{23} = c_v(T_3 - T_2)$$

only by fixing states 2 and 3 by a given temperature. Although this value is known at state 2, fixing a temperature at state 3 (after expansion of the reacting plasma) would be superfluous due to the ambiguity of the properties of the plasma after the explosion. This is also an obvious problem since a real fusion reaction engine would not be a closed system. However, rather than choosing an arbitrary temperature to fix the end state of the process, that temperature can be calculated by knowing the nature of how the fusion reactions in the plasma proceed. It is assumed that the following reactions take place:

$$D + T \rightarrow He^4\ (3.5\ MeV) + n\ (14.1\ MeV)$$

$$D + D \underset{50\%}{\rightarrow} T\ (1.01\ MeV) + p\ (3.02\ MeV)$$

$$D + D \underset{50\%}{\rightarrow} He^3\ (0.82\ MeV) + n\ (2.45\ MeV)$$

$$D + He^3 \rightarrow He^4\ (3.6\ MeV) + p\ (14.7\ MeV)$$

$$T + T \rightarrow He^4 + 2n + 11.3\ MeV$$

It is also assumed that the lithium liner material acts as an inert observer in the process, not reacting with the D-T fuel. In this way the lithium only adds mass to the exhaust without adding further energy; this will also make the calculation a more conservative estimate. Calculating the reaction rates for each reaction followed by the energy of the products based on those reaction rates, the energies can be summed

$$E_{fus} = E_{He^3} + E_{He^4} + E_T + E_p$$

and the engineering gain calculated by

$$G = \eta \frac{E_{fus}}{E_{in}}$$

where η is an assumed efficiency of the transfer of energy from the driver to the load, taken to be 0.5, and the input energy is calculated as the sum of the magnetic and heating energy added to the plasma to achieve ignition at state 2:

$$\frac{E_{in}}{\eta} = E_{mag,2} + U_2 = \frac{B_2^{\,2}}{2\mu_0} V_2 + mc_v T_2 .$$

Now the temperature after the plasma expands is determined in process [2-3] by setting the energy at state 3 equal to the energy of the fusion products plus the energy added to the plasma by heating it to ignition:

$$U_3 = (m_l c_{vl} + mc_v) T_3 = E_{fus} + mc_v T_2$$

so that

$$T_3 = \frac{E_{fus} + mc_v T_2}{m_l c_{vl} + mc_v} .$$

Thrust and Isp results as a function of fractional liner mass $\left(\frac{\text{mass of lithium}}{\text{mass of DT fuel}}\right)$ are given below (see Figures 2.5 and 2.6), assuming the values in Table 2.1.

Table 2.1 Propulsion Assumptions

Pulse Frequency	10 Hz
Driver Energy Density	10 kJ/kg
Compression Ratio	10
Initial DT Fuel Mass	100 mg
Ignition Temperature	20 keV

The design point chosen for this vehicle concept study is designated in Figures 2.5 and 2.6. The fractional liner mass was chosen to be 200x the initial mass of the DT fuel injected into the thruster. This design point was chosen for three reasons:

1. By increasing the fractional liner mass beyond this ratio, the total vehicle mass was found to increase to extraneously large values due to the exponentially increasing amount of neutron shielding required in conjunction with the propellant needed for a given mission;
2. At this point, the values of thrust and specific impulse were found to have a striking balance while still imposing a reasonable limit on the size of the vehicle;
3. In choosing these values the advanced performance abilities of the vehicle could be displayed while still remaining conservative.

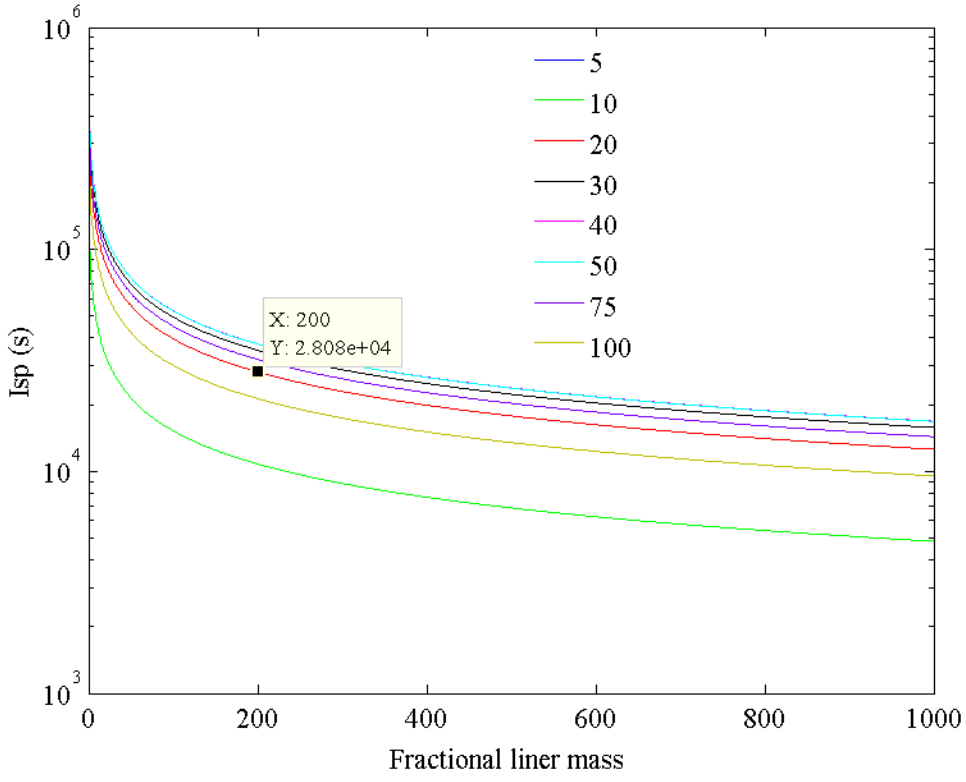

Figure 2.5 ISP as a Function of Liner Mass Ratio

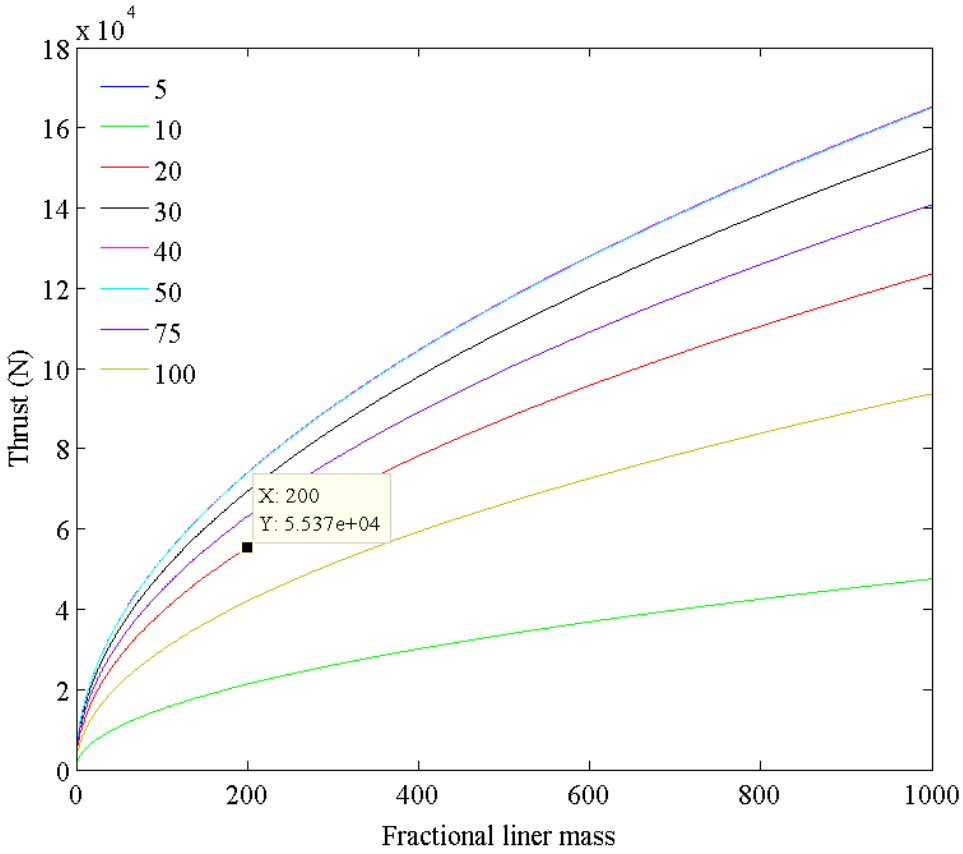

Figure 2.6 Thrust as a Function of Liner Mass Ratio

3 PROPULSION MODELING AND ANALYSIS

3.1 Propulsion Concept

After each fusion pulse, a magnetic nozzle converts the momentum of the radially expanding plasma shell into useful propulsive impulse for the vehicle. Its physical components are a number of current-carrying rings positioned so that they fall on a parabola (or more properly a paraboloid of revolution), which has its focus at the point of fusion – the point from which the plasma shell expands outwards. When an electrical current passes around each ring, the resulting magnetic field is illustrated in Figure 3.1.

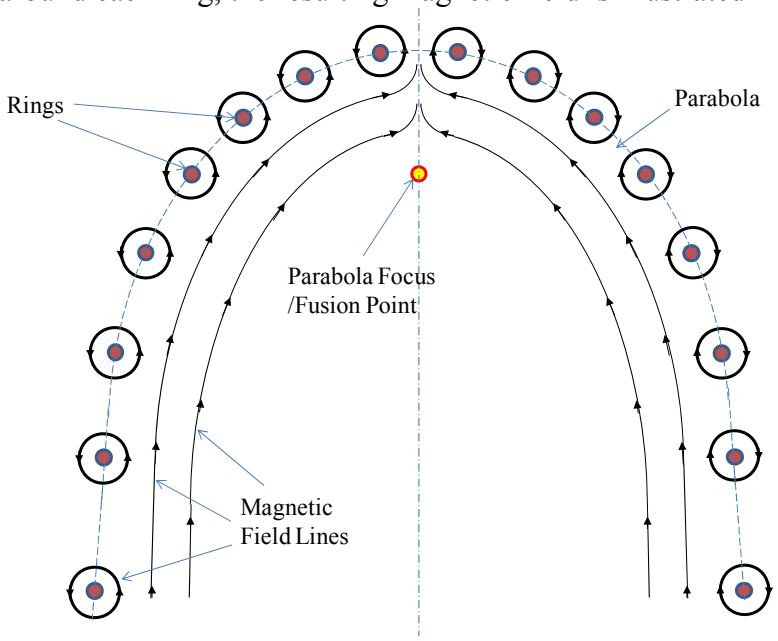

Figure 3.1 Magnetic Field

The expanding plasma is highly conductive, which means that as it impinges on the magnetic field lines, it effectively sweeps the magnetic field lines in front of it. A full description is given in Appendix A, but the net effect is that the magnetic flux is compressed into a progressively smaller annular region between the plasma and the rings. This process is illustrated in figures 3.2 and 3.3. Figure 3.2 shows a relatively early stage of plasma expansion, and figure 3.3 shows a somewhat later stage.

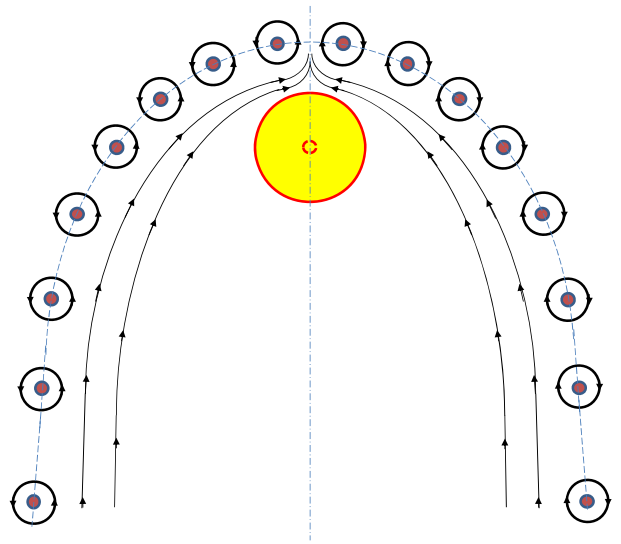

Figure 3.2 Early Stage of Plasma Expansion

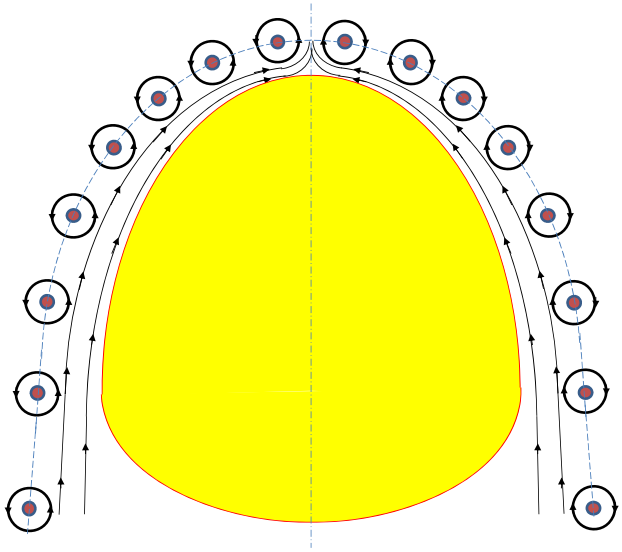

Figure 3.3 Later Stage of Plasma Expansion

As the magnetic flux is compressed, the field strength $(\underline{B})$ increases, as does the magnetic pressure (B^2/μ_0) – where μ_0 is the permeability of free-space. This increasing magnetic pressure acts on the expanding plasma shell, gradually slowing down its expansion until it comes to rest relative to the rings. The magnetic pressure also acts on the current-carrying rings, exerting both a radial force and an axial thrust force, which acts upwards along the main axis of the nozzle (and the vehicle).

At this point, the kinetic energy of the expanding plasma shell has been transferred into potential energy of magnetic flux compression. Once the expansion of the plasma shell has ceased, the magnetic pressure will begin to push the plasma back down the main axis of the nozzle. Because of its parabolic shape, the nozzle has the useful property that

plasma radiating outwards from the focus will be directed out of the nozzle, parallel to the axis – no matter where it strikes. As a result of this, the plasma is eventually expelled from the nozzle and the magnetic field is restored to its original configuration, as illustrated in figure 3.4.

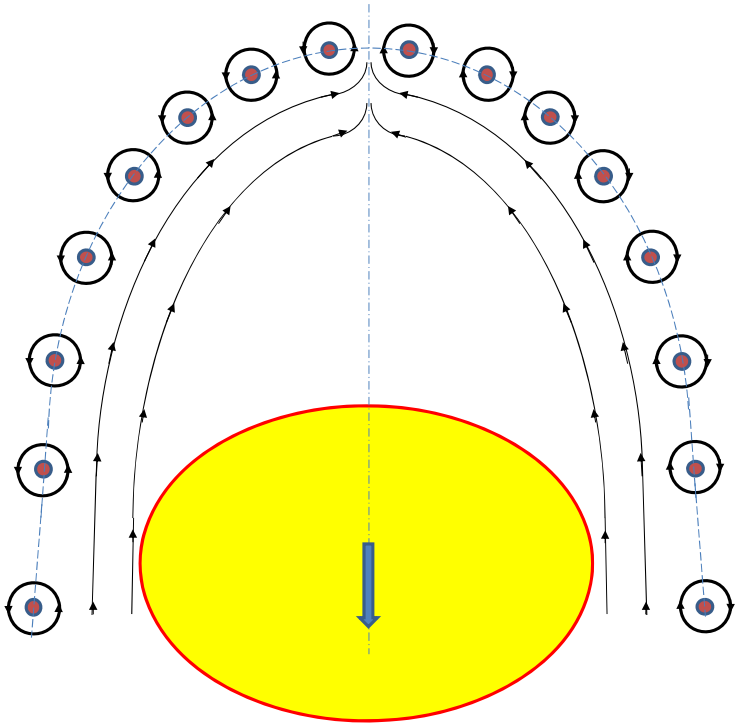

Figure 3.4 Magnetic Field Restored

During the entire process of plasma expansion and expulsion, the magnetic field has acted in the manner of a spring, being first compressed and then expanding back to its original configuration. Useful thrust is being applied to the vehicle throughout the process.

3.2 Magnetic Nozzle Model

The magnetic nozzle performance model addresses the situation that arises relatively late during expansion of the plasma shell, when it has assumed the form of a paraboloid annulus. Although this means neglecting the initial portion of the expansion - when it transforms from spherical form to paraboloid form - this is acceptable because most of the useful impulse is only obtained late during the expansion, when flux compression, and hence magnetic pressure, are at a maximum. The model begins with the situation as shown below in Figure 3.5.

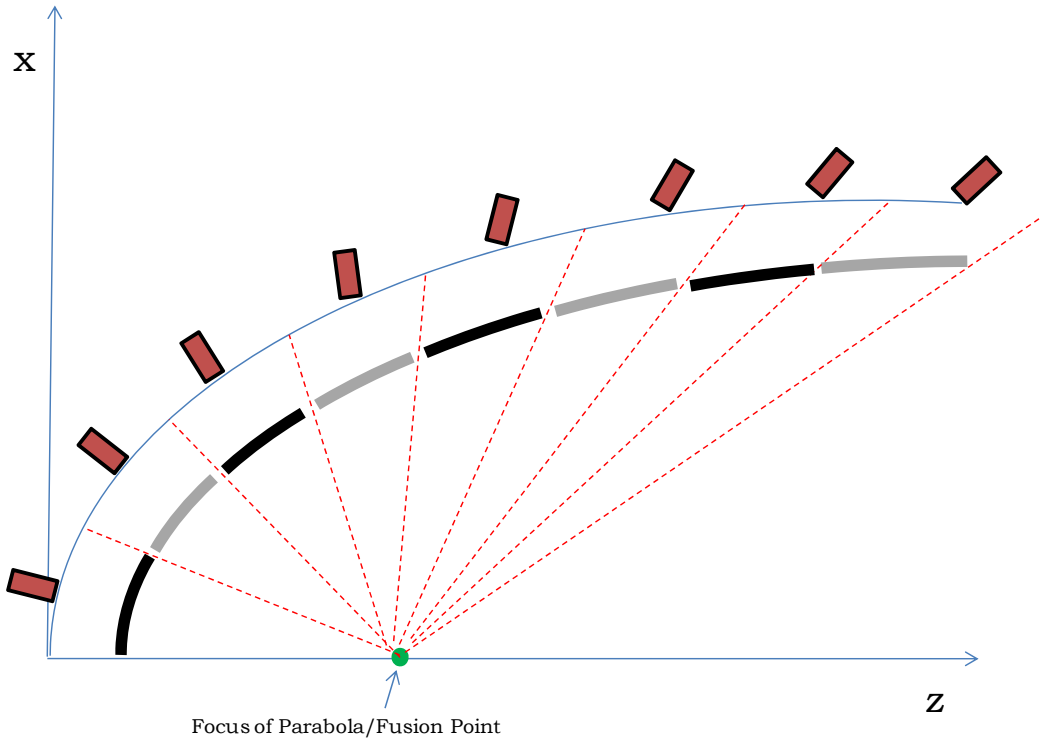

Figure 3.5 Paraboloid Form

For modeling purposes the plasma shell has been divided into a number of discrete segments, each of which is in the shape of a section of paraboloid annulus (shown in cross-section in Figure 3.5 – adjacent segments are shown in a pattern of alternate shading simply to distinguish them from each other). Each segment is moving radially away from the fusion point. The fusion point coincides with the focus of the nozzle paraboloid; it also coincides with the foci of the plasma paraboloid.

Starting from this configuration, the model follows the evolution of each segment in a series of time-steps as it moves outwards, compressing the magnetic flux and increasing magnetic pressure as it does so. A subsequent exaggerated time-step (with the segments still in motion) is shown in Figure 3.6.

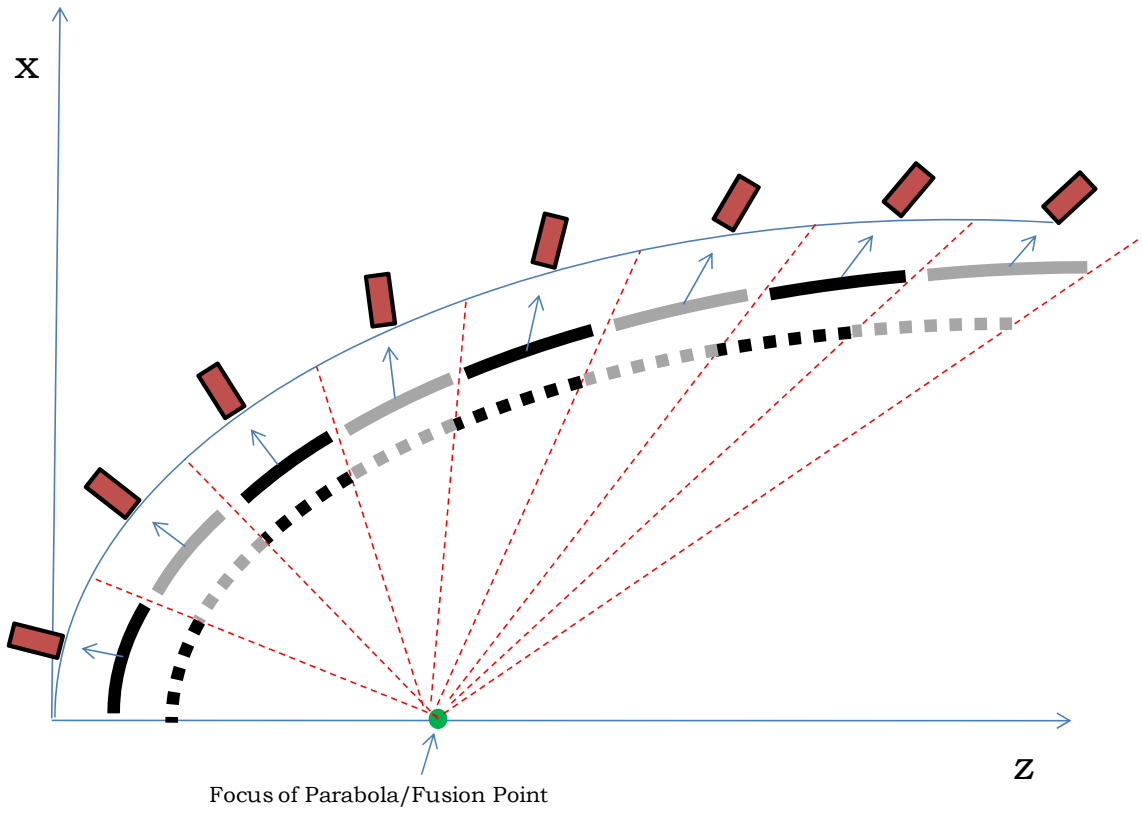

Figure 3.6 Subsequent Time-step

At each time step each segment is still treated as forming part of a paraboloid, but after the initial time-step each has a different paraboloid (although they still all have the same focus position). Details of the plasma shell expansion model are given in Appendix B.

As shown above, the number of plasma segments has been taken as equal to the number of nozzle rings (eight).

For illustration, Figure 3.7 shows the actual plasma segment trajectories that were modeled. The graph shows the parabola on which the segments were initially positioned (inner parabola) and the parabola on which the rings are located (outer parabola). The lines in between represent the trajectories followed by each of the (eight) plasma segments ('Series1' applies to the first segment – closest to the nozzle apex – and the numbering increases moving to the right). Each begins on the inner parabola, moves out towards the outer parabola and then 'reflects'. The total time taken to follow the trajectories shown is 15 microseconds (15×10^{-6} seconds).

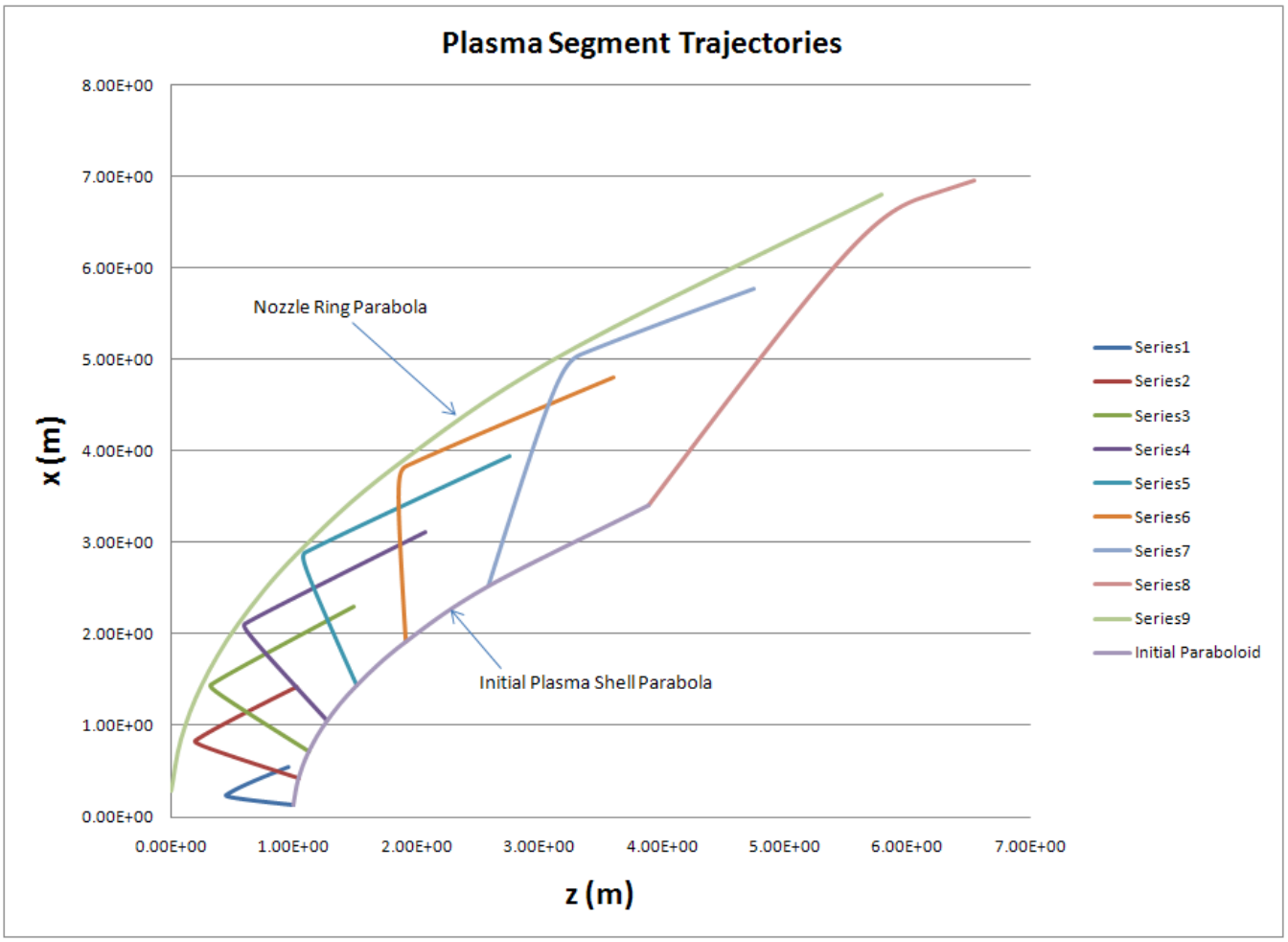

Figure 3.7 Plasma Segment Trajectories

After 'reflection' the trajectories do not follow paths parallel to the nozzle axis. As the nozzle is parabolic, this may seem unexpected. The reason for this apparent anomaly is that just after the point of maximum flux compression (i.e. when the plasma segments are very close to the rings, but have just begun to move away) a large amount of the magnetic field strength is lost when the energy needed to initiate the next fusion pulse is withdrawn inductively from each of the rings. Note that, as the different segments take differing amounts of time to reach their 'rebound' positions, this means that the inductive withdrawal takes place at slightly different times for each individual ring.

The design parameters for the nozzle are as follows:

3.3 Nozzle Details

The nozzle parabola focus is 2 meters from the apex (which is also the origin of the z-x coordinate system). This length has been selected as it is currently considered to be the greatest distance that can be maintained between the Z-Pinch event and the physical nozzle from which the fusion materials (deuterium and tritium) are expelled. In order to keep the physical nozzle outside the parabola, the fusion event (and hence the focus) must be no more than two meters from the apex. Distances less than 2 meters are

possible, but would result in a *smaller* parabola, which – investigation with the model shows – is not capable of successfully redirecting the expanding plasma before it impinges on the nozzle rings.

Note that this arrangement of rings, with a 2 meter focus, means that the nozzle angle is 60.9 °. This is the approximate angle subtended at the focus by the final and largest ring. This nozzle angle was selected because it provides 75% solid angle coverage from the focus (i.e. the nozzle covers ¾ of the total 4π solid angle as seen from the focus). This value was selected as a design starting point and can be varied in more detailed future studies (where the increased performance from a larger nozzle [smaller nozzle angle] can be traded against greater nozzle mass).

Plasma Details

The expanding plasma has a total mass of 0.02 kg and its initial kinetic energy is assumed to be 1 GJ (1×10^9 Joules).

Performance Details

The useful impulse (imparted to the vehicle) per pulse is 3812 N-seconds. Using a total reaction mass of 0.02 kg/pulse, this gives a specific impulse of 19436 seconds. Note that the actual thrust time-averaged over one second will depend upon the engine pulse repetition rate. With a pulse frequency of 10 Hertz, the resulting thrust is 38.12 kN.

Other System Assumptions Used

- A current amplification factor of 25 has been used
- 80% of the energy extracted inductively from the thrust rings (in order to provide power for the next pulse) ends up as usable energy stored in the capacitor system.
- 50% of the energy stored in the capacitor system ends up as useful energy in the Z-Pinch.
- Useful fusion gain for the Z-Pinch is 3. That is to say if energy E is used to initiate the Z-Pinch, then the post-fusion kinetic energy of the expanding plasma shell is 3E.
- Energy lost through the open portion of the nozzle = 14.6% of total. This figure is roughly based on the geometry of the largest of the thrust rings.

Using the above assumptions, the following approximate energy balance has been used:-

Energy extracted inductively from the thrust rings during a pulse (in order to power the next pulse) ≡ E.

Energy stored in the capacitor system = 0.8E

Energy deposited in the Z-Pinch = $0.5 \times 0.8E = 0.4E$

Energy of expanding plasma shell (post-fusion) = $3 \times 0.4E = 1.2E$

Assuming 14.6% energy loss, this leaves a useful energy of 1.0248E. Of this a quantity E must be extracted to power the next pulse. This leaves 0.0243E, which is 2.369% of the energy before the extraction took place.

As energy is proportional to the square of total magnetic flux (Φ), this means that the extraction process effectively reduces the square of the flux as follows:

$$\Phi^2 \rightarrow 0.02369\ \Phi^2$$

This means that the drop in the square of magnetic field strength will be

$$B^2 \rightarrow 0.02369\ B^2$$

And hence

$$B \rightarrow \sqrt{(0.02369)}\ B$$

Which means that

$$B \rightarrow 0.1539B$$

In other words, just after the plasma begins to rebound (after its closest approach to the ring), the local magnetic field is assumed to drop to 15.39% of its value. This is a somewhat unnatural method of allowing for inductive energy extraction – and almost certainly has some impact on the subsequent plasma trajectory – but it does at least satisfy the overall energy balance requirements for the propulsion system. However, by the time this adjustment is applied, the expanding plasma shell has already deposited all its initial kinetic energy into the magnetic field and the outward expansion has been halted.

Table 3.1 contains the main electrical and mechanical performance parameters for each of the eight rings.

Table 3.1 Nozzle Ring Performance Parameters

Ring No.	Inductance ($T \cdot m^2/A$).	Initial (Seed Coil) Current (Amps)	Max. (Thrust Coil) Current (N)	Max. Axial Force acting on ring (N)	Max. Radial Linear Pressure* acting on ring (N/m)
1	3.85E-07	2.52E+07	6.58E+07	8.39E+07	2.74E+06
2	2.35E-06	4.13E+06	1.32E+07	5.49E+08	2.20E+07
3	4.99E-06	1.94E+06	6.57E+06	1.38E+09	5.57E+07
4	8.29E-06	1.17E+06	4.39E+06	1.93E+09	7.78E+07
5	1.24E-05	7.79E+05	3.25E+06	1.72E+09	6.95E+07
6	1.79E-05	5.42E+05	2.46E+06	1.03E+09	4.16E+07
7	2.54E-05	3.81E+05	1.83E+06	4.05E+08	1.65E+07
8	3.68E-05	2.63E+05	1.30E+06	1.02E+08	4.20E+06

* The radial linear pressure is defined as the integral of the outwards acting force around the whole 2π of the ring, divided by the circumferential length of the ring. Although a somewhat unconventional parameter, it can be used to derive the pressure stress that the ring needs to be able to withstand.

The maximum magnetic field experienced is about 17.7 Tesla.

4 MISSION ANALYSIS RESULTS

4.1 Mission Analysis

Current state of the art space propulsion systems limit human exploration to bodies in the Earth vicinity, with Mars as the most challenging destination typically considered. The long flight times to other more distant destinations represent risk and are not ideal for human exploration. Science missions are also limited to our solar system vicinity. The high specific impulse and moderate accelerations possible with the z-pinch fusion system can enable faster trip times to farther destinations with payload mass fractions similar to that predicted for state of the art chemical missions to Mars.

4.1.1 Mission Selection

To understand the benefits of developing a Z-pinch fusion propulsion system one must characterize its performance against potential missions of interest. A standard set of reference missions is offered in the AIAA special report titled "Recommended Design Practices for Conceptual Nuclear Fusion Space Propulsion Systems" (Williams 2004). Missions studied for this project are loosely based on the recommended missions in that publication and are defined below. The first of these missions was the basis for the vehicle conceptual design presented in section 5.

1. Piloted Mars round trip, 150 mt total useful payload to Mars, total round trip transit time ≤ 6 months (not including planet stay time), a reduced transit duration of ≤70 days was also considered.
2. Piloted Jupiter round trip, 150 mt total useful payload to Jupiter, total round trip transit time ≤ 3 years (not including planet stay time)
3. Robotic mission to flyby a distance 550 AU from the sun, 150 mt useful payload, ≤ 35 year one-way trip time

4.1.2 Ground Rules and Assumptions

Because of the short duration and limited resources available for this study several assumptions were made that simplify the required analysis. At some point the vehicle performance should be studied with more rigor, to ensure the complete cost of performing the selected missions is quantified.

- *No mass allocations are estimated to perform vehicle assembly*. The vehicle will require multiple launches from Earth and in-space assembly. One concept for assembly is that all of the pieces be taken to an Earth-Moon L1 base and assembled there, with crew joining only after assembly complete. No analysis has been performed to address the operations, the service equipment required, or the methods to transport the vehicle pieces and crew from the launch delivery orbit in LEO to the assembly area at L1.
- *Trajectories start and end assuming no influence of the gravitation of the departure and arrival bodies.* The trajectory analysis assumes a starting position and velocity equal to that of the Earth in solar inertial space, and a target position

and velocity equal to that of the destination body. This results in smaller than actual departure ΔVs (although if one neglects the propellant to reach L1, the ΔV to depart L1 is small.) The arrival ΔV at each destination is higher than it would be if you used a planets gravity to help capture the vehicle into orbit. No allocation of maneuver propellant for departing L1 to move beyond the Earth's sphere of influence is included. And no assumptions are made on the possible parking orbits at the destination bodies.

- *Payload mass is held constant*. Payload mass on the outbound leg of a round trip mission is the same as payload for the return trip. In actuality landers and cargo may be left behind at a destination prior to Earth return. Dropping mass at a destination will result in lower return ΔV and propellant loads than are reported here.

4.1.3 Methodology

Traditional chemical propulsion systems operate in the 1-g acceleration range allowing for the assumption of impulsive burns for trajectory analyses because the burn time is relatively short compared to the overall trip time. Propulsion systems operating in the low-thrust range (electric propulsion and solar sails) typically supply μ-g accelerations and require complex fully-integrated trajectory analyses due to the fact that burn times account for a very high percentage of the transfer time. The z-pinch propulsion system's milli-g accelerations place it in the category of "medium thrust" trajectory analysis. In order to properly assess trajectories associated with this type of propulsion system, the burns were numerically integrated and patched into a transfer conic trajectory.

The primary focus of this trajectory analysis was to determine the viability of medium thrust trajectories and to provide a high level assessment of the energies and propellant loads required to complete the missions in question. Several simplifying assumptions were made to allow for rapid assessment of multiple propulsion options and destinations. First, no ephemeris data was used to complete the analysis and simple circular orbits at the mean orbital radius were used to represent the departure and arrival planets. Therefore, while the results are valid for representing required energies for the transfer, the epoch of the mission and stay time at the destination were not quantified in this analysis.

Second, a simple orbit-to-orbit transfer was modeled. These transfers were segments of either elliptical or hyperbolic sun-centered orbits depending on the trip time and resulting departure velocity requirements. At either end of these transfers, a numerically integrated burn calculation was performed to quantify the burn duration and resulting propellant load requirement for the main burns of the trajectory. For round trip missions, these burns included the departure and arrival burns for each leg of the trip. The departure and arrival conditions for each leg were set at a v infinity of 0 km/s with respect to the departure and arrival bodies.

Finally, the planetary orbit component of the trajectories was not assessed. No parking orbit analysis was performed. Therefore, the energies associated with escaping the departure planet's gravity field are not accounted for and the propellant loads reported do not include propellant necessary for that escape burn.

4.1.4 Results

For the preliminary trajectory analysis, three missions were assessed. The first was a round trip mission to Mars, where the transfer time between Earth and Mars was set at 90 days. As a sensitivity to this, a 30 day transfer time was also assessed. The second mission was a round trip mission to Jupiter. The final mission assessed was a one-way fly-by of a distance 550 AU from the sun. In all cases, the burn-out mass of our vehicle was assumed to be 552 mT, which included payload mass. The thrust of the vehicle was assumed to be 38,120 N at a mass flow rate of 0.2 kg/s resulting in 19,346 seconds of specific impulse. The results of these missions can be seen in Table 4.1.

Table 4.1 Trajectory Results

	Mars 90	Mars 30	Jupiter	550 AU
Outbound Trip Time (days)	90.2	39.5	456.8	12936
Return Trip Time (days)	87.4	33.1	521.8	n/a
Total Burn Time (days)	5.0	20.2	6.7	11.2
Propellant Burned (mT)	86.3	350.4	115.7	194.4
Equivalent DV (km/s)	27.5	93.2	36.1	57.2

The plots in Figures 4.4 – 4.8 represent the trajectories for each of these cases. Figure 4.1 shows the outbound and return trajectories for a 90 day trip to Mars. This mission offers a 50% reduction in the nominal trip time to Mars with a 1.5 day departure burn.

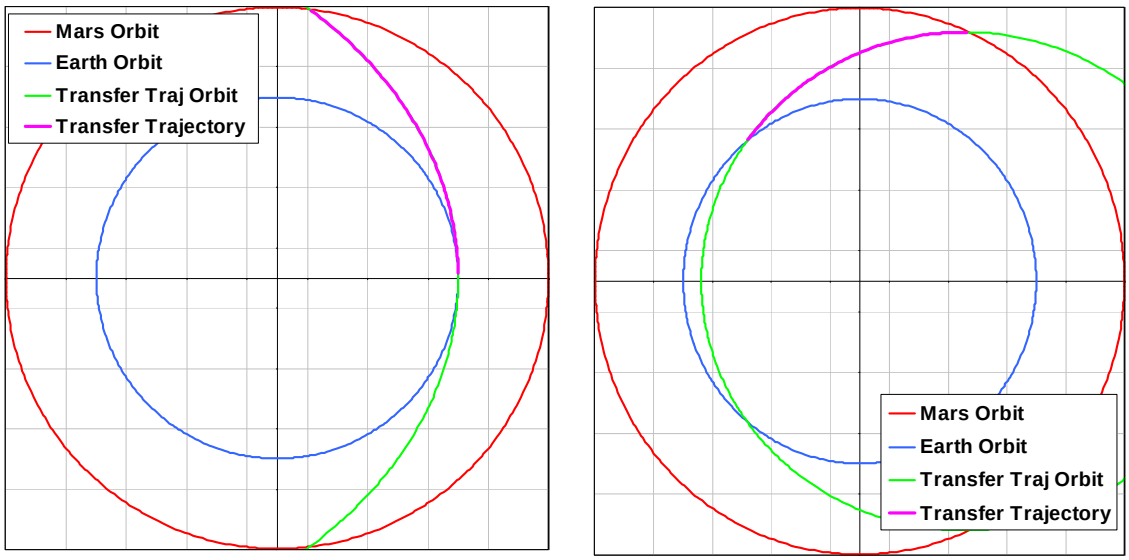

Figure 4.1 Mars 90 Day Transfer Trajectories

Figure 4.2 shows one of the integrated Earth departure burns as a representation of all of the integrated burns. In all plots, the burn time is so small compared to the coast time that these burns are not visible on the full trajectory plots.

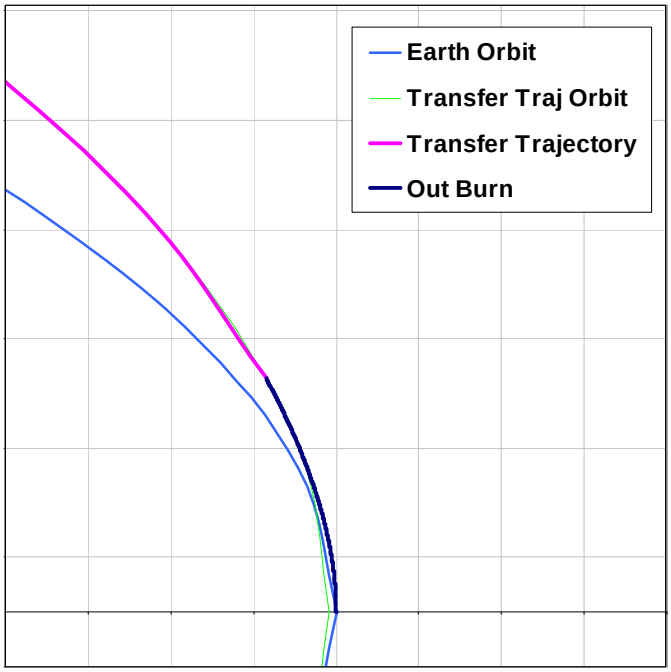

Figure 4.2 Representative Integrated Earth Orbit Departure Burn

Figure 4.3 shows a trajectory from Earth to Jupiter. The goal with this trajectory was to find a closed case with approximately the same propellant load as the Mars vehicle concept. For a propellant load of approximately 116 mT, the outbound trip to Jupiter is 1.25 years and the return trip is 1.42 years.

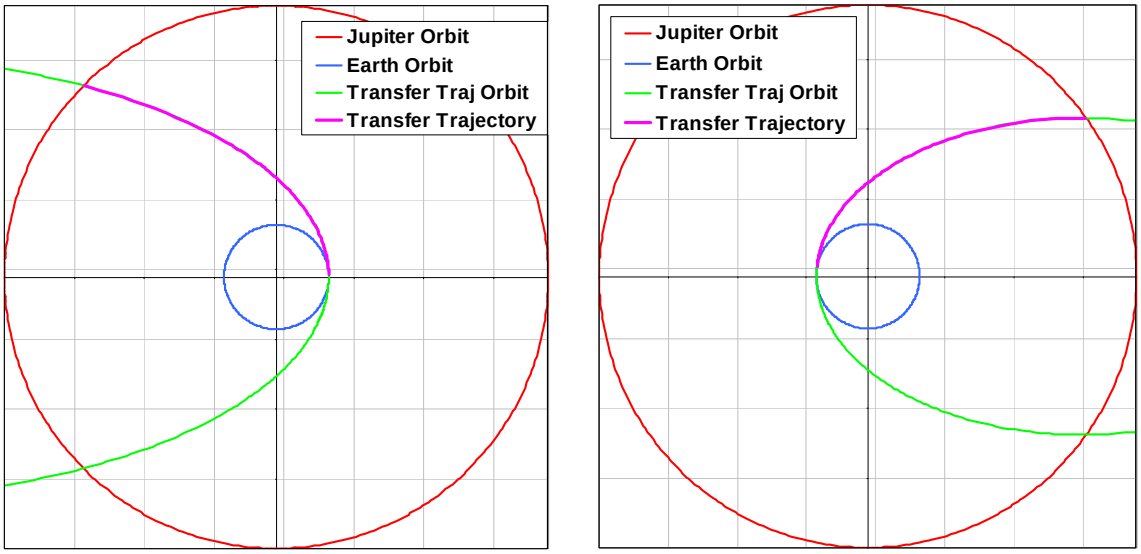

Figure 4.3 Jupiter Transfer Trajectories

Figure 4.4 shows a one way trajectory for a flyby of the region of space 550 AU from the sun. For less than 200 mT of propellant, the spacecraft will fly through the 550 AU mark in 35 years.

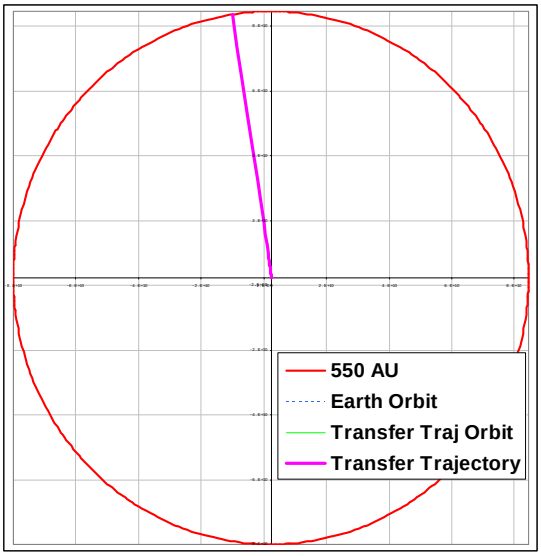

Figure 4.4 Trajectory to 550 AU

4.1.5 Varying Engine Performance

Variations in the design and operational assumptions of the Z-Pinch fusion propulsion system can result in different combinations of thrust and specific impulse. An additional performance point of 55,370 N of thrust and 28,080 seconds of specific impulse was studied. As expected, higher thrust and specific impulse will result in higher payload

mass fractions for the same mission. Figure 4.5 shows the payload mass fractions of the missions studied versus mission Delta-V. The higher data point on each line represents the performance for the higher thrust and specific impulse combination. For perspective, a payload fraction for a traditional system using chemical propulsion and aerobraking at Mars is given. This was calculated from Mars DRA 5 data (Drake, 2009) and corresponds to a 202 day flight time. This figure shows that the Z-Pinch fusion propulsion concept allows for significantly higher delta-v capacity (and shorter trip times) with comparable payload fractions. Figure 4.6 shows that this propulsion system will require significantly lower thrust for faster trips with lower propellant fractions than traditional chemical approaches.

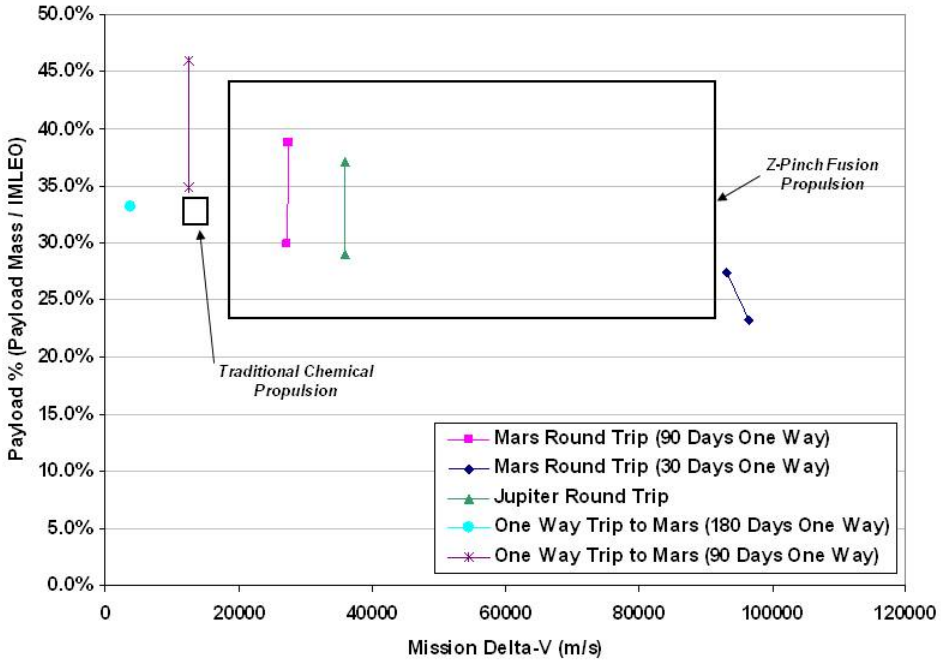

Figure 4.5 Payload Fractions for Z-pinch Fusion Systems

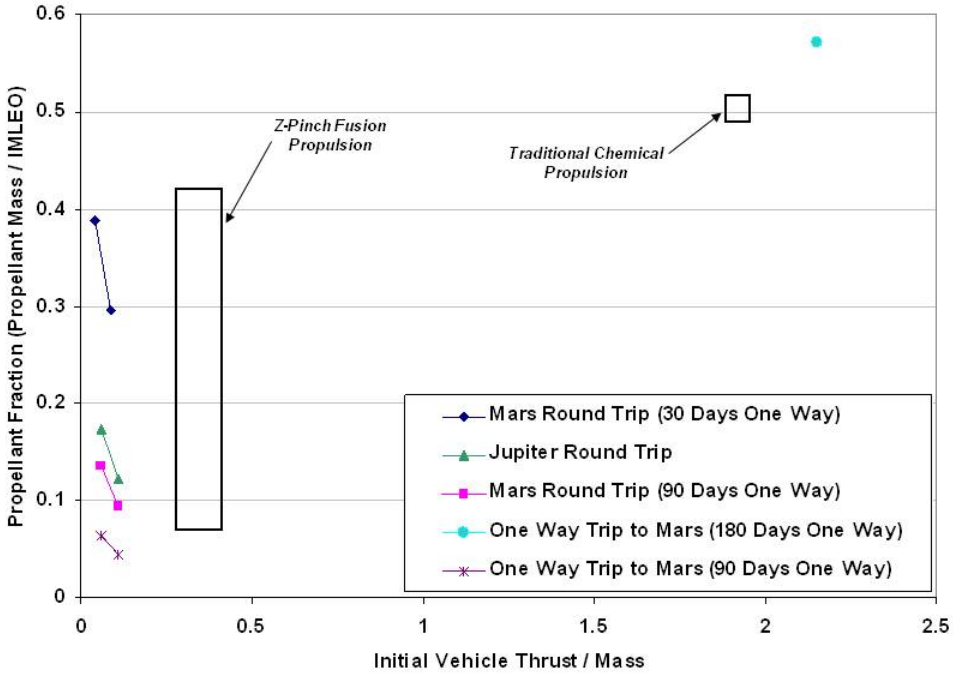

Figure 4.6 Propellant Mass Fraction vs Thrust/Initial Mass

4.1.6 Trajectory Validation

The approach described above was used to quickly assess performance for several missions, but made several simplifying assumptions and was not fully optimized. To confirm the validity of the results the outbound leg of the Mars round trip mission was analyzed using a higher fidelity software program, Copernicus. Using Copernicus potential round trip missions were studied using realistic orbit and ephemeris data.

Figure 4.7 represents an optimal 90-day outbound trajectory to Mars departing Earth August 1, 2035. The burn duration and direction at the departure and arrival ends of each trajectory were optimized to deliver the maximum payload mass for a fixed flight time. Departure date was also allowed to vary. Comparisons back to the previous quick look tool indicate an error in estimated propellant required of only 0.2%. This degree of agreement was surprising, but can be attributed to balancing of the effects of the circular coplanar orbits and non-optimized thrust direction in the quick look tool. With circular coplanar orbits the quick look tool will predict a lower total ΔV, but with non optimal thrust direction the ΔV would be higher than necessary. The final comparison shows a total ΔV that matches closely with the Copernicus prediction. The total ΔV predicted by Copernicus was 219 m/s higher than a Lambert solution for the same start and end conditions.

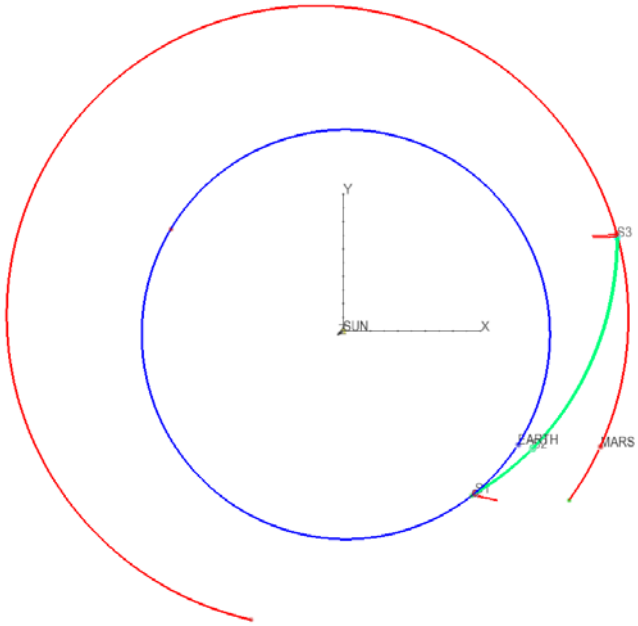

Figure 4.7 90-day Trajectory from Earth to Mars

Table 4.2 Trajectory Validation Results

	Quick Look Tool	Copernicus
Outbound Trip Time (days)	90.2	90.
Departure Burn Time (days)	1.51	1.16
Arrival Burn Time (days)	0.85	1.20
Departure Propellant Burned (mT)	26.297	20.102
Arrival Propellant Burned (mT)	14.716	20.832
Equivalent DV (km/s)	13.1	13.6

Regardless of the type of mission considered it is obvious that the z-pinch fusion rocket could significantly reduce trip times for crewed missions to the outer planets or asteroids, and could enable missions that would otherwise be impossible or impractical with current technology.

5 VEHICLE DESIGN

In order to assess the applicability of Z-Pinch fusion to interplanetary missions, the study team performed a conceptual design of a spacecraft suitable to a number of manned and unmanned missions in the solar system.

The overall design strategy for this vehicle is as follows:

1) The main propulsion system is designed around current Z-Pinch experimental equipment (e.g. the Z-Machine's DECADE Marx generator) adapted for flight use along with other components (e.g. magnetic nozzle) developed for other prolusion concepts. The required analytical parameters such as jet power, thrust, specific impulse, thermal output and others are derived from the propulsion models developed in the early phases of the study.
2) The Reaction Control System (RCS) and Thermal Management System are designed with current manned spacecraft technology specifically for this vehicle.
3) The spacecraft power and avionics systems are taken directly from other interplanetary studies so that the vehicle size and performance will be comparable to other interplanetary vehicles developed for similar mission profiles.
4) Spacecraft structures are designed to meet the specific needs of the vehicle and mission.

In comparing this vehicle to other concepts, it should be noted that this is not an optimized design. The time and resource limits for this study required that the designers be conservative in sizing vehicle subsystems, especially when these subsystems required novel approaches and components. Much future work is required to derive flight-weight components for the vehicle and as that work is completed, size estimates may be revised to reflect more realistic subsystem masses. Currently, the team's strategy is to be relatively conservative in sizing.

5.1 Configuration

The configuration is shown in Figures 5.1. and 5.2.

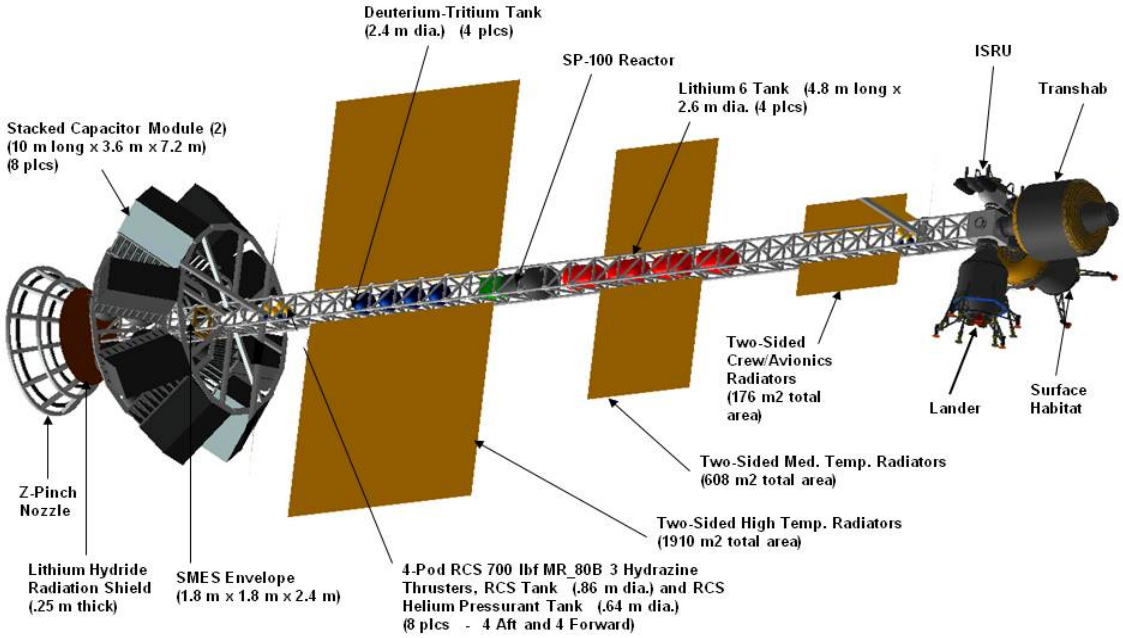

Figure 5.1 Configuration 1

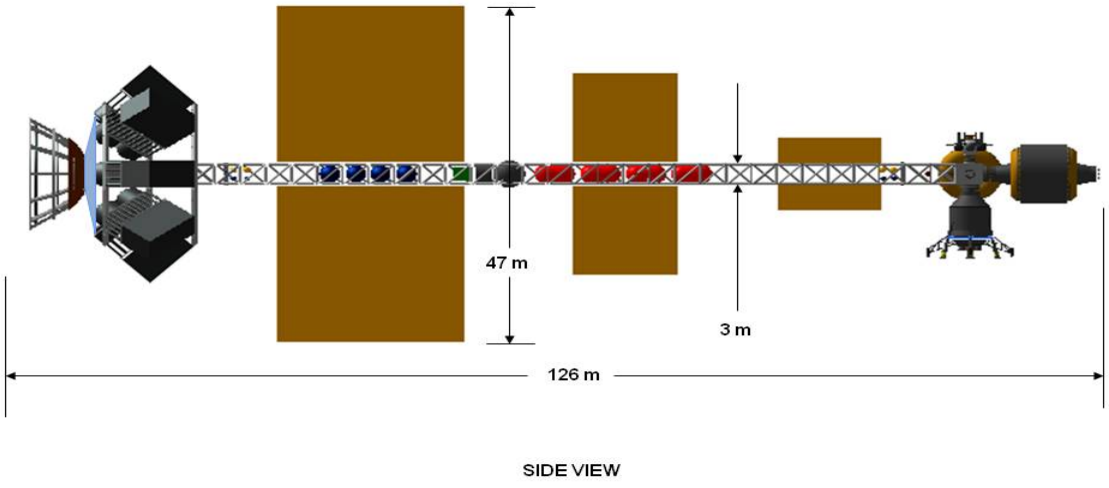

Figure 5.2 Configuration 2

5.2 Main Propulsion

5.2.1 Magnetic Nozzle Design

The nozzle consists of eight current-carrying rings, all of equal minor radius but with varying major radii. Figure 5.3 shows the overall nozzle, with the rings shown in yellow. Figure 5.4, showing the nozzle dimensions, defines the minor (a) and major (R) radii for a ring.

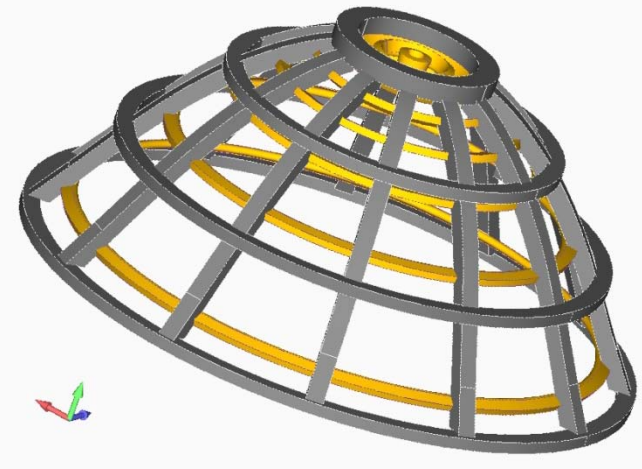

Figure 5.3 Nozzle Configuration

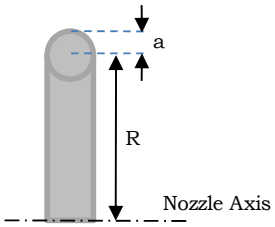

Figure 5.4 Nozzle Dimensions

Each ring is actually composed of two separate conducting rings. There is a superconducting ring that generates the initial seed magnetic field, which fills the volume of the nozzle before fusion takes place. The second conducting ring – a conventional (i.e. non-superconducting) one – supports the electrical current that is induced during plasma expansion. In addition to the two conductors there are various structural, cooling and neutron-protection features that must be incorporated in the design. Design details for one of the rings are illustrated in Figure 5.5.

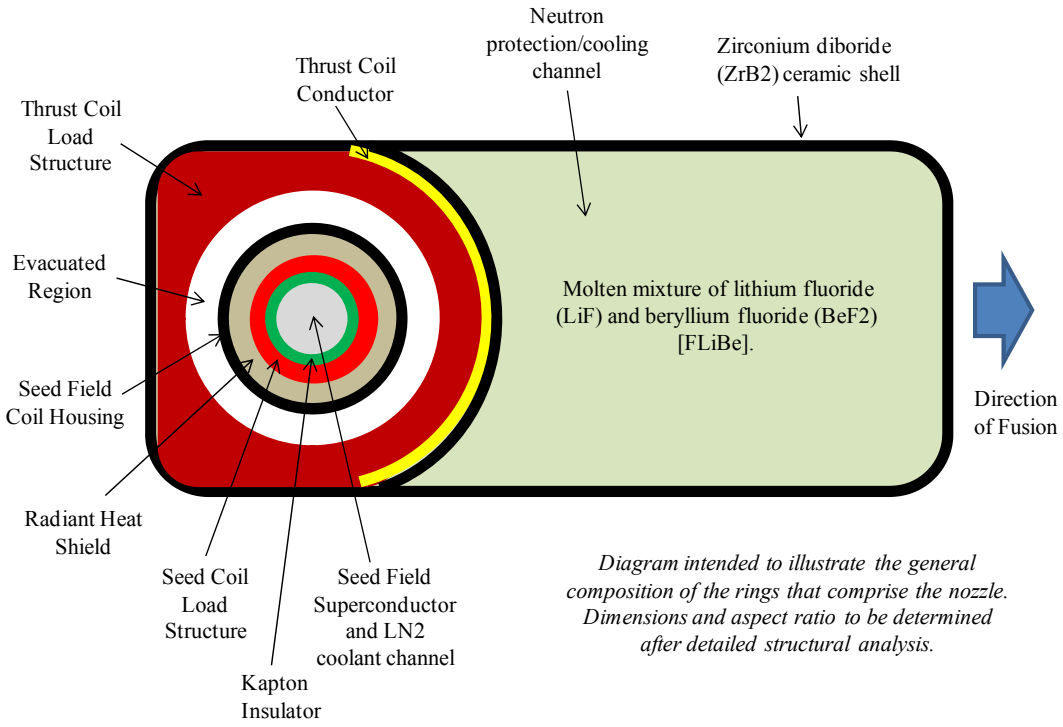

Figure 5.5 Composition of Rings Comprising the Nozzle

Note that the central (seed field generating) element consists of a high-temperature superconducting mesh immersed in liquid nitrogen coolant. An yttrium-based superconductor ($YBa_2Cu_3O_7$) is proposed. This has a transition temperature of 92 K, which allows it to be maintained in its superconducting state by LN_2 temperature at 77 K.

The main thrust coil conductor is made from a metal matrix composite consisting of molybdenum in a matrix of titanium diboride, which has a very low resistivity for a ceramic material. It offers relatively good electrical conduction and strength properties at high temperature.

The arrangement of 8 nozzle rings is shown below (Figure 5.6). They are positioned so that the centers of their electrical conductors (see Figure 5.5) all fall on a parabola with its focus 2 m from its apex. [They are positioned to have constant angular separation ($\Delta\theta$) when viewed from the focus of the parabola.]

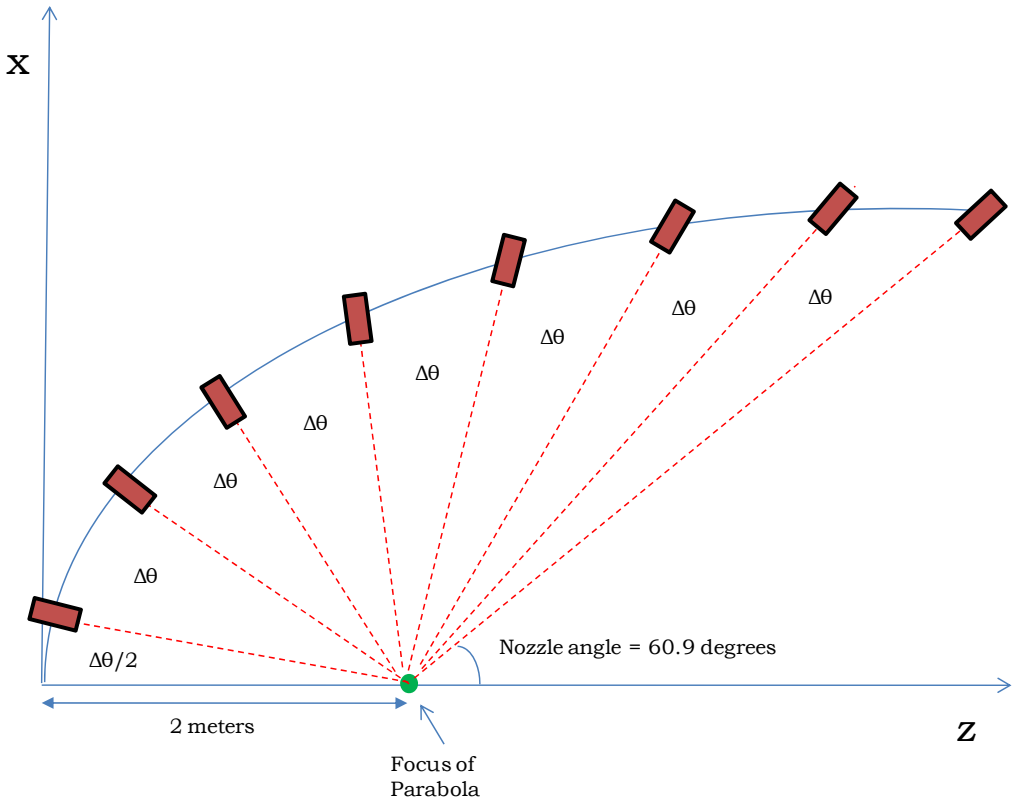

Figure 5.6 Arrangement of Nozzle Rings

The value of the inter-ring spacing angle (Δθ) is 15.9 °. This value is dictated by the 60.9° nozzle angle (which was itself explained earlier) and the decision to have eight rings, all with equal angular-spacing as seen from the focus. Note that the term nozzle angle in the diagram refers to the angle subtended by the 'open' portion of the nozzle as viewed from the focus. The portion of the plasma shell that expands in this direction is largely lost from the propulsion system and provides no useful impulse to the vehicle. [In practice the portion of the plasma that passes close to the final ring will interact with the magnetic field and so will provide some thrust, but the amount will be very small.]

In the above system of coordinates the parabola passes through the origin of coordinates and the ring positions and dimensions are as given in Table 5.1. Note that the ring major radius values apply at the center of the seed field superconductor (see Figure 5.8).

Table 5.1 Dimensions

Ring No.	z (m)	x – Ring Major Radius (m)	Ring Minor Radius (m)
1	0.0096	0.278	0.01
2	0.089	0.844	0.01
3	0.261	1.44	0.01
4	0.556	2.11	0.01
5	1.04	2.88	0.01
6	1.82	3.82	0.01
7	3.19	5.05	0.01
8	5.79	6.81	0.01

Precise dimensions for the conductive portions of the rings have yet to be determined, but they constitute a relatively small fraction of the overall nozzle mass. Figure 5.7 shows some of the conduction rings enclosed by the nozzle thrust structure (which consists of splines and outer structural rings).

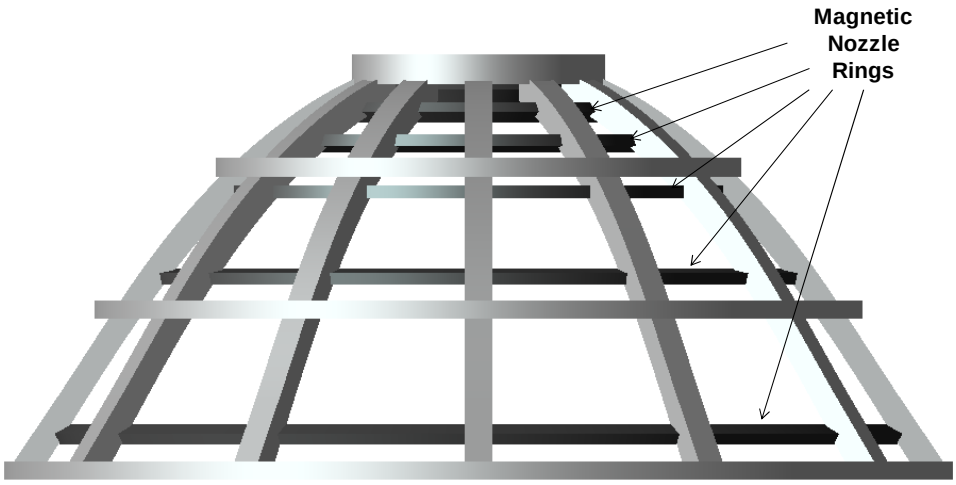

Figure 5.7 Conduction Rings Enclosed by Nozzle Thrust Structure

Dimensions for the conductive portions of the rings must be carefully tuned to allow both the seed and the thrust coils to operate effectively. As shown in Figure 5.8, the superconducting seed-field coil is positioned outside the normally-conducting thrust coil (which has a roughly semicircular cross-section).

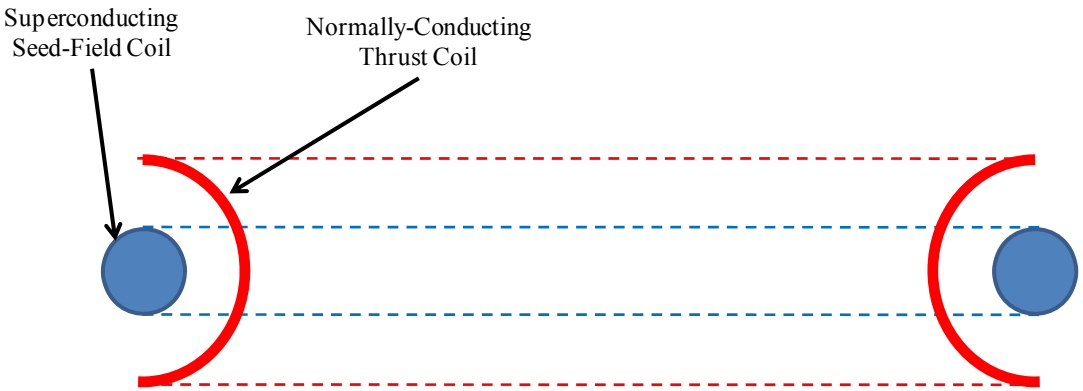

Figure 5.8 Superconducting Seed-field Coil Position

The seed magnetic field – which occupies the nozzle *before* fusion – is produced by a current flowing in the seed-coil. When this current first begins to flow, the resulting magnetic field propagates inwards from these coils to the interior of the nozzle. As shown above, the field must pass through the (normally-conducting) thrust coil before reaching the nozzle interior region. When it reaches the thrust coil, there will be a tendency for a counter-current to be induced in this coil. If fully developed, this counter-current will oppose the seed magnetic field and effectively prevent it from going further into the nozzle. If this were to happen the magnetic nozzle could not operate correctly.

The key to successful propagation of the seed field lies in the detail of what takes place when it encounters the electrically conductive thrust coil. The induced counter-current extends into the coil itself, but attenuates rapidly – as does the magnetic field. The current density profile and consequent magnetic field penetration are illustrated in Figure 5.9.

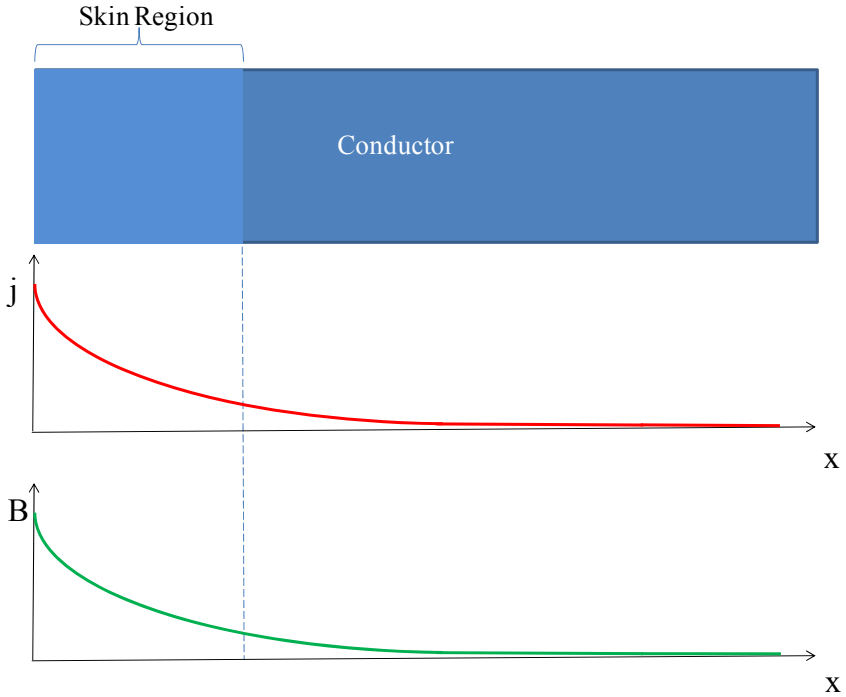

Figure 5.9 Density Profile/Magnetic Field Penetration

The 'skin' region is defined as that across which the induced current density reduces by a factor of 1/e. It is a characteristic of the material and the timescale on which the encroaching B-field changes. A conductor that is much thicker than the skin depth will prevent the B-field from passing through and emerging at the other side. Conversely a conductor which is not as thick as the skin depth will allow the B-field to pass through almost without attenuation.

The design problem for the thrust coils is that they must allow the seed field to pass through so that it can fill the nozzle interior region; however they must not permit the strong magnetic field that builds up in the interior during plasma expansion (after fusion) to pass through. These two contradictory requirements can be met if one considers the equation for skin depth (δ).

$$\delta = \sqrt{\frac{\rho}{\pi f \mu}}$$

Where ρ is the resistivity of the conductor; f is the frequency (in Hertz) of the incident magnetic field; and μ is the absolute magnetic permeability of the conductor. Replacing f by $1/\tau$, where τ is the timescale on which a magnetic field builds up, one gets

$$\delta = \sqrt{\frac{\rho \tau}{\pi \mu}}$$

From this it can be seen that the skin depth is proportional to the square root of τ. Hence for a magnetic field that builds up relatively slowly, the skin depth is relatively large, while for a field that increases very rapidly, the skin depth is very small.

Fortunately the timescale for buildup of the seed field is quite long – of the order of 10 to 50 milliseconds (although this will depend on the propulsion system pulse repetition frequency). On the other hand the timescale for the buildup of the magnetic field within the nozzle due to plasma expansion (after fusion) is much shorter – of the order of 1 to 10 microseconds. Hence the ratio of the two skin depths is given by the following approximate range of vales.

$$\frac{\delta_{Fusion}}{\delta_{seed}} = \sqrt{\frac{\tau_{Fusion}}{\tau_{seed}}} \approx \sqrt{\frac{1\times10^{-6}}{50\times10^{-3}}} \rightarrow \sqrt{\frac{10\times10^{-6}}{10\times10^{-3}}} = 0.0045 \rightarrow 0.032$$

To satisfy both the seed-field and post-fusion field requirements, a thrust coil conductor which has a thickness that is intermediate between the fusion and seed field skin depths is needed. Now the worst case ratio from the above expression is the larger one (0.032). In this case the seed field skin depth (δ_{seed}) is 31.25 (i.e. 1/0.032) times greater than the post-fusion field skin depth (δ_{fusion}). Selecting an actual conductor thickness of about 5 times δ_{fusion}, should prevent any post fusion B-field from passing through, while being only about one-sixth of $\delta_{seed,}$ allowing the seed B-field to pass through with little attenuation.[1]

[1] Although copper is not a suitable material for this high-temperature application, it can serve to provide an example. When τ = 1 microsecond, the skin depth is about 0.07 mm. When τ = 20 milliseconds, the skin depth is about 9 mm. Hence – for this example – a conductor thickness of 1-2 mm would meet both requirements. It would allow the seed field to pass through without attenuation, but it would prevent the post-fusion field from passing through.

5.2.2 Z-Pinch Regeneration / Discharge System

In order to create the conditions necessary for fusion, a very large (333 million Joules) amount of energy must be applied to the DT fuel bolus over a period of just around 100ns. In order to do this, capacitor banks must be employed that have a very low capacitance (so that the discharge will be very rapid) at a very high voltage (in order to store enough energy). These capacitor banks must then be recharged before the next fusion pulse. During the fusion part of the pulse, the conductive plasma expands against and compresses the magnetic field generated in the seed coils. This compressing field then induces a current in the thrust coils which is used to recharge the capacitors. The Z-Pinch Regeneration / Discharge subsystem consists of the capacitors, cables, switches and other circuitry required to charge and discharge the capacitors.

5.2.2.1 Ground Rules & Assumptions

1) The charging efficiency of the capacitors is 80%
2) The discharge efficiency to the Z-Pinch is 50%

Driving Requirements

1) The energy released from fusion is 1 GJ. Since the fusion gain has been calculated to be 3, the energy required to achieve Z-Pinch fusion is 333×10^6 J.
2) The charge time for the capacitors is 750 ns. This was calculated from the known velocity and pressure of the plasma during fusion and the physical dimensions of the magnetic nozzle.
3) The discharge time into the Z-Pinch is 100 ns

Methodology

Although the capacitors must be discharged over a 100ns period, they are recharged over a much longer period of time (750 ns). This would suggest that the capacitance of the banks required for charge should be somewhat larger than the capacitance at discharge. Since the inductance of each of the thrust coils is known, a minimum capacitance may be calculated for the capacitor bank to be charged by that coil. Since the discharge time period and energy are likewise known, the maximum discharge capacitance may be calculated as well.

The capacitance of a number of series connected capacitors

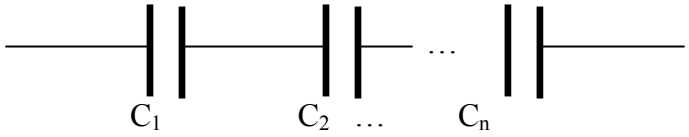

Is given by

$$\frac{1}{C_T} = \frac{1}{C_1} + \frac{1}{C_2} + \ldots + \frac{1}{C_n}$$

Where C_T is the total capacitance of the series.

In such a series, the total voltage of the series end to end is apportioned to each capacitor in the series in proportion to the inverse of its capacitance as well, allowing the series to handle much higher voltages than any of its constituents.

This series behavior is most convenient – if the capacitors may be charged in parallel (where the capacitance is larger) and discharged in series (where the total capacitance is smaller), then a circuit may be devised that allows a large bank of capacitors to be charged in 750ns and discharged in 100ns with very little loss.

This circuit is known as the Marx Generator. It was first described by Erwin Otto Marx in 1924. The basic form of the circuit is shown in Figure 5.10.

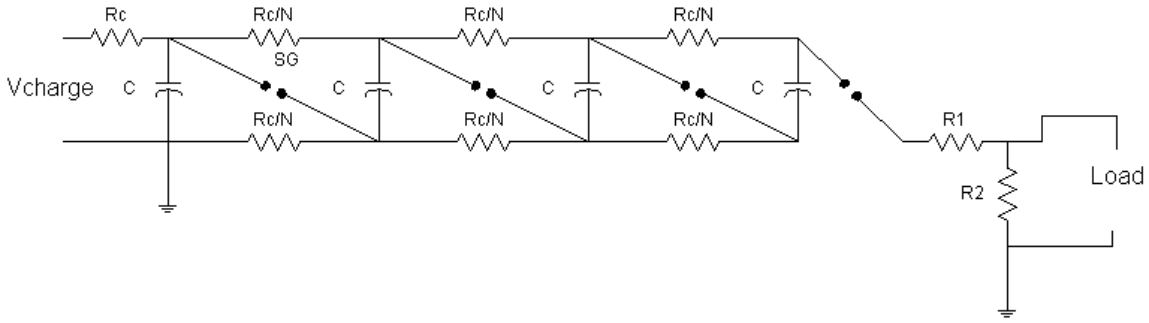

Figure 5.10 Basic Circuit Form

In this basic circuit, the capacitors charge in parallel through the Rc resistors. The gaps (shown as —• •—) do not conduct while charging. If the distance across the gaps is chosen well, and the first gap in the series is made to conduct by closing it with a solid conductor or conducting plasma, the increasing voltage across the other gaps will cause sparks to breach the gaps, ionizing the air between them and completing the series discharge circuit. Alternatively, the gaps can be closed by injecting plasma into a containment housing all of the electrodes.

In sizing a Marx generator for this application, individual capacitors consisting of TiB_2 plates separated with Lead Zirconate Titanate (PZT) dialectric are sized by traditional physics-based methods according to required voltage and capacitance. The plasma switches and diodes are not well characterized enough to size with a mass estimating relation, and so are sized as 12% of the capacitor mass.

Design Features

Figure 5.11 shows a basic schematic of the charge/discharge system.

Figure 5.11 Charge/Discharge System Schematic

The diodes prevent ringing between the capacitive and inductive portions of the circuit, while the plasma switches complete the series discharge circuit as for a typical Marx Generator. There are 8 stages in the Marx generator, arranged radially in a ring surrounding the Z-Pinch.

5.2.2.1 Mass Breakdown

The Mass Breakdown is shown in Table 5.2.

Table 5.2 Regeneration/Discharge Mass Breakdown

Subsystem Equipment List	Mass (kg)
Capacitor Banks	69776
Marx Generator Circuitry	4187
Total Mass	73963

5.3 Structures

5.3.1 Ground Rules and Assumptions

- The vehicle will be assembled in space, so only components small enough to launch as an assembled configuration, like tanks, would be analyzed for launch loads.
- The magnetic field generated in the nozzle will protect the materials of the nozzle and fusion engine from the extreme temperature of the fusion plasma.
- Deuterium/ Tritium storage tanks
    - 50% efficiency was assumed for D/T storage and delivery, so twice as much was tanked. This inefficiency was due to small molecule leakage and incomplete burn.
    - Gaseous 3000 psi D/T storage was used to minimize D/T leakage and avoid the need for cryogenic cooling.
- Radiation shielding is required for the vehicle, especially because the capacitor banks must be kept in close proximity to the top of the magnetic nozzle.
- The vehicle structural mass was largely based upon a previous study, HOPE/RASC MTF.

5.3.2 Driving Requirements

The dimensional and stress requirements of the magnetic nozzle are based on the fusion engine performance. These dimensions and forces were used to create a model to analyze nozzle structure and optimize its design and mass. Material susceptibility and shielding capability against fast neutrons produced by the fusion process are important in nozzle and vehicle configuration to minimize shielding mass.

5.3.3 Methodology

A Finite Element Model Analysis and Post-processing (FEMAP) model of the main propulsion nozzle was created in a simplified form. Material properties for C/C composite were used in Hypersizer® to optimize the nozzle structure for mass. The forces on the nozzle were applied against a fixed boundary that represented the vehicle or a very large mass, as a conservative approximation. See Figure 5.12. The "half-nozzle" component could be launched in this assembled form; the entire nozzle assembly is too large for today's launch vehicles (14 meters). This may require thermal control fluid couplings for LN2 and FLiBe. Also, the fuel injection manifold is not shown in this graphic. LN2 and FLiBe will be recirculated through the thrust coils and channels in the splines of the nozzle to a cryocooler. These are not depicted in Figure 5.12.

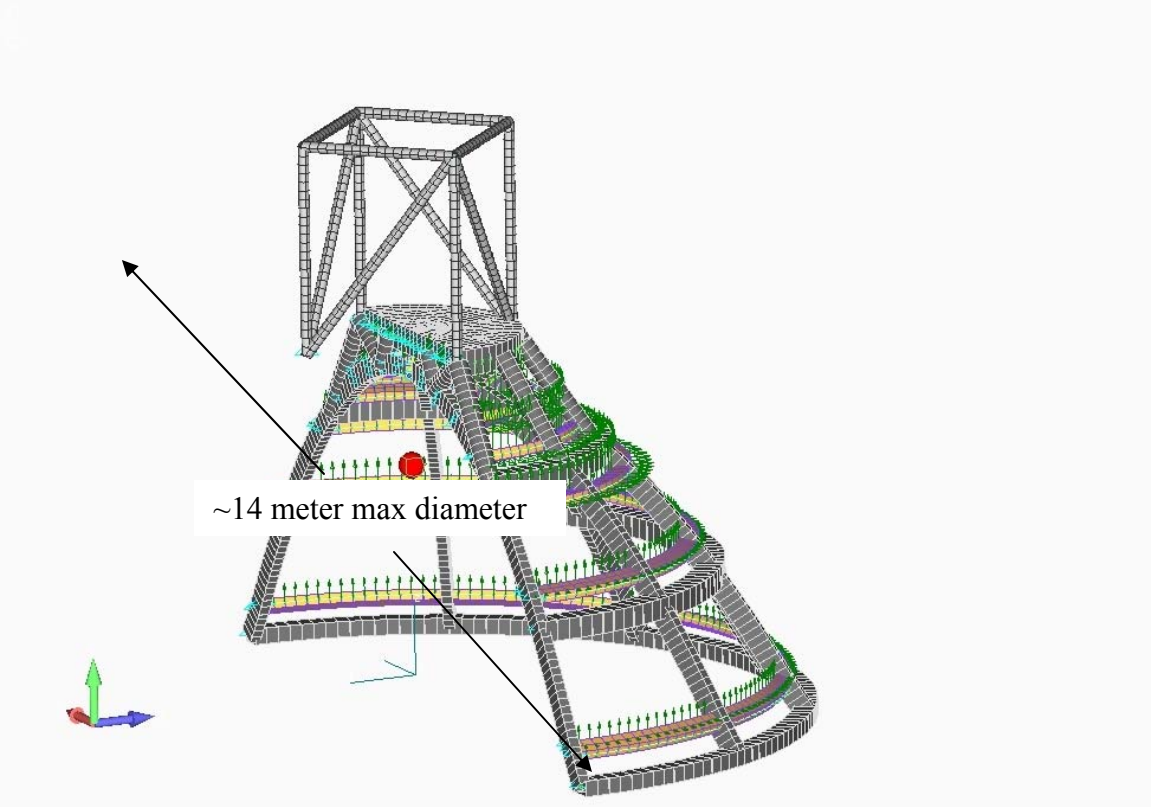

Figure 5.12 FEMAP finite element model of a half magnetic nozzle*

*Note: red sphere in Figure 5.12 indicates focus of Z-Pinch fusion pulses.

Neutron shielding mass was calculated by density and volume required to protect the vehicle materials, such as epoxy insulators (Hsu, et al. 2009). Gamma ray shielding was added to protect the crew. The D/T fuel and Lithium tank masses were calculated using tools that assume the tanks were launched from earth, so must withstand launch loads.

5.3.4 Design features

The Z-Pinch main propulsion engine's magnetic nozzle will be made of a Carbon Composite (C/C) material, such as a graphite epoxy composite IM7/8552, due to stiffness, light weight and carbon's ability to withstand neutron radiation. C/C fibers are produced at upwards of 95% carbon and can be woven and laid-up in several ply directions to produce 3-direction (3D) composite materials that have very high strength, and neutron withstanding capabilities. The thrust coils will be supported within the nozzle by being embedded in the 12 C/C splines.

The magnetic nozzle will require active cooling to maintain a temperature below the $YBa_2Cu_3O_7$ superconductor's transition temperature. Both LN2 and FLiBe were suggested for heat removal in the MTF magnetic nozzle design and these are retained in the Z-Pinch version. FLiBe also captures gamma rays and neutrons so acts a radiation shield for the thrust coils of the nozzle.

Radiation shielding is required for the vehicle, especially because the capacitor banks must be kept in close proximity to the top of the magnetic nozzle. The Li6 fuel will absorb

and carry away some neutrons and will slow down many more. A two-layer neutron shield, 25 cm thick, which includes a C/C shell to contain the shielding material, will fit like a cap over the magnetic nozzle. Lithium Hydride (LiH) will be used for the bulk of the neutron shielding because it slows down neutrons 50% better by mass than water (Carlson 1985), has essentially no vapor pressure and doesn't melt until 960 ° K. See Table 5.3. A small layer of boron carbide (B_4C) will also be part of the neutron shield to capture the thermal neutrons. Mixed lithium-boron hydrides may be even better (Joy 2006). Finally, a thin layer of Tungsten (W) is needed to reduce the gamma rays (Humble et al. 1995). See Figure 5.13 (Emrich 2010).

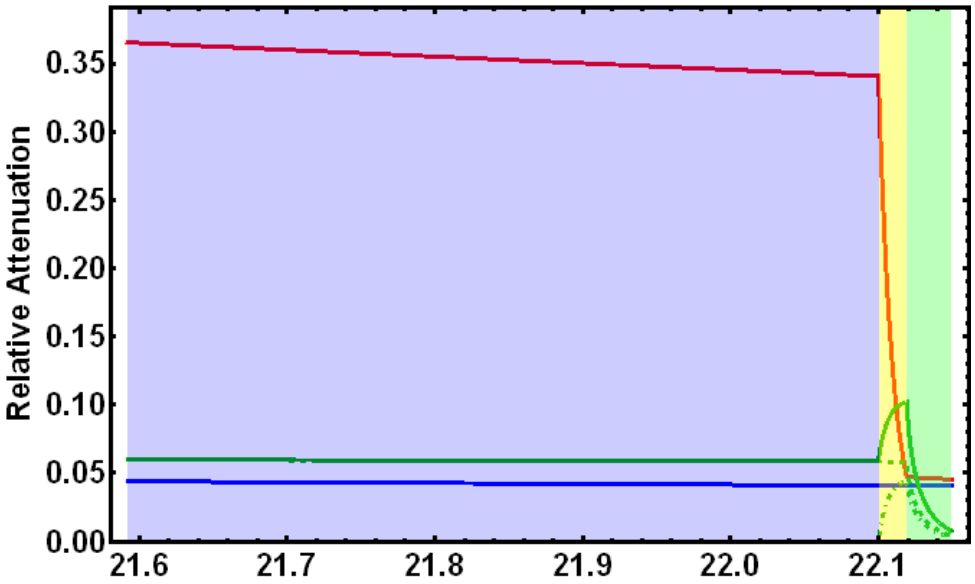

Figure 5.13 Radiation Shielding Thickness and Attenuation*

*Note: Blue = 14.1 MeV neutrons. Red = Thermal neutrons. Green = Gamma rays.

Table 5.3 Fast Neutron Removal Cross Sections of Materials

	(cm^{-1})	(cm^2/g)
LiH	0.110	0.152
H20	0.098	0.098
B_4C	0.118	0.051
C	0.084	0.047
$ZrH_{1.6}$	0.140	0.025
Fe	0.168	0.021
Zr	0.101	0.016
W	0.198	0.010
Pb	0.118	0.010

The "cap" radiation shield will extend down from the top of the nozzle, protecting a radial half angle wide enough to shield the capacitor banks and the entire vehicle. The half angle of neutron shielding will be much larger than the HOPE/RASC MTF shielding because the magnetic nozzle where fusion occurs must be located in close proximity to the large capacitor banks.

There will leakage of radiation around the fuel lines and coaxial leads to the capacitors in the area directly above the magnetic nozzle. These components will be embedded in additional LiH right above the Plasma Facing Component (PFC), probably a C/C manifold. It is expected that these components, the shielding, C/C manifold and the magnetic nozzle and thrust coils will have to be replaced periodically. In addition, a close-out skirt with a thin beryllium coating will extend from the top of the magnetic nozzle to the capacitor banks. This will deflect more neutrons that penetrate the radiation shield away from the vehicle.

A titanium lined Kevlar tank design will be used for D/T storage because it is a suggested design for H2 storage. D/T will be stored as a gas at 3000 psi to avoid needing a cryogenic thermal system and to minimize leakage. Liquid Li^6 will be stored at low pressure and low carbon steel was used in this analysis and yielded reasonable tank mass results.

The rest of the vehicle structure: truss, other primary structure such as capacitor bank attachment to truss, secondary structure, etc, will be aluminum. Mass estimated from the HOPE/RASC MTF vehicle study, is scaled proportional to total Z-Pinch vehicle length and mass. A mass for secondary structure, 20% of the primary structures, will also be added to the vehicle structural mass.

5.3.5 Mass Breakdown

The Mass Breakdown for Structures is shown in Table 5.4.

Table 5.4 Structures Mass Breakdown

Subsystem Equipment List	Ea (kg)	Total (kg)
Magnetic nozzle (less coils)	1	18,000
Radiation shielding	all	17,000
D/T tanks (dry)	1250	5,000
$Lithium^6$ tanks (dry)	500	2,000
Main vehicle truss	all	8,500
Other primary structure	all	2,000
Secondary structure	20% truss & primary structure	2,100
TOTAL		54,600

5.4 Reaction Control

5.4.1 Ground Rules and Assumptions

Objectives

The primary objectives of the reaction control system are as follows:

1. To control the vehicle during main propulsion system burns
2. To "flip" the vehicle (180 degrees) between the departure and arrival main propulsion burns
3. To perform any other non-primary maneuvering of the vehicle during the lifetime of the mission

Vehicle Characteristics

For the purposes of the reaction control sizing, the vehicle was assumed to be a consistent solid cylinder, 150 m in length about the central truss of the spacecraft. For the Mars 90-Day mission, the initial mass of the vehicle is assumed to be 635,227 kg, with a burnout mass of 552,089 kg, main propulsion system burns as detailed in Table 5.5.

Table 5.5 Thermal Main Propulsion System Burns for the Mars 90-Day Mission

Main Propulsion System Burn	Propellant Used (kg)
Burn 1: Earth Departure	25,310
Burn 2: Mars Arrival	14,176
Burn 3: Mars Departure	30,990
Burn 4: Earth Arrival	12,662

Trajectory results for the other missions of interest are outlined in Table 5.5. For the Mars 30-Day, Jupiter, and 500 AU missions, the propellant consumed during each of the primary burns will be calculated by dividing the total propellant load (in Table 5.6) by the total number of primary burns. For the Mars and Jupiter mission, the total propellant load is divided by the four primary burns, and for the 550 AU mission, only a single primary burn is assumed. For the Mars and Jupiter missions, the 180-degree vehicle flip maneuver is assumed to occur after the first and third primary propulsion system burns.

Table 5.6 Total Propellant and Primary Burns for Four Missions of Interest

Mission	Total Main Propellant (mT)	Primary Propulsion Burns	Propellant Used per Primary Burn (mT)
Mars 90-Day	83.1	4	(See Table 5.5)
Mars 30-Day	335.3	4	83.825
Jupiter	111.1	4	27.775
550 AU	186.4	1	186.4

Reaction control will be achieved via two separate systems, consisting of four pods of four thrusts each, at the fore and aft of the vehicle, for a total of 32 thrusters (fore and aft). Because of the relatively large scale for this vehicle, each pod of four thrusters will be separate from the other three pods in the vicinity (fore or aft of the vehicle). A reaction control system that shares working fluids (at the fore or aft of the vehicle) would experience a significant pressure drop along the diameter of the vehicle; hence, independent thruster pods are implemented. The pods will be connected via communication lines, to maintain control and coordination of the vehicle. Each thruster pod will be connected to propellant tank(s) and pressurant tank(s), with the appropriate lines, valves, and regulators. For both systems, a pressure-fed monopropellant (Hydrazine), with an average Isp of 220 seconds, was assumed.

Control during primary propulsive maneuvers is achieved by assuming that 2% of the primary propellant load is necessary for control of that burn. This 2% will be divided equally between the fore and aft reaction control systems, with additional propellant (20%) for contingency. And additional 20% margin was added to the final load, to account for uncertainties when dividing each fore and aft system into individual RCS pods. The 180-degree flip maneuver is assumed to be exactly 180-degrees (pi radians), and must occur after the departure burn, but before the arrival burn. Each mission considered allows for significant durations of coast time and will therefore not drive the thruster selection. Note that the 550 AU mission does not require a 180-degree flip maneuver.

The flip-maneuver is assumed to be a single-axis maneuver; therefore, the equation of motion can be reduced to a function of the thrust level, burn and coast times, moment of inertia, and moment arm. As such, the flip-maneuver will involve a total of 4 thrusters – 2 fore and 2 aft of the vehicle. Thrust levels will be selected that minimize the torque experienced by the vehicle, but enable a reasonable flip duration of, at most, 180 hours (7.5 Earth days).

5.4.2 Driving Requirements

As stated, the reaction control system must perform control during the primary propulsive maneuvers, and it must perform the 180-degree flip maneuver, within the allotted time, with minimal torque applied to the vehicle. Figure 4.20 shows the total time required for the flip-maneuver, as a function of the thrust of each of the four engines in a single pod. Furthermore, Figure 5.14 shows that the selected engine (the Aerojet MR-80B, described later) can perform the flip maneuver as slowly as 7.5 Earth days (using 7-lbf of thrust per engine) or as quickly as 1 Earth day (using 700-lbf of thrust per engine).

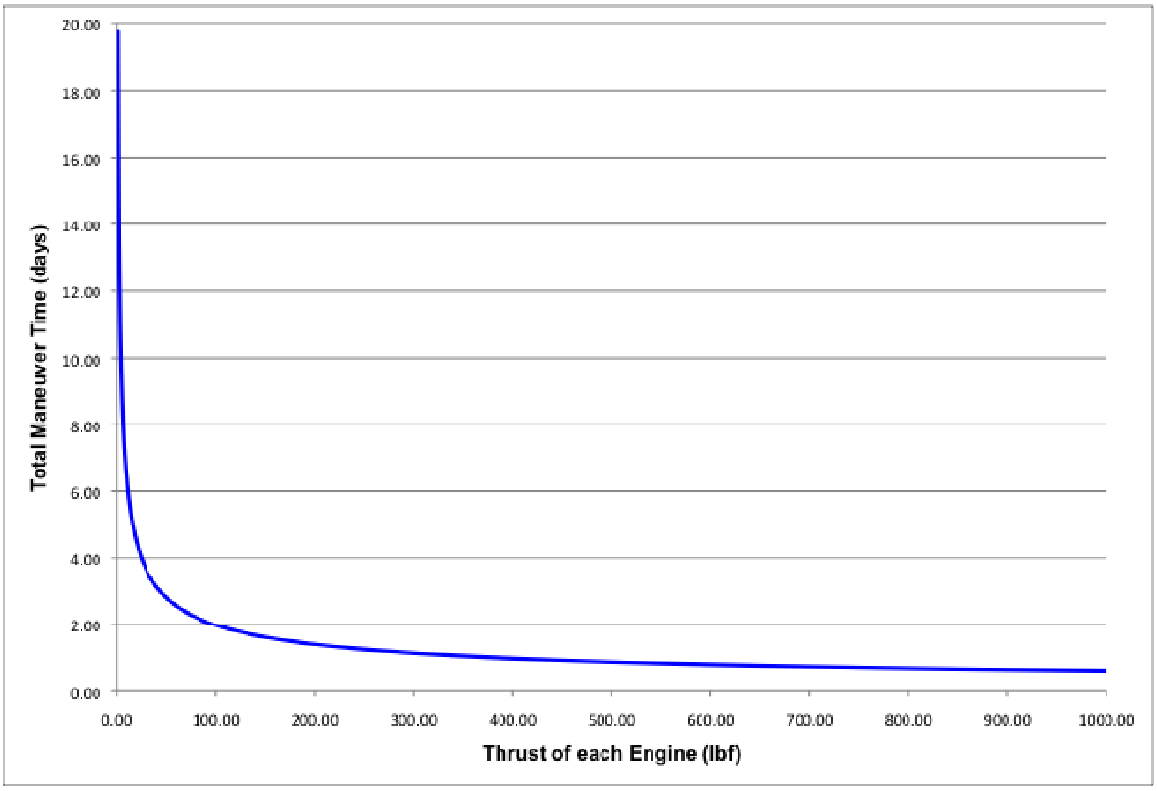

Figure 5.14 Total time Required for Flip-maneuver as a Function of Engine Thrust

Figure 5.15 (primary y-axis) shows the total propellant consumed during a single 180-degree flip-maneuver (this include propellant consumed to start the vehicle flip, and the propellant consumed to cease the maneuver). It can be seen that, even under the most inefficient case, the propellant consumed in virtually insignificant, less than 10 kg. Figure 4.21 (secondary y-axis) also shows the torque (in kN m) that the vehicle experiences using different engine thrust levels. Again, even under worst case conditions, the torqueses experienced by the vehicle do not exceed 1400 kNm.

Since the propellant required for the control of the primary propulsive maneuvers is 2% of those maneuvers, Table 4.8 shows that propellant load for these maneuvers far outweighs that required for the flip-maneuver. Furthermore, Figures 4.20 and 4.21 show that many different levels of engine thrust can accomplish the flip maneuver, without over-torquing the vehicle.

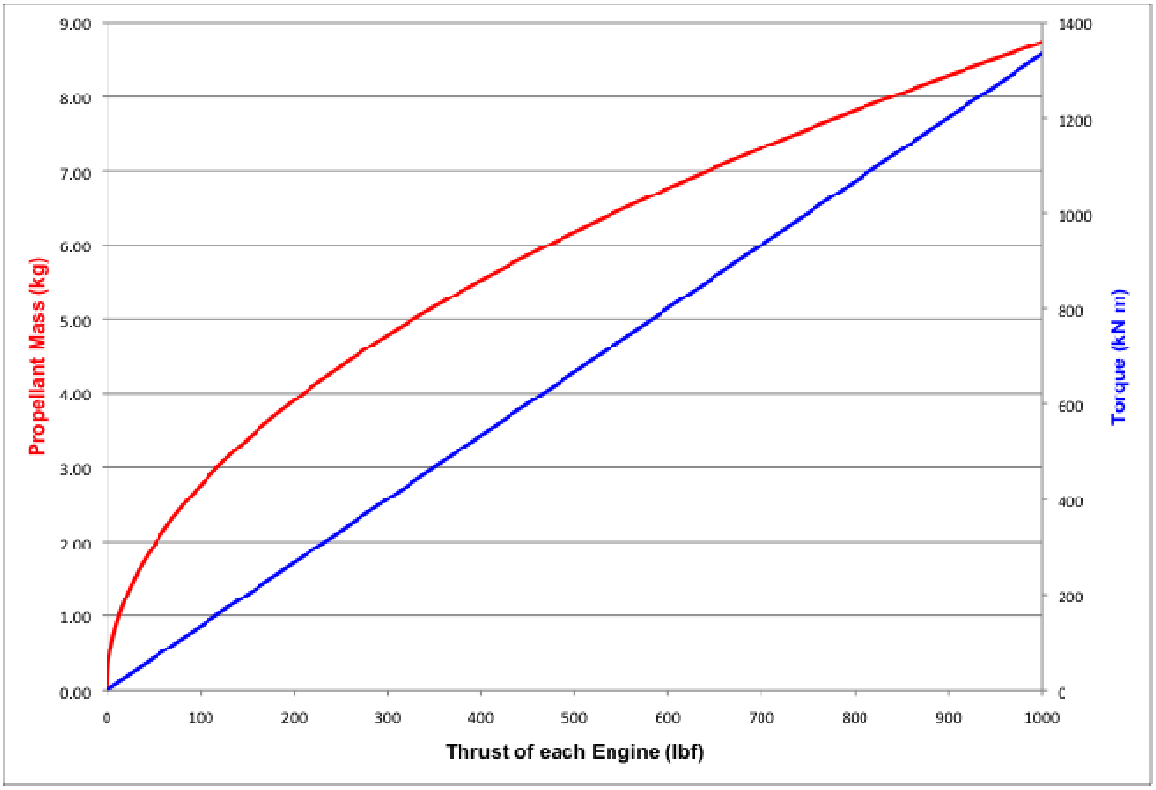

Figure 5.15 Propellant Consumed/Torque Experienced During a 180° Flip-maneuver*

*Note: Propellant mass is the curve on the left of the graph, while torque is the line on the right of the plot.

5.4.3 Methodology

The previous sections show that the propellant load for the RCS is determined by the total propellant load for the primary propulsive maneuvers. Because the propellant required for the flip-maneuver is so comparatively low, it is considered insignificant. Table 5.7 shows the total primary propellant load for each mission, the 2% RCS load, and how this 2% load was divided into the fore and aft reaction control systems, and then divided into individual pods.

Table 5.7 Propellant Loaded into Each 4-thruster Pod

Mission	Total Primary Propellant Load (mT)	2% RCS Propellant Load (kg)	1% (half the 2% load) + 20% for Contingency (kg)	Propellant in each Pod, including extra 20% Margin for Uncertainty (kg)
Mars 90-Day	83.1	1662	997	299
Mars 30-Day	335.3	6706	4023	1207
Jupiter	111.1	2222	1333	400
550 AU	186.4	3728	2237	671

Contingency (of 20%) was added to the propellant for the fore and aft reaction control systems because of the inefficiencies associated with dividing the total load into the two systems. Similarly, 20% margin, for uncertainty, was added to the propellant load for inefficiencies associated with dividing the fore and aft propellant loads into the 4 discrete pods. Therefore, the last column in Table 4.10 is the propellant that will be loaded into each of the 8 RCS pods (where there are 4 pods in the foreward RCS, and 4 pods in the aft RCS).

A monopropellant (hydrazine) engine was chosen to enable a large throttle range. Each pod will contain 4 hydrazine engines, one or more hydrazine tanks (sized to hold the propellant in the last column of Table 4.10), an appropriately sized pressurant (helium) tank(s), and components (lines, valves, etc) to connect the major elements.

5.4.4 Design Features

The numbers of tanks depends on the total propellant load, which is mission specific. It should be noted that, while the elements and pods are "independent" of each other – that is, they do not share propellant or pressurant – both elements and all pods are connected via a data and control system, such that both elements and all pods can act together to accomplish a task. The elements and pods were separated simply because of the size of the vehicle, and the pressure losses that would accompany fluid tubing of that length.

In the total reaction control system, all 8 pods will be identical. The four engines used in each pod will be the Aerojet MR-80B – a 700-lbf hydrazine thruster, capable of throttling down to 7-lbf. The MR-80B has the highest throttle ratio, at 100 to 1, which means that it can provide the small bursts of thrust required for the flip-maneuver, while still offering significant control authority when necessary. Furthermore, because a total of 8 MR-80B thrusters will aligned along the longitudinal axis of the vehicle, this gives an extra 5600-

lbf (approximately 25 kN) of thrust, along the axis of the vehicle, in the positive and negative directions. Figure 4.23 shows the MR-80B specification sheet – note that it is not a large thruster, and thus can be easily integrated into the vehicle. The MR-80B is scheduled to fly on the Mars Science Laboratory mission; but, it has heritage in the MR-80 thruster, which flew on the Viking Mars mission. Figure 5.16 shows a representation of the RCS pod schematic – additional pressurant and/or propellant tanks can be added as necessary for the mission. Figure 5.17 shows the thrusters used.

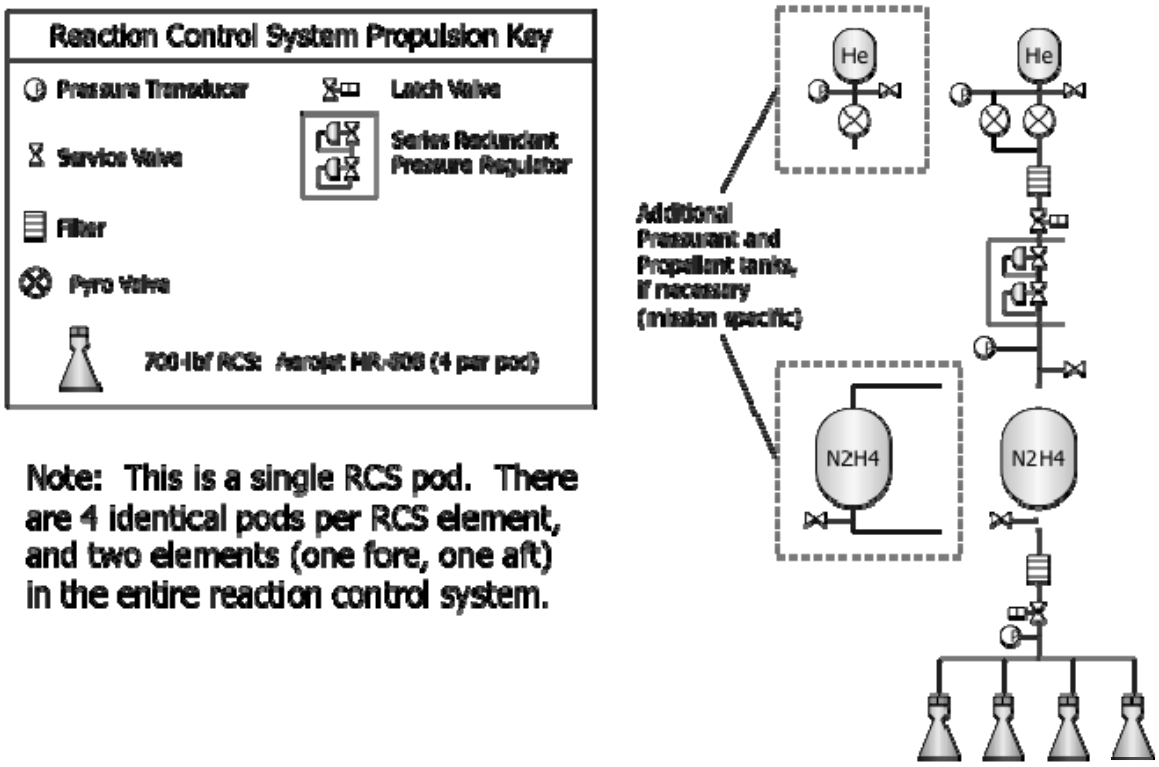

Figure 5.16 Schematic of the RCS Pod, Containing Four MR-80B Thrusters

MR-80B 3,100N (700-lbf) ROCKET ENGINE ASSEMBLY

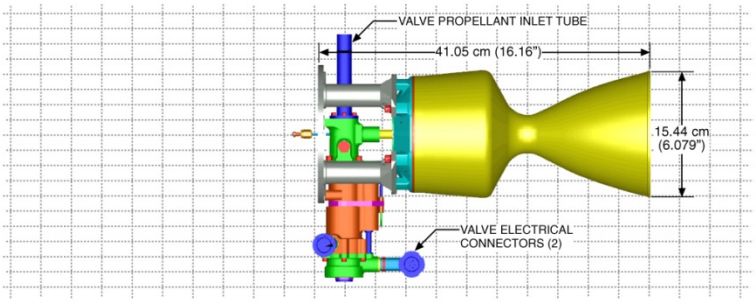

Design Characteristics

- Propellant . . . . . Hydrazine
- Catalyst S405
- VacuumThrust/Steady State . . . . . 3184 – 31N (716 – 7 lbf)
- Feed Pressure . . . . . 369 Bar (535 psia)
- Chamber Pressure . . . . . 171 – 0.14 Bar (248 – 2 psia)
- Expansion Ratio 16.7:1
- Cat. Bed Heater Pwr . . . . 15 Watts/Element Max @ 28 Vdc
- Valve . . . . . Cavitating Throttle
- Valve Power . . . . . 168 Watts Max @ 28 Vdc
- Weight . . . . . 7.94 kg (17.5 lbm)
  - Engine . . . . . 6.35 kg (14.0 lbm)
  - Valve . . . . . .1.59 kg (3.5 lbm)

Performance

- Vacuum Specific Impulse . . . . . 231- 200 sec (lbf-sec/lbm)
- Total Throughput . . . . . 342.5 kg (755 lbm)
- Steady State Firing . . . . . .137 sec – Single Firing
  . . . . . 715 sec – Cumulative

Status

- In Development

Reference

- JP&P-1992: Volume 8, No. 2, P. 320-331

Figure 5.17 Aerojet MR-80B - 700 lbf, Hydrazine Thruster, Used in Pods

5.4.5 Mass Breakdown

The reaction control system was sized for four missions of interest, outlined in Table 4.8. For each system, the components remain relatively unchanged – the number of pods and thrusters per pod remain the same, only the propellant load, and therefore the number and size of propellant and pressurant tanks, change. The propellant loads for the missions are detailed in Table 5.7. The masses for each pod of the reaction control system, for the specific missions of interest, are listed in Tables 5.8 – 5.11.

Table 5.8 Mass Breakdown for the Mars 90-Day Mission, Per Pod

Component	Description	Unit Mass (kg)	Quantity	Total Mass (kg)
Fluids				
Propellant	Hydrazine	300	1	300
Pressurant	Helium	5	1	5
Hardware				
Propellant Tank	Titanium spherical, 400 psia, 0.86m diameter	17.53	1	17.53
Pressurant Tank	COPV, spherical, 4500 psia, 0.64m diameter	18.7	1	18.7
Engines	MR-80B	7.94	4	31.76
Valving	Valves, lines, regulators, etc	5.26	1	5.26
Contingency	30% growth, applied only to dry mass	23.48	1	23.48
Total Pod Dry Mass				96.7
Total Pod Wet Mass				401.7
Total RCS Wet Mass (8x pod Wet Mass)				3213.6

Table 5.9 Mass Breakdown for the Mars 30-Day Mission, Per Pod

Component	Description	Unit Mass (kg)	Quantity	Total Mass (kg)
Fluids				
Propellant	Hydrazine	1207	1	1207
Pressurant	Helium	15.75	1	15.75
Hardware				
Propellant Tank	Titanium spherical, 400 psia, 0.87m diameter	17.6	4	70.5
Pressurant Tank	COPV, spherical, 4500 psia, 0.80m diameter	36.35	2	72.7
Engines	MR-80B	7.94	4	31.76
Valving	Valves, lines, regulators, etc	21.15	1	21.15
Contingency	30% growth, applied only to dry mass	63.56	1	63.56
Total Pod Dry Mass				259.7
Total Pod Wet Mass				1482.5
Total RCS Wet Mass (8x pod Wet Mass)				11,860

Table 5.10 Mass Breakdown for Jupiter Mission, Per Pod

Component	Description	Unit Mass (kg)	Quantity	Total Mass (kg)
Fluids				
Propellant	Hydrazine	400	1	400
Pressurant	Helium	6.7	1	6.7
Hardware				
Propellant Tank	Titanium spherical, 400 psia, 0.76m diameter	11.94	2	23.88
Pressurant Tank	COPV, spherical, 4500 psia, 0.7m diameter	24.56	1	24.56
Engines	MR-80B	7.94	4	31.76
Valving	Valves, lines, regulators, etc	7.16	1	7.16
Contingency	30% growth, applied only to dry mass	28.21	1	28.21
Total Pod Dry Mass				115.6
Total Pod Wet Mass				522.3
Total RCS Wet Mass (8x pod Wet Mass)				4178.4

Table 5.11 Mass Breakdown for 550 AU Mission, Per Pod

Component	Description	Unit Mass (kg)	Quantity	Total Mass (kg)
Fluids				
Propellant	Hydrazine	671	1	671
Pressurant	Helium	8.75	1	8.75
Hardware				
Propellant Tank	Titanium spherical, 400 psia, 0.78m diameter	13.26	3	39.77
Pressurant Tank	COPV, spherical, 4500 psia, 0.66m diameter	20.79	2	41.58
Engines	MR-80B	7.94	4	31.76
Valving	Valves, lines, regulators, etc	11.93	1	11.93
Contingency	30% growth, applied only to dry mass	40.14	1	40.14
Total Pod Dry Mass				165.2
Total Pod Wet Mass				845
Total RCS Wet Mass (8x pod Wet Mass)				6760

5.4.6 Summary

Just as this vehicle is scalable to many missions, the reaction control system was designed to be scalable, retaining as many common parts as possible. Overall system simplicity was also important in the RCS design; hence, a storable, pressurized monopropellant system, with a highly throttlable engine, was utilized. Notice that, in many cases, similarly sized pressurant and fuel tanks are also used – allowing for multiple tanks to be manufactured, and only included in the system when necessary.

The total reaction control system is divided into two identical elements, fore and aft of the vehicle, which each element consisting of four identical pods. No pods or elements share any fluids – because of the relatively large size of the vehicle, they are completely independent; however, they do share data on command and control, such that the entire system can act as one when performing maneuvers.

The RCS system is required to maintain control during primary propulsive maneuvers, perform a 180-degree flip-maneuver during the main propulsive coast periods, and perform any other non-primary maneuvering/control that might be required. The system described in this section meets all those requirements, while offering scalability and flexibility, and without applying too much torque/stress to the vehicle.

5.5 Thermal

The thermal subsystem comprises three separate heat rejection systems, which are described briefly in the following list:

1) A low-temperature radiator system for the avionics and crew
2) A medium-temperature (800 K) radiator for the power conversion system
3) A high-temperature (1250 K) radiator for the propulsion system waste heat including a cryo-fluid management system for the LN2 and FLiBe coolant loops that coil the Superconducting Magnetic Energy Storage (SMES) and superconducting seed coils.

The Figure 5.18 shows a block diagram of the thermal subsystem:

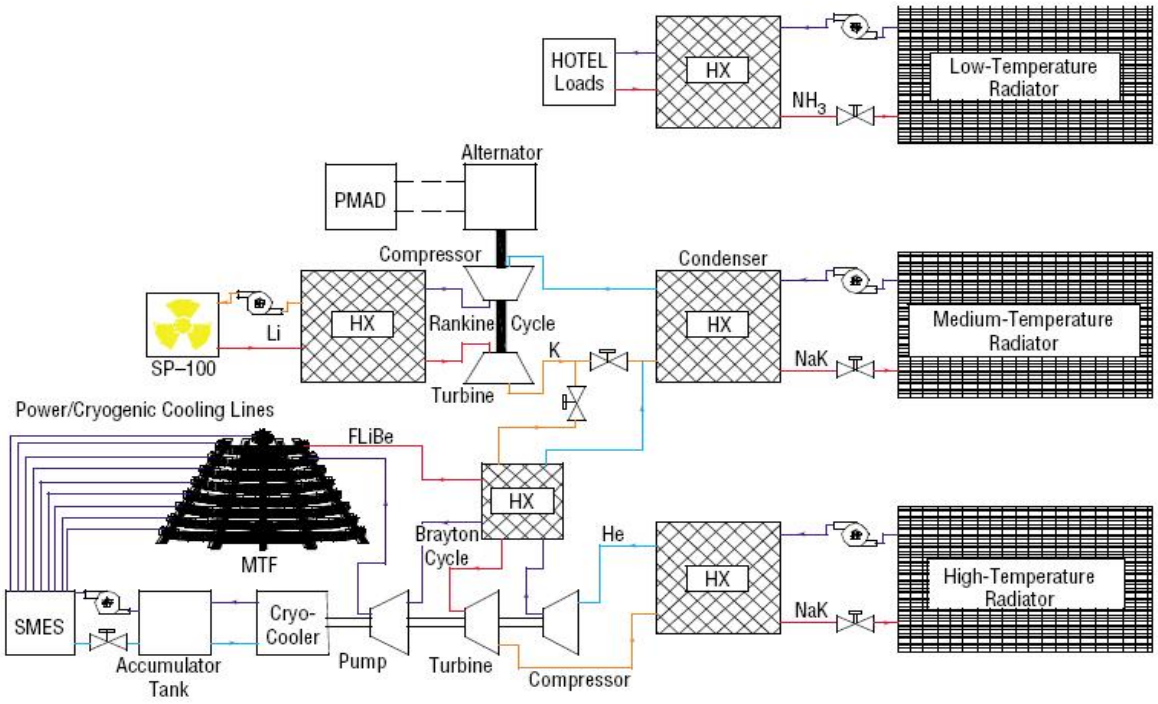

Figure 5.18 Thermal Subsystem Block Diagram

5.5.1 Ground Rules and Assumptions

1) The low-temperature radiator is assumed to view deep space (4 K). The medium and high temperature radiators are assumed to have a both-sides-combined worst-case view of 200K (one side facing a planet and the other side facing deep space).
2) All radiators are 2-sided. The low temp is assumed to have a planform areal density of 3.7 kg / m2, the medium temperature an areal planform density of 10 kg/m2, and the high temperature radiator a planform areal density of 16.7 kg/m2
3) The non-radiator thermal loop components (pipes, heat exchangers, pumps, etc.) are standard for the existing SP-100 reactor and Rankine cycle generator used. These are taken from a previous study. The working fluid is NaK. The working fluid of for both the high and medium tempature radiators is NaK.
4) The emissivity of all radiator surfaces is assumed to be 0.9.

5.5.2 Driving Requirements

1) The low temperature radiator for the avionics, Environmental Control and Life Support System (ECLSS), and habitat is assumed to require 172.5 kW. This is the power required by the 'Black Box' payload and crew module derived from the Human Outer Planet Exploration (HOPE) Magnetized Target Fusion (MTF) study (Adams et al. 2003).
2) The power generation system itself rejects 24.1 MW max at 800K. This requirement is taken from a previous study using the same generation system at the same power level.

3) The high temperature heat rejection system is required to reject 460.9 MW of thermal power. This number was obtained by estimating the amount of thermal radiation absorbed by the nozzle structure during the fusion pulses (10 / sec) in addition to 5% losses estimated for the Z-Pinch electrical charge/discharge system in the actual capacitors and cabling (not in the nozzle structure).

5.5.3 Methodology

Because the low temperature heat rejection system is sized to reject a specific thermal power from the payload, crew habitat, and avionics taken from a prior fusion study (Adams et al. 2003), the low temperature system was simply taken in its entirety from the same study.

The requirement for the medium temperature heat rejection system – derived from the SP-100 reactor, Rankine Cycle engine and generator thermal output – likewise came from the HOPE MTF vehicle. Because the radiators for this system are large, and our concept vehicle will spend time in planetary orbits (Earth, Mars, Jupiter), we thought it more appropriate to assume a view temperature of 200K rather than the deep-space view of 4K used for the HOPE MTF study. The medium temperature radiators were therefore resized to the HOPE MTF requirement (24.1 MW) using the 200K view temperature. The remainder of the medium temperature system (pumps, tank, fluid, heat exchanger) was taken directly from HOPE MTF (Adams et al. 2003).

The radiator for the high temperature heat rejection system was sized with a standard 2-sided radiator sizing tool using Ti as the radiator material throughout. The other components of the high temperature system (pumps, tank, fluid, heat exchanger) were taken directly from HOPE MTF (Adams et al. 2003).

The LN2 cryofluid management system for cooling the SMES and seed coils was also taken from the HOPE MTF study. In this case, the only mass available was the total mass of the system. The individual component masses were derived by apportioning the masses as per similar cryofluid management systems (Adams et al. 2003).

5.5.4 Mass Summary

Table 5.12 summarizes the components that make up the thermal subsystem.

Table 5.12 Thermal Subsystem Components

Low Temperature			1302
	Radiator	1302	
Medium Temperature			23808
	Radiator	6083	
	Pumps	1020	

	Tanks/HX	851	
	Fluid	916	
	Piping	14938	
High Temperature			41849
	Radiator	31841	
	Pumps	2324	
	Tanks/HX	1938	
	Fluid	2088	
	Piping	3658	
LN2 Seed Coil Cooling			10205
	Cryo-Coolers	1290	
	Controller	903	
	Radiator	3200	
	Insulation	4812	
Total Thermal Mass			77164

5.6 Power

With the exception of the Z-Pinch fusion propulsion system (which has its own power generation system), all spacecraft systems are powered by an SP-100 lithium cooled fast-spectrum nuclear reactor. The SP–100 reactor project was started in 1983 by Defense Advanced Research Projects Agency in cooperation with the Department of Energy. Its focus was to design and demonstrate technology to provide nuclear power at a wide range of power levels, from 100 kW to MMW, for space applications. It was designed to fi t in the Space Shuttle payload bay and to operate for 7 to 10 yr. It has found application in the areas of non-terrestrial ground based power, satellite weapon systems power, and space vehicle power and propulsion (Adams et al. 2003).

The SP-100 drives a Rankine Cycle engine and generator to perform the electrical power conversion. The Figure 5.19 illustrates the Power Subsystem:

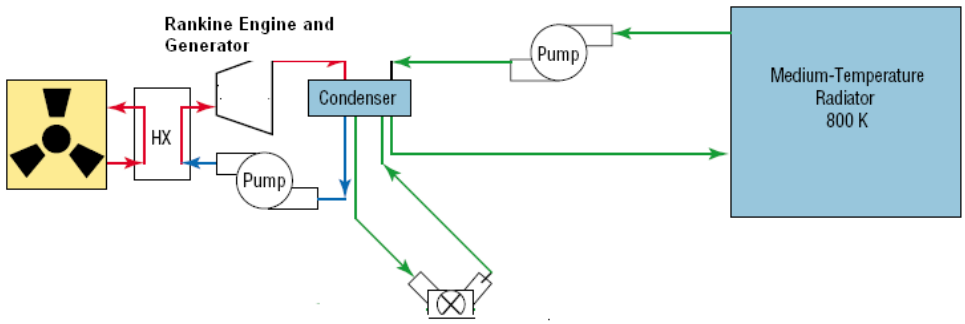

Figure 5.19 Power Subsystem

5.6.1 Ground Rules and Assumptions

1) All spacecraft power (except propulsion), payload, ECLSS and crew habitat is provided by the power subsystem. Power for the Z-Pinch propulsion engine is provided by a self-contained generation system.
2) Power required for all systems does not exceed 172.5 kW.

5.6.2 Methodology

The power subsystem was taken in its entirety from the HOPE Magnetized Target Fusion Study (Adams et al. 2003). There were three major reasons for that:

1) The payload (habitat, crew, ECLSS, etc) was assumed to be the same. Other powered spacecraft subsystems were either taken from that study or were comparable in their power requirements.
2) Maintaining consistency across various studies for similar mission and vehicle concepts affords the ability to compare and contrast them.
3) Using subsystems from a previous vehicle allows the team to spend its time on the challenges of Z-Pinch propulsion

5.6.3 Design Features

1) Thermal Power is provided by an SP-100 Lithium-cooled fast-spectrum fission reactor.
2) Power conversion is accomplished with a 375 kW electrical Rankine-cycle nuclear reactor with a net system efficiency of 19 percent. A typical layout of this system is shown in Figure 5.20, where LiH and tungsten radiation shielding dominates the mass and volume. This three-loop system heats lithium metal in the primary cooling loop and then carries heat from the reactor to the boiler. Potassium metal is evaporated in the boiler and expanded through a 10-pole homopolar turboalternator to generate the electrical power (300 kW nominal). Waste heat is removed from the turboalternator exhaust by exchanging with the third loop, which carries a heated NaK metal mixture to the radiators. Electromagnetic pumps are used in all of the liquid-metal cooling loops (Adams et al. 2003).

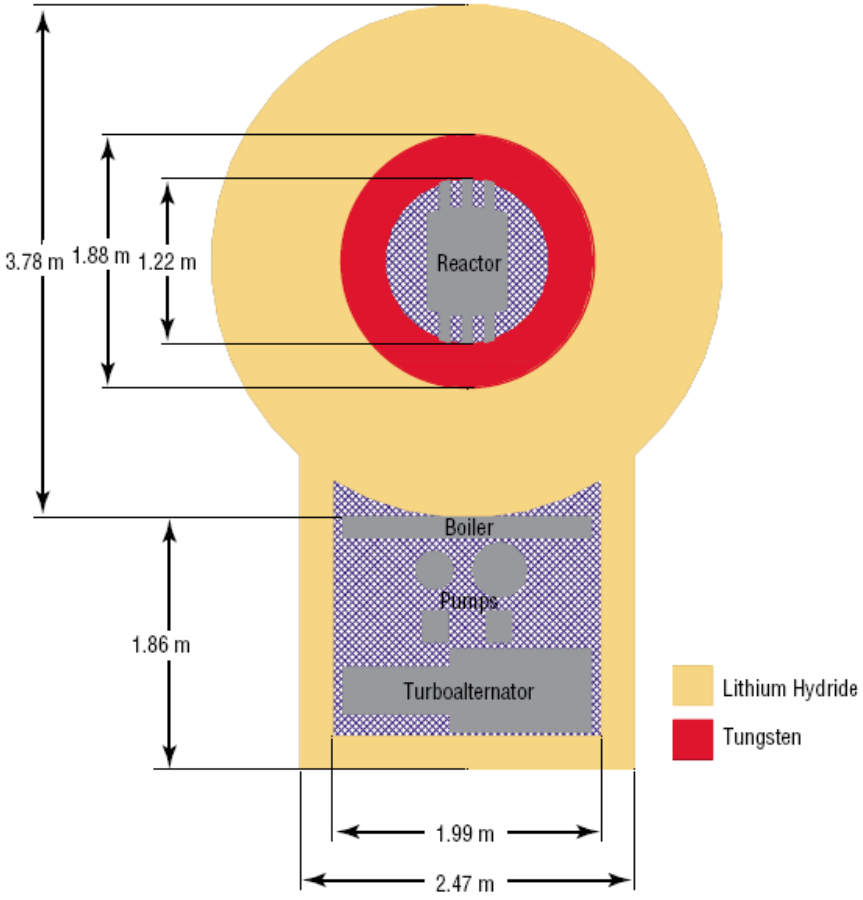

Figure 5.20 System Layout

5.6.4 Mass Breakdown

The Power Mass Breakdown is shown in Table 5.13.

Table 5.13 Power Mass Breakdown

Subsystem	Mass (kg)
Reactor	1810
Primary (Li) Loop	680
Power Conversion (K) Loop	1270
Main Heat Rejection (NaK) Loop	1575
Reactor Shielding	10000
Generator Cooling Loop	263
Turbine Cooling Loop	96
Electronics Cooling Loop	240
Ancillary Electrical Components	546
Total Power Mass	16480

5.7 Avionics

The avionics system includes Guidance and Navigation (G&N), Communications, and Command and Data Handling (C&DH) subsystems. The G&N subsystem includes everything needed to assess the spacecraft's location in space and its attitude. C&DH includes the flight computer and all other data processing elements, including data storage, telemetry, and command processing. Figure 5.21 shows an avionics schematic.

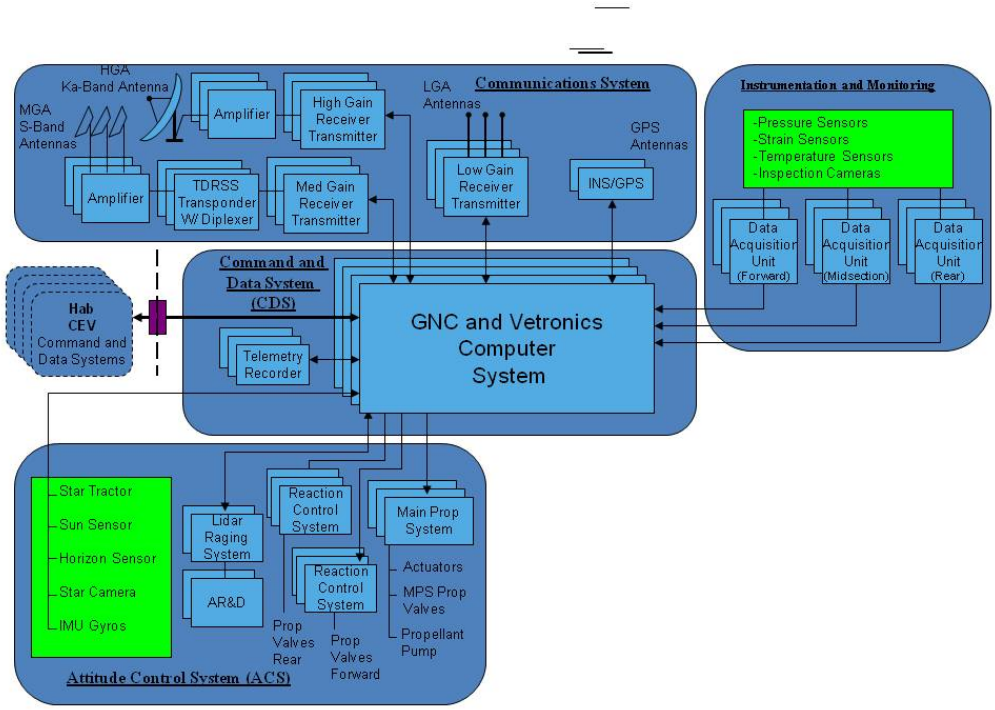

Figure 5.21 Avionics Schematic

5.7.1 Ground Rules and Assumptions

1) All mission critical components are 2-fault tolerant as consistent with a manned mission.
2) Communication with Earth will employ the Deep Space Network (DSN) and will be assumed to be inter-planetary in range.

5.7.2 Driving Requirements

1) 25Mbps Data rate (Max) – multi-channel voice and video
2) Complete location and Spacecraft Health telemetry.
3) Attitude Determination within 10 ArcSec
4) 35 Year Lifetime (Max)

5.7.3 Methodology

The avionics system was taken in its entirety from the Constellation Mars DRA-5 Design Reference Architecture in order to be comparable with other Mars studies. It should be noted that both mass and power requirements for this avionics architecture are comparable to that of the HOPE MTF study as well.

5.7.4 Mass Breakdown

The Avionics Mass Breakdown is shown in Table 5.14 below.

Table 5.14 Avionics Mass Breakdown

Subsystem	Mass (kg)
Attitude Control System	456
Command and Data System	210
Instrumentation and Monitoring	141
Communications System	850
Totals	1657

5.8 Vehicle Mass Breakdown

The Vehicle Mass Breakdown is shown in Table 5.15.

Table 5.15 Vehicle High Level Mass Breakdown

Subsystem	Mass (kg)
Payload	150,000
Structures	54,600
Main Propulsion	95,138
Reaction Control System	586
Thermal Management	77,164
Power	16,480
Avionics	389
Total Dry Mass	394357
30% Mass Growth Allowance	73,307
Total Mass (Best Estimate)	467,664

6 FUTURE WORK

The technology development required for this propulsion system is achievable on a reasonable timescale given sufficient resources. The first stage of a development program would involve sub-scale experiments to establish the foundational aspects of the system, such as Z-Pinch formation utilizing annular nozzles. Furthermore, the experiments would yield quantitative information enabling more sophisticated configurations for test and evaluation. The equipment needed for a suitable test facility is identified below, along with a general outline of the experimental program and some objectives identified in this study.

6.1 Z-Pinch Test Facility

DM2 stands for Decade Module 2, a ~500 kJ pulsed power facility. The DM2 was the last prototype serving as a test bed for the design and construction of the much larger Decade Machine, which was built and utilized at Arnold Air Force Base in Tennessee for Nuclear Weapons Effects (NWE) testing. DM2 was built by Physics International around 1995; it has had an active and important role in the development of advanced Plasma Radiation Sources (PRS) for the Defense Threat Reduction Agency's (DTRA) cold X-ray source development program.

DM2 is one of the latest inductive energy store, pulse power machines and is an excellent research platform for a university pulsed power or plasma physics research branch. Despite over 10 years of use, the unit is in good working order and has had a reliable operating history.
UAH has been in touch with current custodians of the DM2 machine and related equipment. This includes Anil Verma (Deputy and Program Manager in DTRA-RD-CXTN) and John Goyer of L3 Communications, who have notified the university that the facility is available for transfer, pending several steps in an approval process for transfer of government equipment. The UAH office of research has expressed interest in

Figure 6.1: Aerophysics Facility at Redstone

acquiring DM2. UAH has a secure facility in which to place DM2: the Aerophysics Facility located on Redstone Arsenal (see Figure 6.1). The space available in the building is shown in Figure 6.2. Jason Cassibry, Assistant Professor in the Department of Mechanical and Aerospace Engineering, is leading the coordination effort in the transfer and is currently exploring a sustainable business model for the long-term use of DM2. Dr. Bill Seidler, Senior Technical Fellow at Boeing, was actively involved in the DECADE program and is facilitating the communication between UAH and L3; he is also providing invaluable mentoring in DM2 utilization.

Experiments carried out on wire array Z-Pinch machines use multiple diagnostic methods to observe the behavior of the implosion process from initiation to stagnation. Any experiments carried out for this Z-Pinch propulsion concept will also accommodate the same diagnostic methods. A list of possible diagnostics useful for such an experiment would include the following:

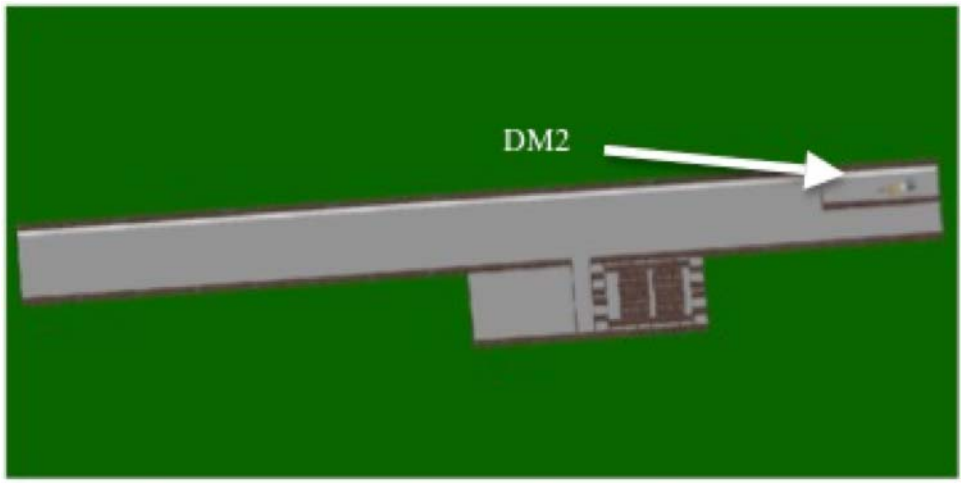

Figure 6.2: Aerophysics Facility Floor Layout

- X-ray diodes (XRD)
- Tantalum Calorimeters
- Zipper Array
- CCD-based extreme ultraviolet (XUV) transmission grating spectrography
- Laser shearing interferometer (LSI)
- Planar laser induced fluorescence (PLIF)
- Magnetic probes: B-dots, flux loops, rogowski coils, pearson probes, etc.
- Langmuir probes
- Mach-Zehnder interferometer (multiple chords).

This list only touches the surface of the multiple methods used in modern pulsed power experiments and therefore is not exhaustive. The main purpose is to illustrate the multitude of techniques available to acquire quantitative information about the plasma under study.

6.2 Development Plan

The most important questions have already been discussed by the team and deserve more scrutiny to determine what remains to be answered. The main concern currently is the operation of the thruster concept and whether it will work. There are multiple problems that must be solved, so the key objectives have been broken down as follows:

1. How will the Z-Pinch work in this configuration, and what is its functionality in relation to the rest of the system?
    a. This will involve sizing the Z-Pinch. As of now, the state-of-the-art Z-Pinch size is only a few centimeters, although there exist experiments capable of achieving Z-Pinch plasmas up to one meter in length.
    b. It also involves the scaling of physical laws via our experimental observations; i.e. compression, neutron flux, power output, etc.
2. Can the liner be made to work in the desired fashion? The obstacles associated with this question are legion:
    a. How will the lithium be handled?
    b. How will it be injected into the system and at what state (solid, liquid, gas, plasma)?
    c. Before attempting to use lithium, should a safer metal, such as gallium, be considered or tested?
    d. What materials will be needed in the feed system?
    e. How will the lithium be stored?
3. If the liquid liner concept is shown to function adequately, how can a magnetic nozzle be designed and constructed to direct the exhaust elements?
    a. What materials should be used?
    b. How might an MHD generator be incorporated for partial recharge of the power systems?
    c. How will the flow be redirected?
    d. How can important parameters such as specific impulse and thrust be measured or inferred?

Other questions that need to be answered include the following:

1. How can the system gain be measured or inferred using DM2?
2. What are the different scaling relationships that can be utilized to direct future experiments?
3. What experiments can be performed to determine optimum fuel mixing ratios, and how might they be incorporated into the overall process?
4. What methods can be used to mitigate radiation from the machine?

The obstacles to answering these questions will require significant time and effort; however, they can be answered in conjunction with the key objectives.

In addition to the general objectives listed above, a loose schedule of how the experimental program might be built up from DM2 to a break-even facility is outlined in Table 6.1.

Table 6.1 Schedule

Experiment Stage	# Years
DM2	3
Single Decade Quad	2
4 Decade Quads	2
8 Decade Quads (1 full ring)	2
2 Full Rings (Break-even)	2
	Total: 11 years

Although 11 years is an optimistic timeline, it can be achieved, given the right technology and resources. Development of each experimental stage, i.e. the design and construction of additional Decade modules, needs to occur in parallel with experiments/tests.

In general, a phased approach to this could be the following:

Phase 1. Develop the Z-Pinch and Dense Plasma Focus concepts
- Identify critical elements to test experimentally
- Design experimental apparatus for testing
- Evaluate the mission effectiveness of the proposed propulsion concepts

Phase 2. Experiment set-up and diagnostic development
- Clear out laboratory space(s)
- Finalize experimental layout and install supporting infrastructure
- Transport equipment and set up testing facility with new control systems
- Develop diagnostics and test methods for T&E activities

Phase 3. First sub-scale tests
- Perform initial Z-Pinch formation studies
- Install first diagnostic package and perform initial tests and calibration
- Initiate development of systems for fuel handling and injection
- Develop nozzle designs

Phase 4. Larger scale testing for thruster designs
- Perform design and testing for thruster configuration(s)
- Begin experimenting with fuel mixing properties
- Begin development of diagnostic methods for full-scale thermonuclear testing

6.3 Future Magnetic Nozzle Analysis Work

The effort during this study has focused largely on modifying the theory of magnetic nozzle operation and then implementing it in a piece of software. So far there has been little opportunity to thoroughly explore the available trade space. As a result the design offered here is not an optimum one. Among the various issues which would benefit from further study are the following:

- Variation in the number and location of the nozzle rings
- Variation in the minor radius of each nozzle ring
    - In this study they were all taken to have the same minor radius. In practice, a gradual variation would probably be optimum, with the smaller diameter rings having larger minor radii than the larger ones.
- Variation in the position of the paraboloid focus
    - In this study, the focus is always 2 meters from the nozzle apex.
- Variation in current amplification factor
    - The currently assumed value of 25 was selected because it gave a successful performance solution; this factor needs to be varied, along with the seed-field flux, to seek an optimum solution.

7 FUTURE WORK

A vehicle of this magnitude represents a substantial investment. In order to justify its development, it must be reusable and suitable for a wide variety of missions. It is possible that with some refurbishment between missions, the vehicle could have a very long service life (much like Naval vessels). New (full) propellant tanks could replace the spent ones, and components that incur significant wear and/or damage (Z-Pinch electrical leads, Lithium nozzles, Z-Pinch diodes and switches, SP-100 Reactor, etc) could be replaced robotically while the vehicle is at dock at L1.

As the vehicle nears the end of its service life, it could be sent on a very long range one-way mission to an inter-stellar destination.

References

Carlson, D. (1985). SP-1OO Low Mass Shield Design. *2nd SP-1OO Program Integration Meeting.*

Derzon, M. S., Rochau, G. A., DeGroot, J., Olson, C., Peterson, P., Peterson, R. R., et al. (2000). *An Inertial-Fusion Z-Pinch Power Plant Concept.* Albuquerque, NM: Sandia National Laboratories.

Drake, B. (2009). *Human Exploration of Mars Design Reference Architecture 5.0.* National Aeronautics and Space Administration, NASA Headquarters.

Emrich, W. (2010). Mathematica freeware shielding tool. Huntsville, AL: National Aeronautics and Space Administration, Marshall Space Flight Center.

Hsu, S., Tang, X., Wang, Y. and Tynan, G. (2009). *Synergistic Effects of Radiation Damage and Plasma-Material Interactions.*

Humble, R., Henry, G., Larson, W. (1995) *Space Propulsion Analysis and Design.* McGraw-Hill.

Joy, J. (2006). Mixed Li-B Materials. *Adv in Scie & Tech,* Vol 45.

Knecht, S. D., Mead, F. B., Thomas, R. E., Miley, G. H., & Froning, D. (2006). Propulsion and Power Generation Capabilities of a Dense Plasma Focus (DPF) Fusion System for Future Military Aerospace Vehicles. *AIP Conference Proceedings. 813*, p. n/a. Albuquerque, NM: American Institute of Physics.

Lindemuth, I., and Siemon, R. (2009). The fundamental parameter space of controlled thermonuclear fusion. *American Journal of Physics* 77, no. 5: 407-416.

Mather, J. (1966). An Intense Source of Neutrons From The Dense Plasma Focus. *Fast Pulsed Neutron Sources* (pp. 623-632). Los Alamos, NM: Los Alamos Scientific Laboratory.

Moreno, C., Bruzzone, H., Martinez, J., & Clausse, A. (2000). Conceptual Engineering of Plasma-Focus Thermonuclear Pulsors. *IEEE Transactions on Plasma Science , 28* (5).

Olson, C. e. (2005). Development Path for Z-Pinch IFE. *Fusion Science and Technology , 47*, 633-640.

Schulze, Norman R. 1991. *Fusion Energy for Space Missions in the 21st Century*. NASA Technical Memorandum. NASA Office of Safety and Mission Quality, August.

Shumlak, U., Lilly, R. C., Adams, C. S., Golingo, R. P., Jackson, S. L., Knecht, S. D., et al. (2006). Advanced Space Propulsion Based on the Flow-Stabilized Z-Pinch Fusion

Concept. *42nd AIAA/ASME/SAE/ASEE Joint Propulsion Conference* (pp. 1-14). Sacramento, CA: AIAA.

Slutz, S. A., Olson, C. L., Rochau, G. E., Derzon, M. S., Peterson, P. F., DeGroot, J. S., et al. (2000). *Z-Pinch Driven Fusion Energy.* Albuquerque, NM: Sandia National Laboratories.

Tonks, L. *Transactions of the Electrochemical Society , 72* (37), 167.

Turchi, P. J., Roderick, N. F., Degnan, J. H., Frese, M. H., and Amdahl, D. (2008, July 13-18). Plasma Guns for Controlled Fusion at Megagauss Energy-Densities. *12th International Conference on Megagauss Magnetic Field Generation* . Novosibirisk, Russia.

Turchi, P. J., Roderick, N. F., Degnan, J. H., Frese, M. H., & Amdahl, D. (2009). *Plasma Guns for Controlled Fusion at Megagauss Energy-Densities.* Los Alamos, NM: Los Alamos National Laboratory.

Velikovich, A. L., R. W. Clark, J. Davis, Y. K. Chong, C. Deeney, C. A. Coverdale, C. L. Ruiz, et al. 2007. Z-Pinch plasma neutron sources. *Physics of Plasmas* 14, no. 2: 022701. doi:10.1063/1.2435322.

Williams, C. (2004). *Recommended Design Practices for Conceptual Nuclear Fusion Space Propulsion Systems.* Special Project Report. Reston, VA: American Institute of Aeronautics and Astronautics.

APPENDIX A: PLASMA EXPANSION AND MAGNETIC FLUX COMPRESSION

This appendix consists of an entirely *qualitative* description of the phenomena of magnetic flux compression, which appears to take place within the magnetic nozzle during plasma expansion.

Consider a cross-section through the nozzle that coincides with one of the thrust rings (Figure A.1). If one considers the situation before fusion takes place, the region is occupied by the seed magnetic field, which is represented by the field lines shown passing down *into* the plane of the figure. The thrust ring is shown in green.

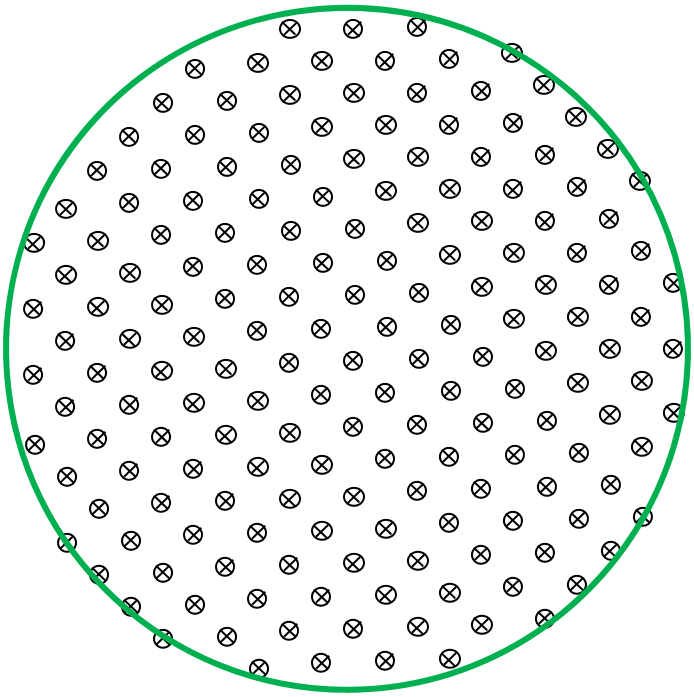

Figure A.1 Ring and Seed Field

The total magnetic flux contained within the ring is denoted by Φ, where

$$\Phi = \int \underline{B} \cdot \underline{dA} \qquad \text{A-1}$$

$\underline{B}$ denotes the magnetic field, $\underline{dA}$ is an element of cross-sectional area and the integral is carried out over the entire cross-section area enclosed by the ring.

Assuming a uniform seed field ($\underline{B}_{seed}$) the flux can be approximated as

$$\Phi \approx \pi R_{ring}^2 B_{seed} \qquad \text{A-2}$$

As the highly-conductive fusion plasma expands it crosses the seed field lines and as it does so it experiences a $\underline{v} \times \underline{B}$ electromotive force, which induces an electrical current. The current – which flows in the outer regions of the plasma – travels in a direction that can be determined from the 'right-hand' generator effect. This induced current flows in such a way as to generate a magnetic field which exactly counteracts the seed field *within* the plasma, but which reinforces it *outside* the plasma. This is illustrated below (Figure A.2); where the plasma, its induced current and the consequent magnetic field lines are all shown in red (red arrows indicate direction of current).

Color-coding:

- *The original seed-field lines are shown on black* ⊗
- *The field lines due to the plasma current are shown in red* ⊙ & ⊗
- *The field lines due to the thrust ring current are shown in green* ⊙ & ⊗

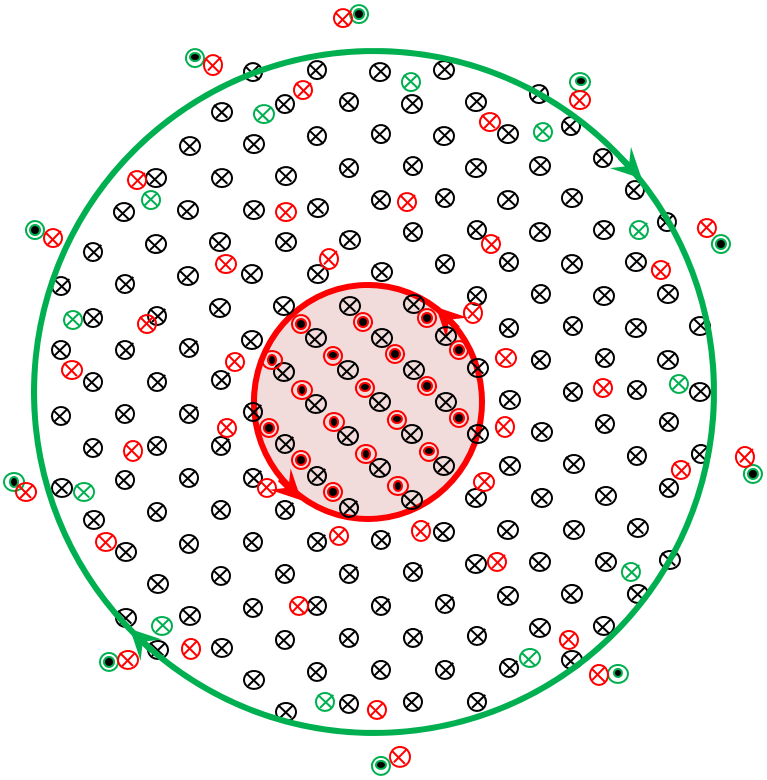

Figure A.2 Expanding Plasma with Induced Current and Magnetic Field

Note that, *within* the plasma, every seed-field line passing down *into* the plane of the diagram is matched by one which passes up *out of* the plane of the diagram. These new lines are produced by the induced current flowing in the outer regions of the plasma.

Also note that the new B-field (in red) caused by the plasma current also extends out to the thrust ring, where it induces (through $\underline{v} \times \underline{B}$) a counter-current in the ring (direction shown with a green arrow). This counter-current itself generates a B-field (the field-lines for which are shown in green).

When the above diagram is 'cleaned up' – by cancelling all the various counteracting field lines – the following picture emerges (Figure A.3).

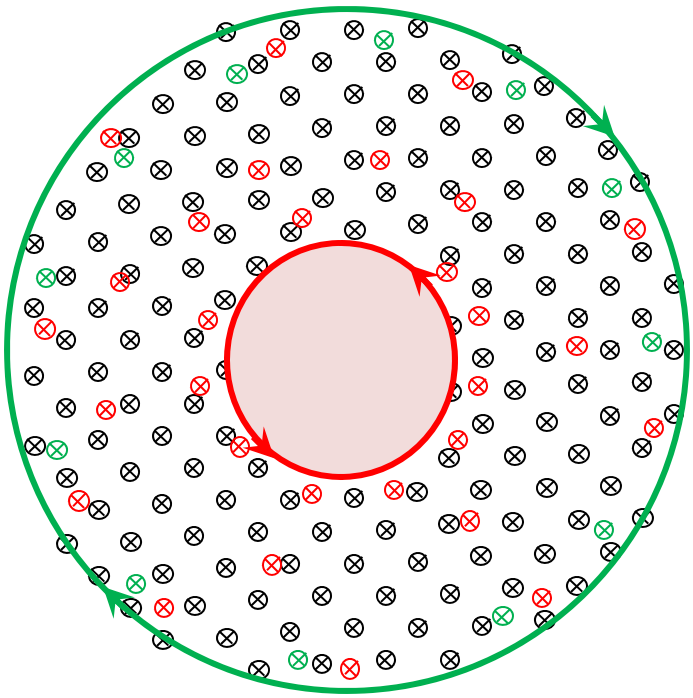

Figure A.3 Expanding Plasma with Induced Current and Net Magnetic Field

The net effect – after all the cancellations – is that the original seed field flux appears to have been compressed into the annular region between the outer edge of the plasma and the ring.

This process continues as the plasma expands further. The situation at a later time is shown below (Figure A.4).

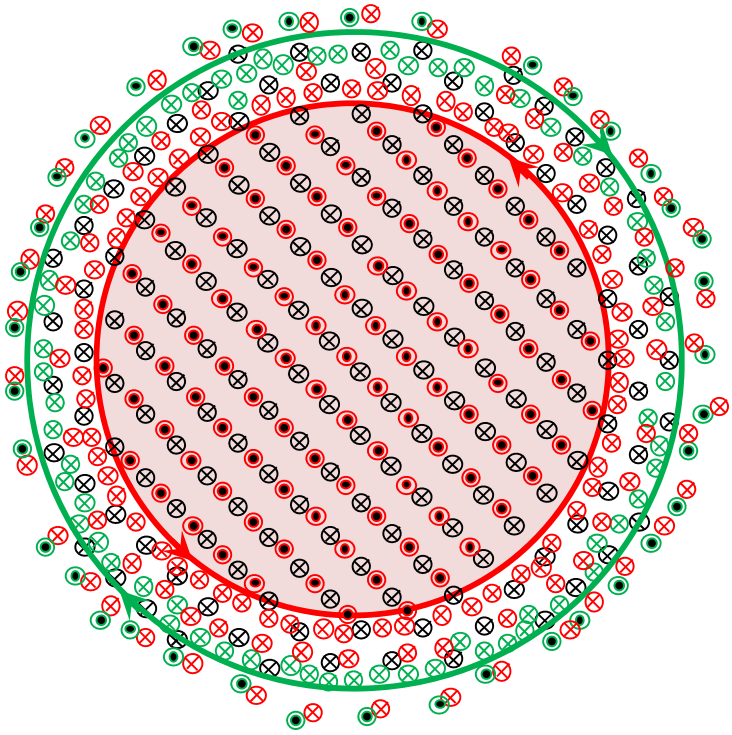

Figure A.4 Expanding Plasma with Induced Current and Magnetic Field

Once again, after cancelling the counteracting field lines the net effect is one of apparent flux-compression, as shown below (Figure A.5).

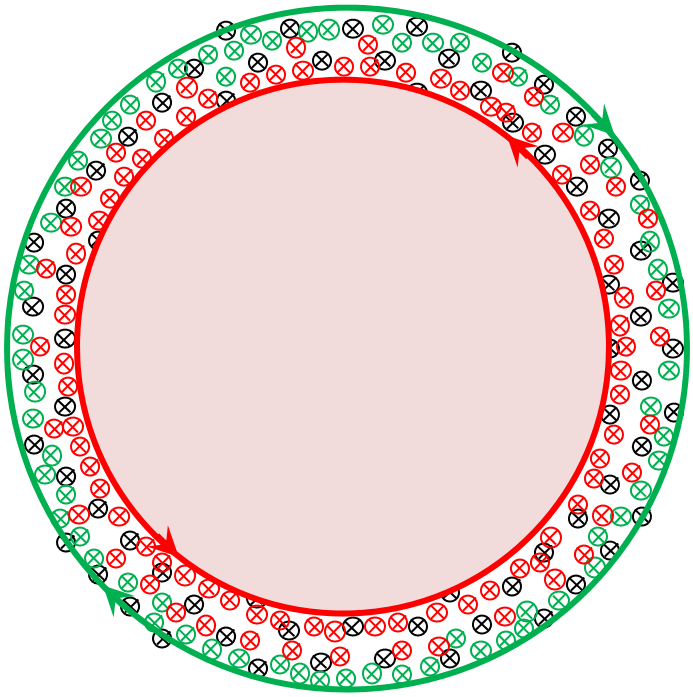

Figure A.5 Expanding Plasma with Induced Current and Net Magnetic Field

Maintaining the assumption of a uniform magnetic field (B) in the annulus, the flux can be approximated as

$$\Phi \approx \pi\left(R_{ring}^2 - R_{plasma}^2\right)B \qquad \text{A-3}$$

where R_{plasma} is the radius of the plasma cloud.

Equating this with the flux given in equation (A-2) yields

$$B \approx B_{seed}\frac{R_{ring}^2}{\left(R_{ring}^2 - R_{plasma}^2\right)} \qquad \text{A-4}$$

As $R_{plasma} \to R_{ring}$, clearly B becomes very much greater than B_{seed}.

Under the flux-compression description of events the expanding plasma shell motion is retarded by magnetic pressure in the surrounding annulus. Under this alternate picture, consider an arbitrary point P in Figure A.6.

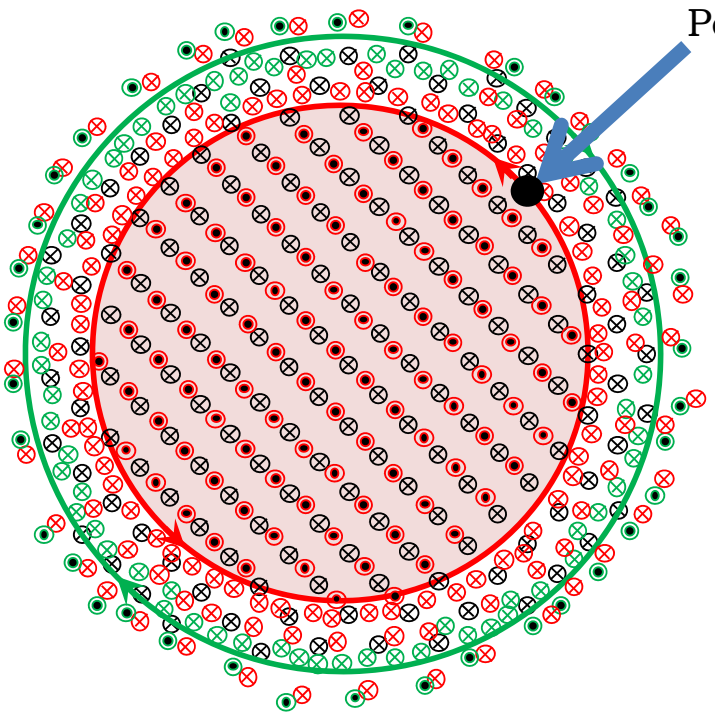

Figure A.6 Arbitrary Point P on Plasma Surface

At point P the radially-outward motion of the conductor across the seed-field lines induces an azimuthal $\underline{v} \times \underline{B}$ and hence a current – according to the 'right-hand' generator rule as illustrated below (Figure A.7).

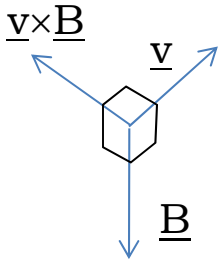

Figure A.7 Electromotive Force at Point P

The azimuthal current interacts with the seed-field to produce a $\underline{j} \times \underline{B}$ force (according to 'left-hand' motor rule) which acts radially inwards and retards motion outwards. This is illustrated below (Figure A.8).

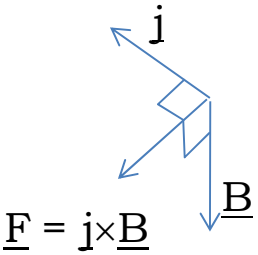

Figure A.8 Retarding Force at Point P

It is this retarding force that slows the plasma expansion.

APPENDIX B: MAGNETIC NOZZLE THEORY

This treatment is a revised and expanded version of that presented in the final report for the RASC-HOPE study (Conceptual Design of In-Space Vehicles for Human Exploration of the Outer Planets: NASA/TP—2003–212691) and is based on work originally done by Dr. Francis Thio.

The model addresses the situation late during expansion of the plasma cloud, when interaction with the nozzle magnetic field has already caused its leading surface to assume the form of a paraboloid (i.e. a parabola of revolution). Although this approach neglects the initial expansion (which will probably be spherical) it can be justified by the fact that the important period of magnetic nozzle operation will be the later part. This is because it is only during this later stage that the flux compression and hence the magnetic pressure become significant.

Consider a time late in the plasma expansion, where the magnetic flux is all contained in the thin 'annular' gap between two parabolas (which are assumed to have their foci at the same point) as shown below (Figure B.1). The outer parabola marks the position of the nozzle rings and the inner one represents the expanding plasma shell.

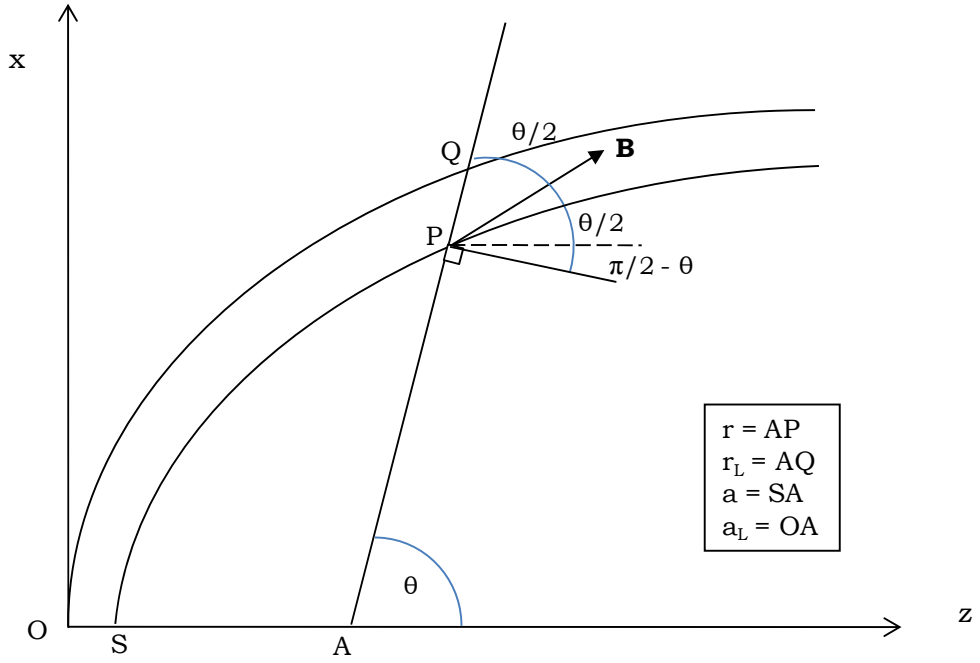

Figure B.1 Magnetic Flux Contained in Gap Between Two Parabolas

The total flux (Φ) is effectively conserved during plasma expansion and so the magnetic field strength (**B**) can be determined from

$$\Phi = A_{con}\left[B\cos\left(\frac{\pi}{2}-\frac{\theta}{2}\right)\right] = BA_{con}\sin\left(\frac{\theta}{2}\right) \qquad \text{B-1}$$

where A_{con} is the total area of the conical annulus, which is formed by rotating the line PQ through one complete rotation about the nozzle axis (i.e. the z-axis).

This area is illustrated below in Figure B.2 (with a diagram only showing the cone).

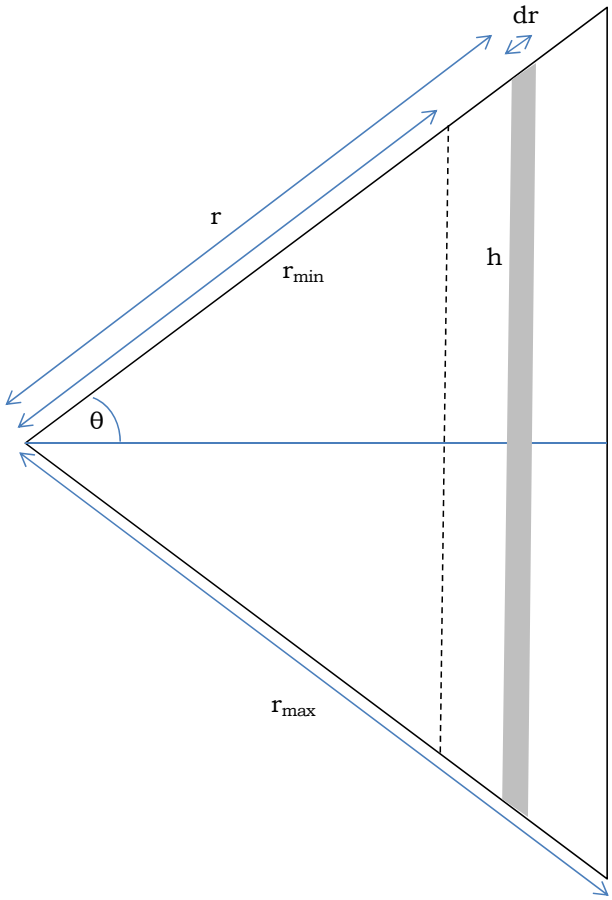

Figure B.2 Area of the Conical Annulus

From this diagram it can be seen that the elemental conical annulus (shaded in the diagram) has area given by

$$dA_{con} = 2\pi h dr \qquad \text{B-2}$$

It is also know that

$$h = r\sin\theta \qquad \text{B-3}$$

and so

$$dA_{con} = 2\pi r\sin\theta dr \qquad \text{B-4}$$

This can be integrated to give

$$A_{con} = \pi\sin\theta\left(r_{\max}^2 - r_{\min}^2\right) \qquad \text{B-5}$$

Returning to Figure B-1, the equations for the two parabolas (the inner and outer ones) can be written in circular polar coordinates as

$$r = \frac{2a}{(1-\cos\theta)} \qquad \text{B-6}$$

and

$$r_L = \frac{2a_L}{(1-\cos\theta)} \qquad \text{B-7}$$

Combining (B-5), (B-6) and (B-7) it can be shown that

$$A_{con} = 4\pi \sin\theta \frac{\left(a_L^2 - a^2\right)}{\left(1-\cos\theta\right)^2} \qquad \text{B-8}$$

Using this expression with (B-1) the following expression for the magnetic field can be derived

$$B = \frac{\Phi}{A_{con} \sin\left(\frac{\theta}{2}\right)} = \frac{\Phi\left(1-\cos\theta\right)^2}{4\pi \sin\theta\left(a_L^2 - a^2\right)\sin\left(\frac{\theta}{2}\right)} \qquad \text{B-9}$$

The half angle formula for tangent can be written as

$$\tan\left(\frac{\theta}{2}\right) = \frac{1-\cos\theta}{\sin\theta} \qquad \text{B-10}$$

And thus

$$\sin\theta \tan^2\left(\frac{\theta}{2}\right) = \frac{\left(1-\cos\theta\right)^2}{\sin\theta} \qquad \text{B-11}$$

Combining (9) and (11) gives

$$B = \frac{\Phi \sin\theta \tan^2\left(\frac{\theta}{2}\right)}{4\pi\left(a_L^2 - a^2\right)\sin\left(\frac{\theta}{2}\right)} = \frac{\Phi 2\sin\left(\frac{\theta}{2}\right)\cos\left(\frac{\theta}{2}\right)\tan^2\left(\frac{\theta}{2}\right)}{4\pi\left(a_L^2 - a^2\right)\sin\left(\frac{\theta}{2}\right)} \qquad \text{B-12}$$

which becomes

$$B = \frac{\Phi \sin^2\left(\frac{\theta}{2}\right)}{2\pi\left(a_L^2 - a^2\right)\cos\left(\frac{\theta}{2}\right)} \qquad \text{B-13}$$

The magnetic pressure (p_B) is given by

$$p_B = \frac{B^2}{\mu_0} \qquad \text{B-14}$$

where μ_0 is the magnetic permeability of free space.

To determine the force acting on an element of plasma, the element must first be defined. This is done in Figure B.3.

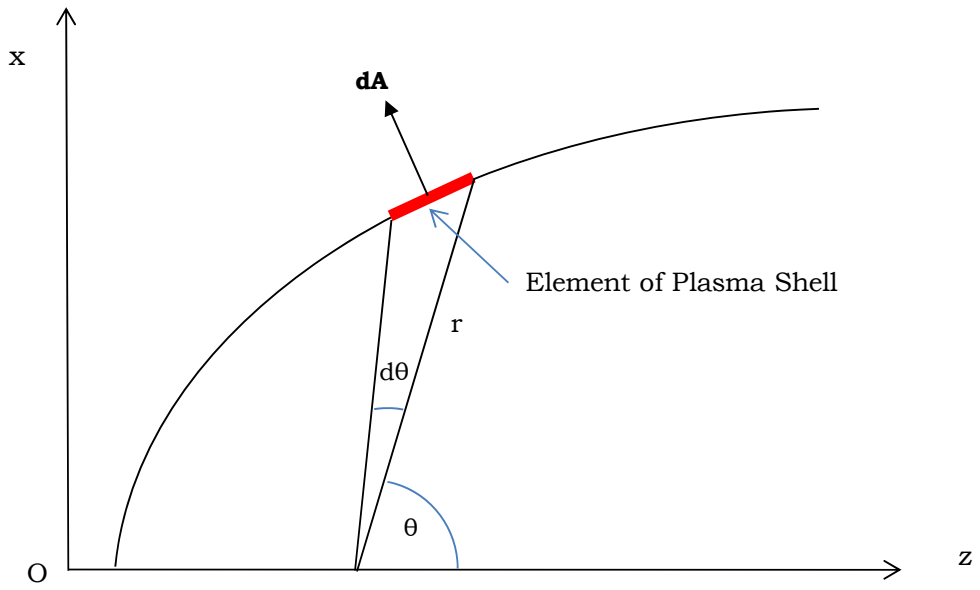

Figure B.3 Determining the Force Acting on an Element of Plasma

The vector element of area (dA) can be written as

$$\underline{dA} = dA_\theta \underline{e_\theta} + dA_r \underline{e_r} \qquad \text{B-15}$$

where $\underline{e_\theta}$ and $\underline{e_r}$ are the local unit vectors in the θ and r directions (in a spherical polar coordinate system based at the nozzle focus).

The element is shown in greater detail below in Figure B.4.

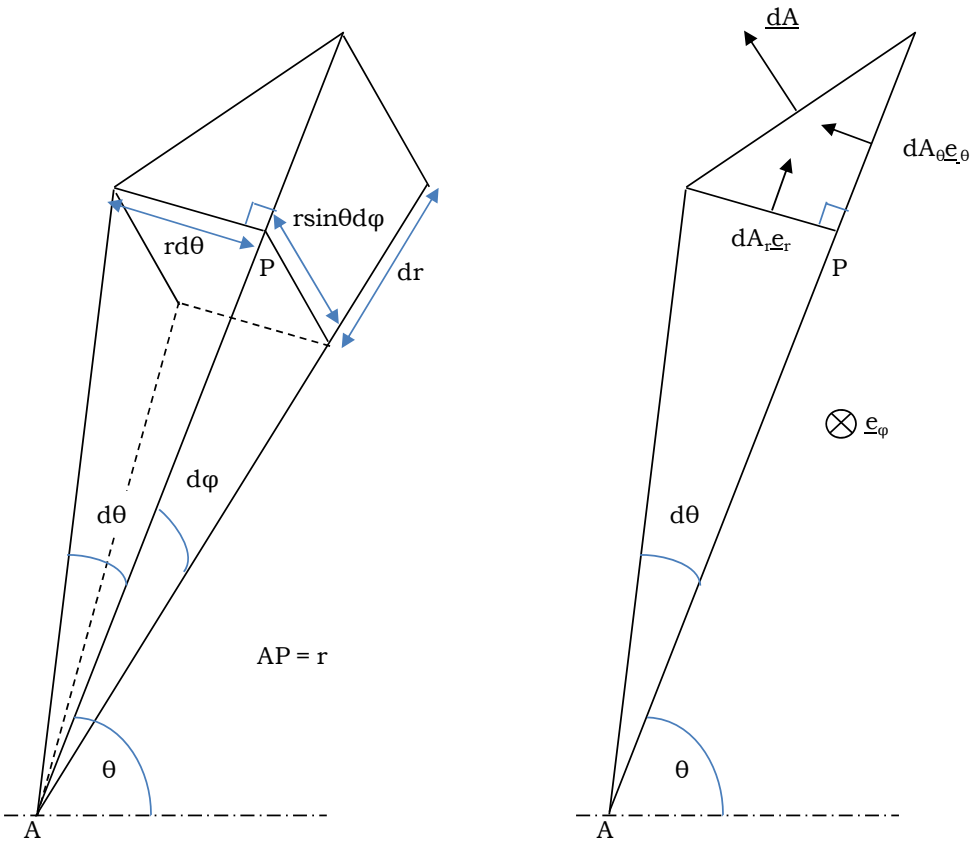

Figure B.4 Vector Element

From Figure B.4 it can be seen that

$$dA_r = r^2 \sin\theta d\theta d\phi \qquad \text{B-16}$$

and also

$$dA_\theta = r\sin\theta(-dr)d\phi \qquad \text{B-17}$$

Note that the dr term has a minus sign because r decreases as θ increases (this can be seen from Figure B-4 where – because of the shape of the surface element dA – the value of r at angle θ + dθ is less than it was at angle θ).

Hence

$$\underline{dA} = -r\sin\theta dr d\phi \underline{e_\theta} + r^2 \sin\theta d\theta d\phi \underline{e_r} \qquad \text{B-18}$$

This can be rewritten as

$$\underline{dA} = r\sin\theta d\phi\left(-dr\underline{e_\theta} + rd\theta\underline{e_r}\right) \qquad \text{B-19}$$

and also

$$\underline{dA} = r^2 \sin\theta d\phi d\theta\left(-\frac{1}{r}\frac{dr}{d\theta}\underline{e_\theta} + \underline{e_r}\right) \qquad \text{B-20}$$

From (B-6), dr/dθ can be derived as follows

$$\frac{dr}{d\theta} = \frac{-2a\sin\theta}{(1-\cos\theta)^2} = -\frac{r\sin\theta}{(1-\cos\theta)} \qquad \text{B-21}$$

and thus

$$\underline{dA} = r^2 \sin\theta d\phi d\theta \left(\frac{\sin\theta}{(1-\cos\theta)} \underline{e_\theta} + \underline{e_r} \right) \qquad \text{B-22}$$

Which can be rewritten as

$$\underline{dA} = r^2 \sin\theta d\phi d\theta \left(\cot\left(\frac{\theta}{2}\right) \underline{e_\theta} + \underline{e_r} \right) \qquad \text{B-23}$$

Now the solid angle (dΩ) subtended at the focus (point A in Figure B-4) by this element of plasma is given by

$$d\Omega = \sin\theta d\theta d\phi \qquad \text{B-24}$$

Combining (B-23) and (B-24) gives

$$\underline{dA} = r^2 d\Omega \left(\cot\left(\frac{\theta}{2}\right) \underline{e_\theta} + \underline{e_r} \right) \qquad \text{B-25}$$

The pressure force acting on this element of plasma is given by

$$\underline{dF} = -p_B \underline{dA} \qquad \text{B-26}$$

where the minus sign is to account for the fact that the magnetic pressure acts *inwards* on the plasma shell (whereas the area element vector points *outwards*).

Thus

$$\underline{dF} = -p_B r^2 d\Omega \left(\cot\left(\frac{\theta}{2}\right) \underline{e_\theta} + \underline{e_r} \right) \qquad \text{B-27}$$

To first approximation, it is assumed that elements of the plasma shell that subtend the same solid angle at the focus all contain the same mass of plasma.

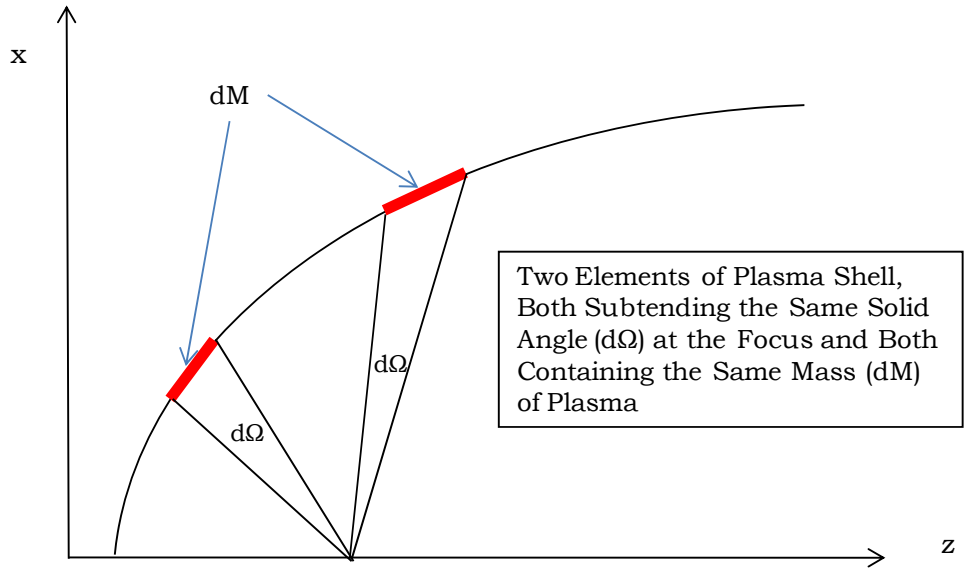

Figure B.5 Two Elements of Plasma Shell

If the total mass of plasma in the shell is denoted by M, then the amount (dM) in a portion of the shell that subtends solid angle dΩ at the focus is given by

$$dM = \frac{d\Omega}{4\pi} M \qquad \text{B-28}$$

And thus (B-27) becomes

$$\underline{dF} = -4\pi p_B r^2 \frac{dM}{M}\left(\cot\left(\frac{\theta}{2}\right)\underline{e_\theta} + \underline{e_r}\right) \qquad \text{B-29}$$

Now the equation of motion for the plasma element dM can be written as

$$\underline{dF} = dM \frac{d\underline{v}}{dt} \qquad \text{B-30}$$

From (B-29) and (B-30) the following expression for the plasma velocity during the expansion phase can thus be derived

$$\frac{d\underline{v}}{dt} = -\frac{4\pi p_B r^2}{M}\left(\cot\left(\frac{\theta}{2}\right)\underline{e_\theta} + \underline{e_r}\right) \qquad \text{B-31}$$

Note that *dv/dt* is negative, as expected (because for θ in the range 0 to 2π, cot(θ/2) is always positive). This equation can be used to numerically to model plasma shell expansion (provided p_B is recalculated at each time step). It can also be used, with reduced fidelity, to model the initial phases of the plasma 'rebound' – when it begins to move away from the nozzle rings.

Equation (B-27) gives the force acting on an element of plasma. The corresponding reactive force – acting on the thrust rings – due to the same element of plasma is given by

$$\underline{dF} = p_B r^2 d\Omega\left(\cot\left(\frac{\theta}{2}\right)\underline{e_\theta} + \underline{e_r}\right) = p_B r^2 \sin\theta d\theta d\phi\left(\cot\left(\frac{\theta}{2}\right)\underline{e_\theta} + \underline{e_r}\right) \qquad \text{B-32}$$

This can be combined with (B-31) to give

$$\underline{dF} = -\frac{M}{4\pi}\frac{dv}{dt}\sin\theta d\theta d\phi \qquad \text{B-33}$$

Now consider the thrust force acting on the thrust rings due to the element of plasma shell with polar (θ) and azimuthal (φ) angles in the following ranges

$$\theta = \theta_i \to \theta_{i+1}$$
$$\textit{and} \qquad \text{B-34}$$
$$\phi = \phi_j \to \phi_{j+1}$$

Clearly the thrust force due to this element of plasma, denoted by $\underline{F}\left(\theta_i \to \theta_{i+1}, \phi_j \to \phi_{j+1}\right)$ is given by

$$\underline{F}\left(\theta_i \to \theta_{i+1}, \phi_j \to \phi_{j+1}\right) = -\int_{\phi_j}^{\phi_{j+1}} d\phi \int_{\theta_i}^{\theta_{i+1}} \sin\theta d\theta \frac{M}{4\pi}\frac{d\underline{v}}{dt} \qquad \text{B-35}$$

This is the force acting on the portion of the rings in the angular interval (B-34), due to the magnetic field 'compression'.

As the situation is symmetric about the nozzle axis, this can be written as

$$\underline{F}\left(\theta_i \to \theta_{i+1}, \phi_j \to \phi_{j+1}\right) = -\left(\phi_{j+1} - \phi_j\right)\int_{\theta_i}^{\theta_{i+1}} \sin\theta d\theta \frac{M}{4\pi}\frac{d\underline{v}}{dt} \qquad \text{B-36}$$

This expression can be used to derive the thrust force experienced by each individual coil. To do this, assume that each coil experiences the reaction force due to that portion of the plasma that has a polar angle closer to it than to any other coil. If coils i –1, i, and i +1 have polar angles of θ_{i-1}, θ_i, and θ_{i+1}, respectively, then the portion of plasma with polar angle between $(\theta_{i-1} + \theta_i)/2$ and $(\theta_{i+1} + \theta_i)/2$ is associated with coil i. This is illustrated in Figure B-6.

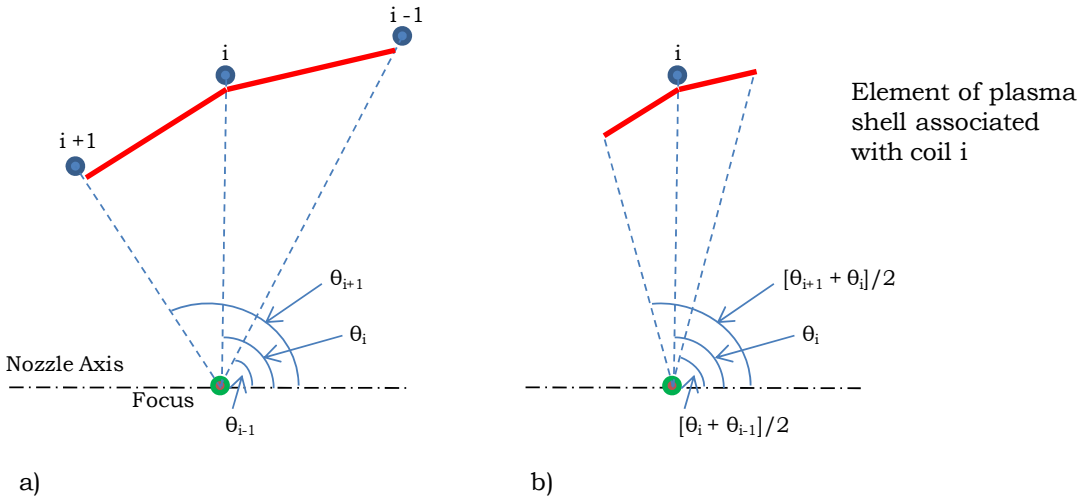

Figure B.6 Coil to Plasma Associations

Under these assumptions (and assuming that the force is not too strong a function of the polar angle θ) the thrust force experienced by coil i ($\underline{F}_i$) is given by

$$\underline{F}_i \approx -2\pi\frac{M}{4\pi}\frac{d\underline{v}}{dt}\bigg|_{\theta_i}\int_{\frac{(\theta_{i-1}+\theta_i)}{2}}^{\frac{(\theta_{i+1}+\theta_i)}{2}} \sin\theta d\theta \qquad \text{B-37}$$

Where $\left.\frac{d\underline{v}}{dt}\right|_{\theta_i}$ denotes the value of $\frac{d\underline{v}}{dt}$ at polar angle θ_i.

This equation becomes

$$\underline{F}_i \approx \frac{M}{2}\frac{d\underline{v}}{dt}\bigg|_{\theta_i}\left[\cos\left(\frac{\theta_{i+1}+\theta_i}{2}\right) - \cos\left(\frac{\theta_{i-1}+\theta_i}{2}\right)\right] \qquad \text{B-38}$$

Speaking now in a cylindrical-polar sense, the radial and axial components of this force are as shown below in Figure B.7.

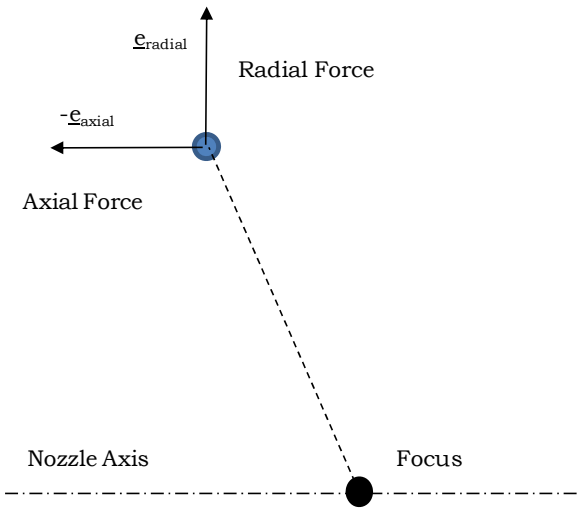

Figure B.7 Radial and Axial Components

The radial and axial unit vectors are given by

$$\underline{e}_{radial} = \underline{e}_{\theta}\cos\theta + \underline{e}_{r}\sin\theta \qquad \text{B-39}$$

and

$$\underline{e}_{axial} = -\underline{e}_{\theta}\sin\theta + \underline{e}_{r}\cos\theta \qquad \text{B-40}$$

Starting with an initial 'parabolic shell' of plasma, expanding with a given speed, and a value for the total magnetic flux (Φ), the above analysis enables one to incrementally model the subsequent plasma expansion to the point where it is brought to rest by the increasingly compressed flux (and hence the increasingly strong magnetic field). The subsequent 'rebound's stage can also be modeled for a short period – whilst the plasma shell can still be treated as being composed of a number of annuli all having paraboloid form.

Next, a technique for modeling the maximum current flowing in the thrust coils – an important design parameter – is considered using an inductively-based analysis.

The equation for magnetic self-inductance of a simple current-carrying ring is

$$\Phi = LI \qquad \text{B-41}$$

where L denotes self-inductance and I current.

Consider a single thrust ring (ring j). When the seed field is present (before the fusion event takes place) the total flux contained within the ring is given by

$$\Phi_{j} = L_{j} I_{s,j} \qquad \text{B-42}$$

Where L_j denotes the self-inductance of ring j and $I_{s,j}$ denotes the initial current in ring j.

After the fusion event, when the plasma is at maximum expansion, the situation is akin to that shown below, where the skin current running around the plasma represents another current ring, which has its own self-inductance ($L_{p,j}$) as well as a mutual inductance (M_j) between itself and the thrust ring.

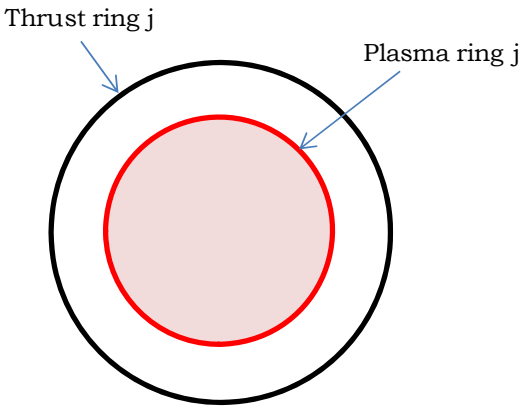

Figure B.8 Thrust and Plasma Rings

At this point, the flux through the thrust ring is given by

$$\Phi_j = L_j I_{c,j} + M_j I_{p,j} \qquad \text{B-43}$$

Where $I_{c,j}$ is the current now running through thrust ring j (the subscript 'c' denoting that the B-field is in its compressed state) and $I_{p,j}$ is the current running through plasma ring j. The following expression for the flux through the plasma ring is

$$\Phi_{pj} = L_{p,j} I_{p,j} + M_j I_{c,j} \qquad \text{B-44}$$

Where Φ_{pj} denotes the flux enclosed by plasma-current ring j.

However it is known that the net flux enclosed by the plasma ring current is zero (i.e. $\Phi_{pj} = 0$) and thus

$$M_j = -L_{p,j} \frac{I_{p,j}}{I_{c,j}} \qquad \text{B-45}$$

And thus (B-43) becomes

$$\Phi_j = L_j I_{c,j} - L_{p,j} \frac{I_{p,j}}{I_{c,j}} I_{p,j} = \left(L_j - L_{p,j} \left[\frac{I_{p,j}}{I_{c,j}} \right]^2 \right) I_{c,j} \qquad \text{B-46}$$

from which a new net induction for thrust ring j ($L_{c,j}$) can be defined, *which of course applies only at this specific point during plasma expansion and magnetic flux compression*

$$L_{c,j} = \left(L_j - L_{p,j} \left[\frac{I_{p,j}}{I_{c,j}} \right]^2 \right) \qquad \text{B-47}$$

Where it can now be written

$$L_{c,j} I_{c,j} = \Phi_j \qquad \text{B-48}$$

Now consider the total energy in coil j before compression begins (i.e. when only the seed field is present). This quantity is denotes by E_{js} and is given by

$$E_{js} = \frac{1}{2} L_j I_{s,j}^2 \qquad \text{B-49}$$

At maximum plasma expansion the energy is denoted by E_{jc} and is given by

$$E_{jc} = \frac{1}{2} L_{c,j} I_{c,j}^2 \qquad \text{B-50}$$

Define a current amplification factor (A_j) – between the seed field situation and the situation at maximum flux compression – as follows

$$A_j = \frac{I_{c,j}}{I_{s,j}} \qquad \text{B-51}$$

Using this expression, (B-48) can be written as

$$A_j L_{c,j} I_{s,j} = \Phi_j \qquad \text{B-52}$$

(B-50) can also be rewritten as

$$E_{jc} = \frac{1}{2} A_j^2 L_{c,j} I_{s,j}^2 \qquad \text{B-53}$$

Next, $L_{c,j}$ can be eliminated between (B-52) and (B-53) to give

$$E_{jc} = \frac{1}{2} A_j^2 \frac{\Phi_j}{A_j I_{s,j}} I_{s,j}^2 = \frac{1}{2} A_j \Phi_j I_{s,j} \qquad \text{B-54}$$

Finally, $I_{s,j}$ can be eliminated from (B-54) using (B-42) to give

$$E_{jc} = \frac{1}{2} A_j \Phi_j \frac{\Phi_j}{L_j} = \frac{1}{2} \frac{A_j \Phi_j^2}{L_j} \qquad \text{B-55}$$

(B-49) can be used to write an equivalent expression for the initial energy

$$E_{js} = \frac{1}{2} L_j I_{s,j}^2 = \frac{1}{2} \frac{\Phi_j^2}{L_j} \qquad \text{B-56}$$

From (B-55) and (B-56) it follows that

$$E_{jc} = A_j E_{js} \qquad \text{B-57}$$

The energy input to the magnetic field due to plasma expansion can be written as

$$\Delta E_j = E_{jc} - E_{js} = \left(A_j - 1\right) E_{js} \qquad \text{B-58}$$

Which can be rewritten, using (B-56) as

$$\Delta E_j = E_{jc} - E_{js} = \left(A_j - 1\right) \frac{1}{2} \frac{\Phi_j^2}{L_j} \qquad \text{B-59}$$

The simple initial self-inductance of the ring L_j is given by

$$L_j = \mu_0 R_j \left[\ln\left(\frac{4\pi R_j}{a_j} \right) - 2.45 \right] \qquad \text{B-60}$$

Where the various quantities are defined in Figure B.9.

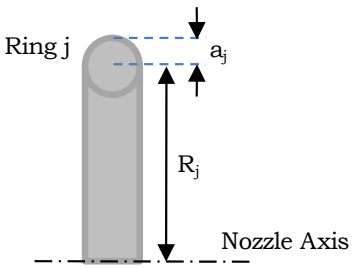

Figure B.9 Nozzle Dimensions

When implementing this theory, the simplifying assumption is made that the same current amplification factor applies to all of the rings. In other words

$$A_j = A \tag{B-60}$$

for all values of j.

This assumption enables one to use (B-59) to write the following expression for the entire energy that needs to be absorbed by the magnetic nozzle (denoted by ΔE)

$$\Delta E = \sum_j \Delta E_j = (A-1)\frac{1}{2}\sum_j \frac{\Phi_j^2}{L_j} \tag{B-61}$$

This can be further simplified by noting that – to good approximation – the total magnetic flux enclosed by each ring is the same, and hence (replacing Φ_j by Φ)

$$\Delta E = (A-1)\frac{\Phi^2}{2}\sum_j \frac{1}{L_j} \tag{B-62}$$

where the final term, involving the sum of the inverse inductances, can be derived from (B-60).

This is an important expression because it allows one to establish the basic design parameters for the magnetic nozzle. A physical design for the nozzle (number of rings, together with their positions and radii) is first selected and used with (B-60) to derive the quantity $\sum_j \frac{1}{L_j}$. The quantity ΔE is derived by taking the total plasma kinetic energy that needs to be absorbed (which can be calculated from details of the fusion reaction) and factoring it down to account for the portion that escapes through the open part of the nozzle.

This enables one to write (B-62) as

$$(A-1)\frac{\Phi^2}{2} = \frac{\Delta E}{\sum_j \frac{1}{L_j}} \tag{B-63}$$

where the only remaining unknown quantities are A and Φ.

One can now complete the basic design *either* by selecting a current amplification factor – in which case (B-63) is used to derive the corresponding value of Φ (and hence define the necessary seed magnetic field) – *or* by selecting an initial seed magnetic field, and thus defining Φ, in which case (B-63) is used to derive the necessary current amplification factor (A).